

Hybrid Broadband Ground-Motion Simulation Validation of Small Magnitude Active Shallow Crustal Earthquakes in New Zealand

Robin L. Lee¹, robin.lee@canterbury.ac.nz

Brendon A. Bradley¹, brendon.bradley@canterbury.ac.nz

Peter J. Stafford², p.stafford@imperial.ac.uk

Robert W. Graves³, rwgraves@usgs.gov

Adrian Rodriguez-Marek⁴, adrianrm@vt.edu

¹University of Canterbury ²Imperial College London

³U.S. Geological Survey ⁴Virginia Tech

May 19, 2021

Peer Review DISCLAIMER: This draft manuscript is distributed solely for purposes of scientific peer review. Its content is deliberative and predecisional, so it must not be disclosed or released by reviewers. Because the manuscript has not yet been approved for publication by the U.S. Geological Survey (USGS), it does not represent any official USGS finding or policy.

Contents

1 Abstract	2
2 Introduction	3
3 Earthquake Sources and Ground-Motion Recording Stations Considered	5
3.1 Earthquake Sources	5
3.2 Ground-Motion Recording Stations	9
3.3 Observed Ground-Motion Records	10
4 Ground-Motion Modelling Methods and Inputs	11
4.1 Hybrid Broadband Method	11
4.2 Method Modifications	11
4.3 Crustal Velocity and Site Response Models	13
4.4 Empirical Ground-Motion Models	14
5 Illustrative Example Simulation: 22nd February 2016 M_w 4.8	15

6 Validation Analysis Method	18
7 Results and Interpretation	19
7.1 Model Prediction Bias, a	19
7.2 Between-event Residual, δB_e	21
7.2.1 Comparison for Entire Dataset	22
7.2.2 Dependence on Source Parameters	23
7.2.3 Spatial Dependence	23
7.3 Site-to-site and Within-event Residuals, $\delta S2S_s$ and δW_{es}	25
7.3.1 Systematic Site-to-site and Within-event Residuals for All Stations	26
7.3.2 Dependence on Site and Path Parameters	27
7.3.3 Spatial Dependence	29
7.3.4 Station Subcategory Analysis	30
8 Discussion	34
8.1 Spatially-Varying Stress Parameter	35
8.2 HF Duration Modification for Soft Soil Sites	36
8.3 V_{s30} Model Sensitivity	37
8.4 Examination of Topographic Effects	38
9 Conclusions	38
10 Data and resources	40
11 Acknowledgements	40
Appendices	i
A Electronic Supplement A: Event Information	i
B Electronic Supplement B: Station Information	xx
C Electronic Supplement C: Ground-Motion Simulation Method and Computational Considerations	xxv
D Electronic Supplement D: Fourier Amplitude Spectra Validation	xxvii
E Electronic Supplement E: Comparison of Residuals Against Source, Path and Site parameters	xxix
F Electronic Supplement F: Spatial Maps of δB_e and $\delta S2S_s$	xxxiv
G Electronic Supplement G: Additional Station Subcategory Analysis	xli

1 Abstract

- ² This paper presents a comprehensive validation of the hybrid broadband ground-motion simulation approach (via the commonly-used Graves and Pitarka (2010, 2015, 2016)

4 method) in a New Zealand context with small magnitude point source ruptures using
5 an extensive set of 5218 ground motions recorded at 212 sites from 479 active shallow
6 crustal earthquakes across the country. Modifications to the simulation method inferred
7 from a previous New Zealand validation are implemented and the improvements are ex-
8 plicitly quantified. Empirical ground-motion models are also considered to provide a
9 benchmark for simulation prediction accuracy and precision. Examination of intensity
10 measure residuals identifies that the the simulation method modifications lead to reduced
11 model prediction bias and within-event variability, and provides evidence toward the use of
12 spatially-varying coefficient models for simulation parameters, such as the high-frequency
13 Brune stress parameter. Additional biases identified include, among others, underpredic-
14 tion of significant durations at soft soil sites, and overprediction of short-period pseudo-
15 spectral accelerations at stiff alluvial gravel and rock sites due to low estimated 30 m
16 time-averaged shear-wave velocity values.

17 2 Introduction

18 Validation of physics-based ground-motion models (GMM) is important toward their uti-
19 lization in seismic hazard analysis (Graves et al., 2011) and earthquake engineering ap-
20 plications (Galasso et al., 2013; Bradley et al., 2017a; Bijelić et al., 2018). In the recent
21 decade, several significant ground-motion simulation validation efforts have been carried
22 out to assess the predictive capability of ground-motion simulation methods (e.g., Dreger
23 and Jordan (2015); Maufroy et al. (2015)). In particular, the Southern California Earth-
24 quake Centre (SCEC) Broadband Platform (BBP) exercise (Goulet et al., 2015) rigorously
25 evaluated four widely-used simulation methods implemented on the SCEC BBP (Atkinson
26 and Assatourians, 2015; Crempien and Archuleta, 2015; Graves and Pitarka, 2015; Olsen
27 and Takedatsu, 2015). In that study, twelve events of magnitude $M_w \geq 4.60$ and a total
28 of 394 pairs of orthogonal horizontal component observed ground-motion records were con-
29 sidered (from a potential set of 918 records within 200 km of their causative fault). From
30 comparisons between simulated and observed pseudo-spectral accelerations (pSA), as well
31 as empirically-predicted pSA, the predictive capability of the methods were quantified.

32 Additionally, several improvements to each of the simulation methods were identified as
33 a part of the validation. While a few other validation studies have utilized a comparable
34 number of events to the SCEC BBP exercise, e.g., Yenier and Atkinson (2015), Maufroy
35 et al. (2016), and Taborda et al. (2016), the majority of ground-motion simulation val-
36 idation studies focus on one or few specific events, such as the 1994 M_w 6.7 Northridge
37 and 2008 M_w 5.4 Chino Hills earthquakes, to demonstrate new ground-motion simulation
38 methods or input developments. For example, several recent studies have focussed on
39 validation of simulations which are deterministically calculated to frequencies as high as
40 10.0 Hz, and hence require additional fault and velocity model complexities (Graves and
41 Pitarka, 2016; Savran and Olsen, 2019) compared to previous ground-motion simulation
42 modelling studies, or explicitly consider plasticity (Withers et al., 2019). Other studies
43 have also focussed on the validation of earthquake ruptures that are currently not as well
44 understood, such as great subduction zone earthquakes (Wirth et al., 2017).

45 As the literature cited in the previous paragraph illustrates, validation against ob-
46 servations in an earthquake engineering context has usually been limited in the number
47 of earthquake events or number of ground-motion recording stations (and consequently
48 regional extent) considered. This is principally due to the scope of the particular studies
49 and the choice to consider large M_w earthquakes which are spatially sparse and temporally
50 infrequent. Small magnitude earthquakes ($M_w \leq 5.0$) occur significantly more frequently,
51 and although their direct relevance in earthquake engineering applications is limited, they
52 provide valuable information toward validation as their underlying processes are funda-
53 mentally the same as for large M_w earthquakes. Additionally, the relative simplicity in
54 source modelling of small M_w earthquakes allows for greater focus on the ground-motion
55 simulation method, crustal velocity model, and near-surface site-response to weak mo-
56 tions. Therefore, arguably, the first step toward an exhaustive validation study of a
57 spatially extensive region is to consider small M_w earthquakes.

58 Recently in a New Zealand (NZ) context, Lee et al. (2020) presented a comprehensive
59 hybrid broadband ground-motion simulation (Graves and Pitarka, 2010) validation study
60 in the Canterbury region considering 148 small M_w ($3.5 \leq M_w \leq 5.0$) earthquakes, with

61 1896 observed ground-motion records. Intensity measures (IM) calculated from observed
62 and simulated ground motions were compared and an analysis of prediction residuals
63 across the aggregated dataset was carried out to quantify the biases in the simulations
64 and their causes. Several potential improvements to the ground-motion simulation method
65 in a NZ context were identified. Prior to the Lee et al. (2020) study, only large M_w
66 scenarios had been considered in NZ for several prominent events, such as the 2011 M_w
67 6.2 Christchurch (Razafindrakoto et al., 2018) and 2016 M_w 7.8 Kaikōura earthquakes
68 (Bradley et al., 2017b).

69 Building on Lee et al. (2020), this study extends from that regional Canterbury study
70 to a nation-wide application in NZ. This paper provides a comprehensive validation of
71 the Graves and Pitarka (2010, 2015, 2016) hybrid broadband ground-motion simulation
72 method, with modifications informed by the previous validation, in NZ using small M_w
73 earthquakes. New and updated input models for source, 3D crustal velocity, and near-
74 surface 30 m time-averaged shear-wave velocity (V_{s30}) are also utilized. Firstly, a descrip-
75 tion of the data and methods used for the simulations are provided, followed by an outline
76 of the validation framework. Next, the results of the validation are presented, and finally
77 the near-term directions of opportunity are discussed.

78 **3 Earthquake Sources and Ground-Motion Record- 79 ing Stations Considered**

80 **3.1 Earthquake Sources**

81 Earthquake source descriptions used in this study were obtained from the GeoNet centroid
82 moment tensor (CMT) catalogue (Ristau (2008, 2013), [https://github.com/GeoNet/
83 data/tree/master/moment-tensor](https://github.com/GeoNet/data/tree/master/moment-tensor)). While the catalogue contains over 2400 earth-
84 quakes, dating back to the beginning of 2003, attention is restricted to small M_w , be-
85 tween 3.5–5.0, shallow crustal events, based on centroid depth (CD) less than 20 km.
86 Figure 1 presents the locations of earthquakes considered and ground-motion recording

87 stations, highlighting their spatial distribution, as well as surface projections of schematic
88 ground-motion raypaths which provide a qualitative illustration of the spatial domain
89 being robustly assessed in the simulation validation. Most earthquakes are clustered near
90 the tectonic plate boundary, with a significant proportion of earthquakes having occurred
91 due to the 2010-2011 Canterbury, 2013 Seddon and 2016 Kaikōura earthquake sequences
92 which were all located on the north-east region of the South Island. Earthquakes located
93 far offshore, such that they do not produce reliable ground motions at onshore ground-
94 motion recording stations due to large distances, have been excluded. The minimum M_w
95 = 3.5 was chosen to ensure there is adequate constraint on earthquake source parame-
96 ters (i.e., related to the CMT solution) and sufficient signal-to-noise ratio (SNR) of the
97 ground-motion records. The maximum M_w = 5.0 was chosen to ensure that the point-
98 source modelling approximation utilized is generally valid for the majority of observed
99 ground motions (which significantly simplifies the source modelling and consequent un-
100 certainties) and that there is no appreciable off-fault near-surface nonlinear soil behaviour
101 in order to reduce uncertainties associated with modelling nonlinear site response. The
102 range of CD considered (0–20 km) is expected to broadly cover earthquakes which are
103 mostly located above the crustal seismogenic depth and therefore likely classified as active
104 shallow crustal. A minimum requirement of three high-quality observed ground motions
105 per event was also enforced (in an effort to limit the potential influence of statistical out-
106 liers) resulting in 479 earthquakes in the final dataset. This requirement is less strict than
107 the five high-quality ground motions required in Lee et al. (2020) as the density of earth-
108 quakes surrounding many recording stations in NZ is much less than in the Canterbury
109 region.

110 Figure 2 illustrates the M_w and source-to-site distance (R_{rup}) distributions of the
111 earthquakes and corresponding recorded ground motions considered. Figure 2b shows
112 the M_w - R_{rup} distribution of the recordings has relatively widespread coverage in the M_w -
113 R_{rup} space of typical interest. The histograms in Figures 2a and 2c illustrate that the
114 earthquake M_w have an expected increase in number of events with decreasing M_w down
115 to M_w = 4 and the majority of ground-motion records have $R_{rup} \leq 80$ km. The decrease in

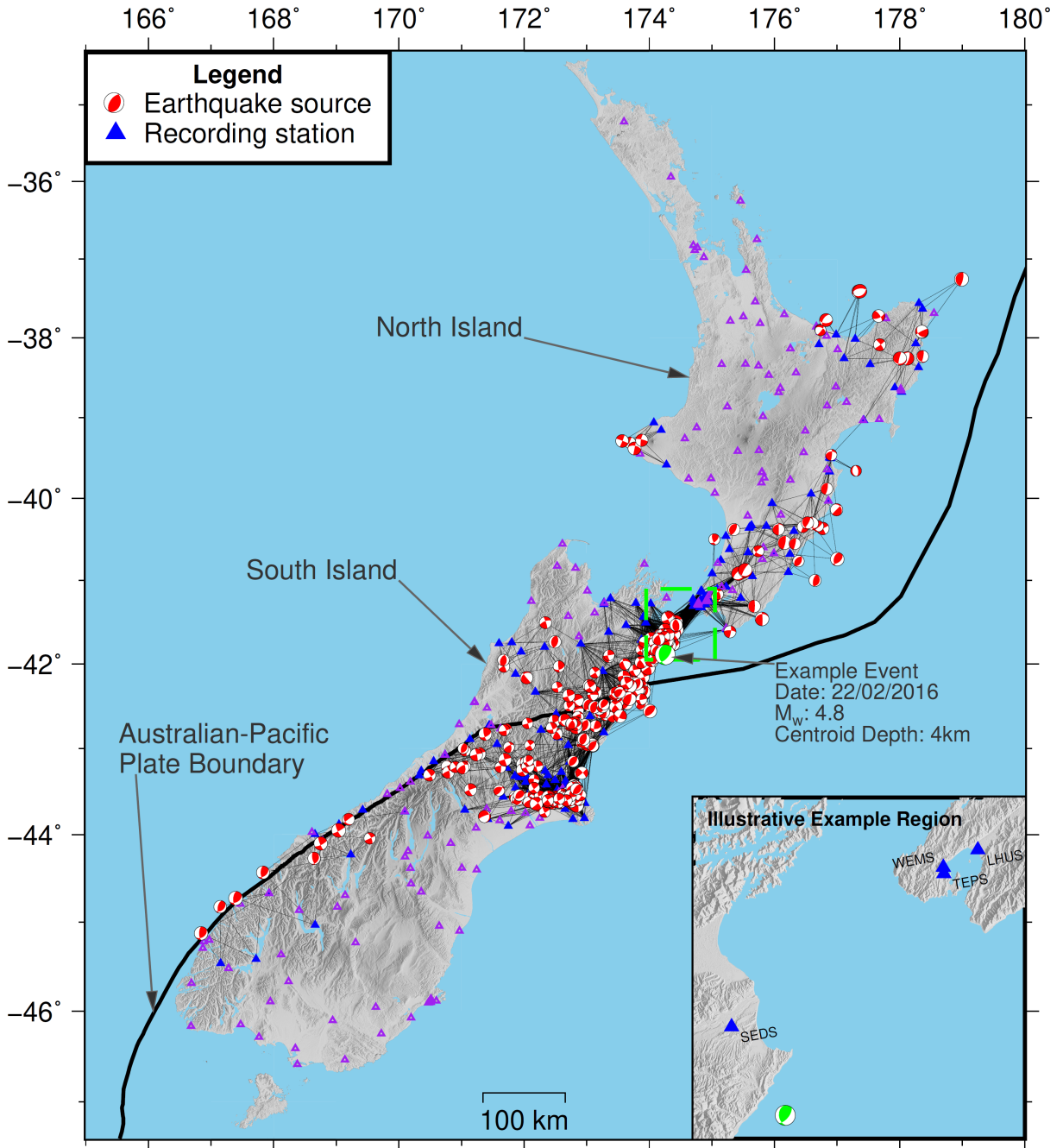


Figure 1: Location of 479 earthquake sources and 382 ground-motion recording stations considered across New Zealand. 212 stations used in the validation are shown as blue filled markers while the 170 stations not used due to insufficient records are shown as purple unfilled markers. Schematic ray paths between the causal source and recording station of the final set of 5218 ground motions are also shown as black lines. The Australian-Pacific tectonic plate boundary is shown by the thick black line. The earthquake corresponding to the subsequent illustrative example simulation is highlighted and the inset shows the station locations of the presented waveforms.

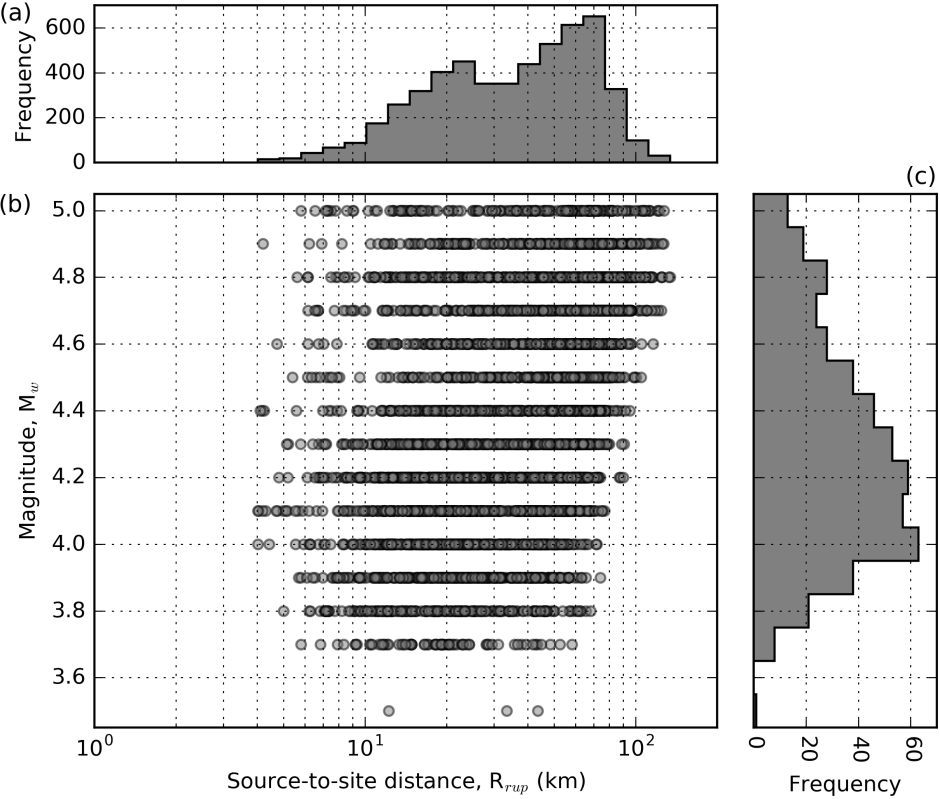


Figure 2: Earthquake source and ground-motion dataset distributions: (a) source-to-site distance histogram; (b) magnitude versus source-to-site distance scatter plot; (c) magnitude histogram.

number of events below $M_w = 4$ occurs due to the inability to determine CMT solutions for many such events due to insufficient low-frequency energy (Ristau, 2018). No maximum R_{rup} is enforced, however, the largest R_{rup} considered in this study are within the range used for similar M_w in several empirical GMM studies (over 200 km, e.g., Chiou et al. (2010)). Thus, bias associated with instrument triggering (Boore et al., 1993) are not expected.

Figures 3a and 3b present histograms of the earthquake CD and the number of sites per earthquake (NS_e). The distribution of CD is relatively uniform with the exception of more shallow events at 4 km, 6 km and 8 km. Figure 3c presents a plot of M_w against NS_e which illustrates that larger values of NS_e generally correspond to the larger M_w earthquakes. Table A.1 in Electronic Supplement A provides further details of all the earthquakes events considered.

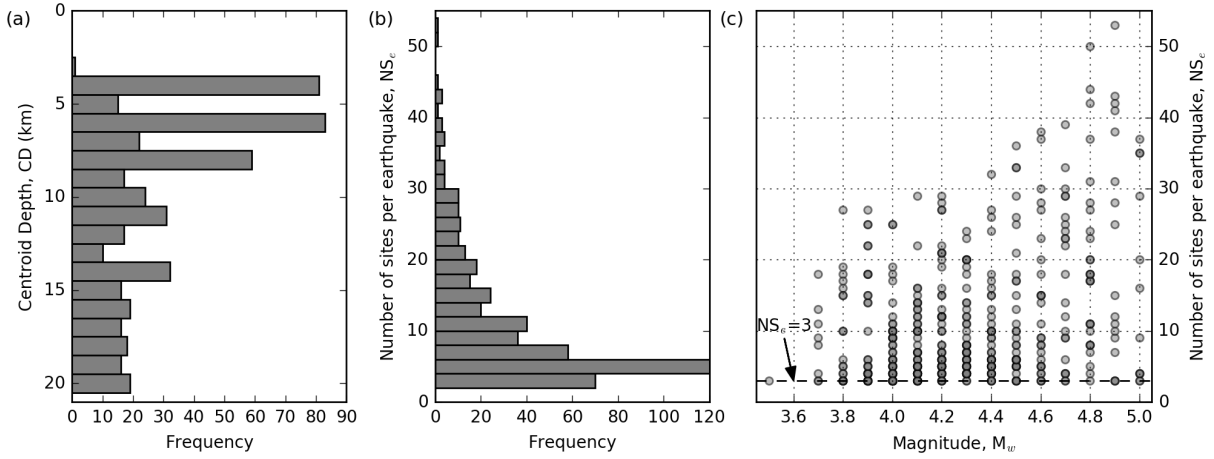


Figure 3: Earthquake source-related dataset distributions: (a) centroid depth histogram; (b) number of sites per earthquake histogram; (c) magnitude versus number of sites per earthquake NS_e scatter plot. In panel (c), all markers are the same transparency so apparently darker symbols are multiple events with the same NS_e .

¹²⁸ 3.2 Ground-Motion Recording Stations

¹²⁹ Of the 382 ground-motion recording stations considered in this study (Figure 1), 212 stations recorded a sufficient quantity of high-quality ground motions from different ¹³⁰ earthquake events (at least three), while 170 stations did not (and hence were not used). Of ¹³¹ these 212 stations, 23 were broadband stations (commonly installed at rock sites) and ¹³² 189 were strong-motion stations. Stations are relatively evenly distributed across most ¹³³ of the country, and are therefore located upon highly variable site conditions, with the ¹³⁴ exception of larger densities in population centres, such as Canterbury and Wellington ¹³⁵ (whose locations are shown in Figure B.1 in Electronic Supplement B). To quantify the ¹³⁶ site conditions, this study uses V_{s30} . Measured values of V_{s30} (through either invasive or ¹³⁷ non-invasive testing methods) are used, where available, at 32 stations. Where measured ¹³⁸ values are not available, the Foster et al. (2019) NZ-wide V_{s30} model is used, which pre-¹³⁹dicts values based on surface geology and terrain categories conditioned on assumed prior ¹⁴⁰ distributions and measured values. Figure 4a presents the distribution of V_{s30} values at ¹⁴¹ the 212 sites, explicitly showing the distribution of measured and estimated V_{s30} , where ¹⁴² there is notably few high values (i.e., $V_{s30} > 600$ m/s) despite many sites being nominally ¹⁴³ located on rock. Figure 4b presents the distribution of the number of earthquake-induced ¹⁴⁴ ground motions per site (NE_s), where most sites have recorded less than 40 earthquakes, ¹⁴⁵

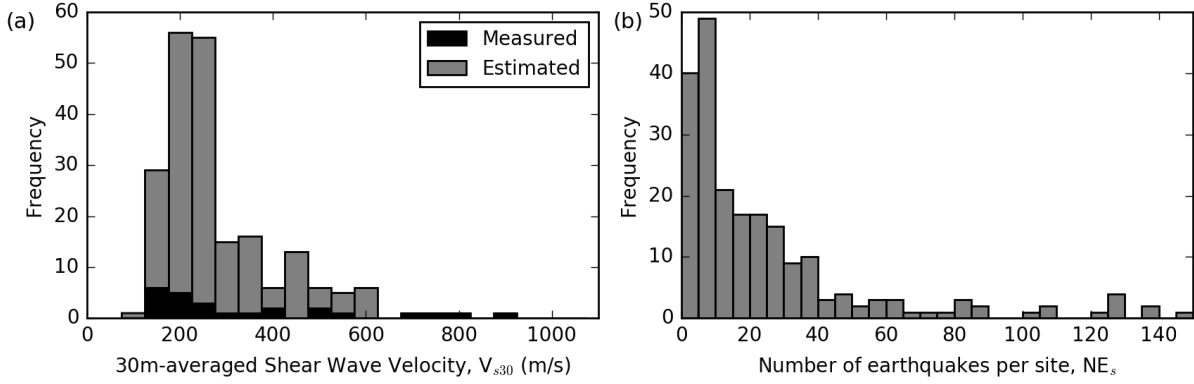


Figure 4: Ground-motion recording station distributions: (a) 30 m time-averaged shear-wave velocity (V_{s30}) directly measured or estimated from the Foster et al. (2019) NZ-wide V_{s30} model; (b) number of earthquake-induced ground motions per site (NE_s).

¹⁴⁶ although several have more than 100.

¹⁴⁷ 3.3 Observed Ground-Motion Records

¹⁴⁸ Volume 1 (unprocessed) ground-motion records were obtained from the GeoNet file trans-
¹⁴⁹ fer protocol (see Data and Resources). All ground motions were baseline corrected, de-
¹⁵⁰ trended and processed with a 4th order Butterworth filter with a low-pass frequency of
¹⁵¹ 50 Hz (for sample rate of 200 Hz) or 20 Hz (for sample rate of 50 Hz), and a high-pass
¹⁵² frequency of 0.08 Hz to reliably retain the Fourier amplitudes at $f \geq 0.1$ Hz (Boore and
¹⁵³ Bommer, 2005; Ancheta et al., 2014). From the 479 earthquake events, 19064 ground
¹⁵⁴ motions were recorded. However, the low amplitudes of many records (a consequence of
¹⁵⁵ small M_w earthquakes) lead to variable quality such that many are not usable for ground-
¹⁵⁶ motion simulation validation. Issues include low SNR, poor triggering, premature ending
¹⁵⁷ of records, and other instrument problems, which prevent the earthquake ground-motion
¹⁵⁸ signal from being adequately resolved. To quantify the quality of the ground motions, and
¹⁵⁹ hence determine which ground motions are usable, the ground-motion quality classifica-
¹⁶⁰ tion neural network developed by Bellagamba et al. (2019) was used. The neural network
¹⁶¹ provides a score on how well the ground motion resembles the good records which it was
¹⁶² trained upon through features such as frequency-dependent SNR, Fourier amplitude ra-
¹⁶³ tios, and time-domain acceleration amplitude ratios. A quality score threshold of 0.5 was

¹⁶⁴ used such that a score below would be considered a low-quality record and a score above
¹⁶⁵ would be considered a high-quality record. From the suite of 19064 candidate ground
¹⁶⁶ motions, the final ground-motion dataset consists of 5218 ground-motion recordings (i.e.,
¹⁶⁷ 27.4% of records).

¹⁶⁸ 4 Ground-Motion Modelling Methods and Inputs

¹⁶⁹ 4.1 Hybrid Broadband Method

¹⁷⁰ This study adopts the hybrid broadband ground-motion simulation approach developed
¹⁷¹ by Graves and Pitarka (2010, 2015, 2016). This approach computes the low-frequency
¹⁷² (LF) and high-frequency (HF) ground-motion components separately using comprehensive
¹⁷³ and simplified physics, respectively. The comprehensive physics method uses a finite
¹⁷⁴ difference formulation to explicitly model 3D wave propagation and the simplified physics
¹⁷⁵ method (often referred to as a ‘stochastic’ method) is based on a simpler theoretical
¹⁷⁶ representation of wave propagation. The two components are then merged in the time
¹⁷⁷ domain using a 4th order Butterworth filter, with an LF-HF transition frequency of $f_t =$
¹⁷⁸ 1 Hz, to produce a single broadband (BB) time series. A summary of the simulation
¹⁷⁹ method pertaining to this specific study is included in Electronic Supplement C, while
¹⁸⁰ comprehensive details can be found in Graves and Pitarka (2010, 2015, 2016). For HF
¹⁸¹ simulation parameters, this study adopts values calibrated for the California region in lieu
¹⁸² of specific evidence to the contrary but simulation validation studies can drive refinements
¹⁸³ of these choices in the future. Computational considerations and optimizations for this
¹⁸⁴ study are also included in Electronic Supplement C.

¹⁸⁵ 4.2 Method Modifications

¹⁸⁶ Two modifications are made to the simulation method based on prior validation by Lee
¹⁸⁷ et al. (2020). Firstly, validation results illustrated that the significant durations of sim-
¹⁸⁸ ulated ground motions were too short compared to observed records (which also influ-
¹⁸⁹ enced short-period pSA). Therefore, the HF path duration model, previously defined as

¹⁹⁰ $D_p = 0.07R_{rup}$ (GP10, Graves and Pitarka (2010)), was replaced with the Boore and
¹⁹¹ Thompson (2014) (BT14) path duration model for active shallow crustal earthquakes.
¹⁹² Boore and Thompson (2014) identified that conventional path duration models for sim-
¹⁹³ plified physics ground-motion simulation methods resulted in underprediction of durations
¹⁹⁴ and developed their model specifically to be used with these methods. Figure 5a presents
¹⁹⁵ a plot of the two path duration models, highlighting the increase across the range of R_{rup}
¹⁹⁶ relevant to this study. The BT14 path duration model gives larger path durations at all
¹⁹⁷ R_{rup} , with the extent of this difference depending on the particular distance.

¹⁹⁸ The second simulation method modification is motivated by Lee et al. (2020) identi-
¹⁹⁹ fying that the V_{s30} -based empirical site amplification factor model used (Campbell and
²⁰⁰ Bozorgnia, 2014) was likely double-counting long-period site effects, which were already
²⁰¹ explicitly modelled through the 3D velocity model used in the LF finite difference simu-
²⁰² lation. Therefore, the empirical site amplification was modified to no longer be applied
²⁰³ to the LF simulation component, but is still applied to the HF simulation component in
²⁰⁴ the conventional manner. Figure 5b presents examples of the empirical site amplification
²⁰⁵ functions, as applied in this study and also previous studies (e.g., Graves and Pitarka
²⁰⁶ (2010) and Lee et al. (2020)), for one set of input variables ($V_{sref} = 500$ m/s, $V_{s30} = 250$
²⁰⁷ m/s and $\text{PGA} = 0.025$ g). Although the empirical site amplification is only applied to
²⁰⁸ the HF simulation component (primarily corresponding to periods $T \leq 1$ s), the modified
²⁰⁹ function used has reduced long-period amplification to reduce frequency roll-off effects
²¹⁰ when merging.

²¹¹ The subsequent validation presented in this paper will highlight and quantify the
²¹² improvements to prediction of ground-motion IMs made by these two modifications. For
²¹³ brevity herein, the Graves and Pitarka (2010, 2015, 2016) method as outlined in the
²¹⁴ respective papers, and used in Lee et al. (2020), will be referred to as the ‘Standard’
²¹⁵ simulation method and the method with the two modifications will be referred to as the
²¹⁶ ‘Modified’ simulation method.

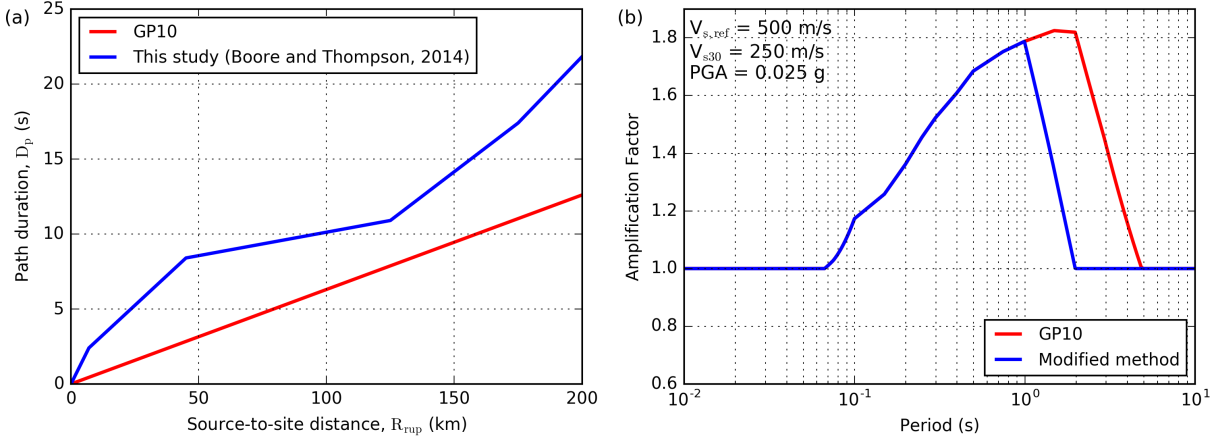


Figure 5: Simulation method modifications: (a) HF path duration models as a function of source-to-site distance; and (b) empirical V_{s30} -based site amplification factor.

217 4.3 Crustal Velocity and Site Response Models

218 To simulate LF ground motions, the New Zealand Velocity Model (NZVM, Thomson
 219 et al. (2019), see Data and Resources) is used to provide the P-wave and S-wave veloci-
 220 ties, and density required (V_p , V_s and ρ , respectively). This study uses a recent version
 221 of the NZVM (v2.02), with several improvements over the velocity model utilized in the
 222 related Canterbury validation study of Lee et al. (2020) (NZVM v1.66) and other previ-
 223 ous validation studies (Bradley et al., 2017b; Razafindrakoto et al., 2018). Figure 6a and
 224 6b present fence diagrams of 6 cross sections (whose transects are shown in Figure 6c)
 225 throughout the upper South Island of NZ for NZVM v1.66 and v2.02, respectively, high-
 226 lighting their general features and recent modifications. The primary components of the
 227 velocity model are the embedded sedimentary basin models and a background travel-time
 228 tomography-based seismic velocity model (Eberhart-Phillips et al., 2010). NZVM v2.02
 229 includes 7 additional sedimentary basins. Specifically, from north to south: Wellington,
 230 Nelson, Marlborough, Kaikōura, Hanmer, North Canterbury and Cheviot. The second
 231 major improvement is the inclusion of a geotechnical layer throughout the top 350 m of
 232 the model outside of the embedded sedimentary basins (to effectively represent weath-
 233 ered rock and shallow soil conditions). This follows the commonly-used V_{s30} -dependent
 234 formulation of Ely et al. (2010) in combination with the Foster et al. (2019) V_{s30} model.
 235 In this study, the Standard simulation utilizes the NZVM v1.66 (consistent with previous

²³⁶ validation by Lee et al. (2020)) while the Modified simulation uses the NZVM v2.02. For
²³⁷ the HF component simulations, a generic 1D velocity model is used. Figure 6d presents
²³⁸ the V_p , V_s and ρ profiles which comprise the 1D velocity model.

²³⁹ It is important to note that such nation-wide scale input models have large spatial
²⁴⁰ variability in quality. For example, the crustal velocity model for seismic wave propagation
²⁴¹ may be better characterized in some regions (e.g., in the New Zealand Velocity Model,
²⁴² NZVM, the Canterbury region has a high resolution sedimentary basin model whereas
²⁴³ the rest of New Zealand has either simplistic basin models or the basin model is absent).
²⁴⁴ Likewise for near-surface velocity models (e.g., V_{s30}), only a subset of ground-motion
²⁴⁵ recording stations have ‘measured’ values (either from invasive or non-invasive testing).
²⁴⁶ However, it is usually not feasible to carry out field testing to obtain these measurements
²⁴⁷ at every station, and therefore nation-wide models which use broader and more general
²⁴⁸ sets of data, coupled with correlations, must be utilized. The effect of such aspects in
²⁴⁹ the inputs will likely lead to variability in predictive performance of simulation methods.
²⁵⁰ However, for forward prediction applications, with many locations of interest that are not
²⁵¹ explicitly characterized with measurements, the use of such models is a necessity.

²⁵² 4.4 Empirical Ground-Motion Models

²⁵³ In addition to the comparison between observed and simulated ground motions, the per-
²⁵⁴ formance of selected horizontal component empirical GMMs are also evaluated. The
²⁵⁵ empirical prediction models considered in this study are the Bradley (2013) NZ-specific
²⁵⁶ ground-motion model for peak ground acceleration (PGA), peak ground velocity (PGV)
²⁵⁷ and pseudo-spectral acceleration (pSA); Campbell and Bozorgnia (2012) for Arias in-
²⁵⁸ tensity (AI), Campbell and Bozorgnia (2010) for cumulative absolute velocity (CAV);
²⁵⁹ and Afshari and Stewart (2016) for 5-75% and 5-95% significant durations (D_{s575} and
²⁶⁰ D_{s595} , respectively). Prediction using empirical models is intended to provide a relative
²⁶¹ performance benchmark for the simulations, and therefore exhaustive empirical predic-
²⁶² tions making use of a logic tree of alternate models was not considered.

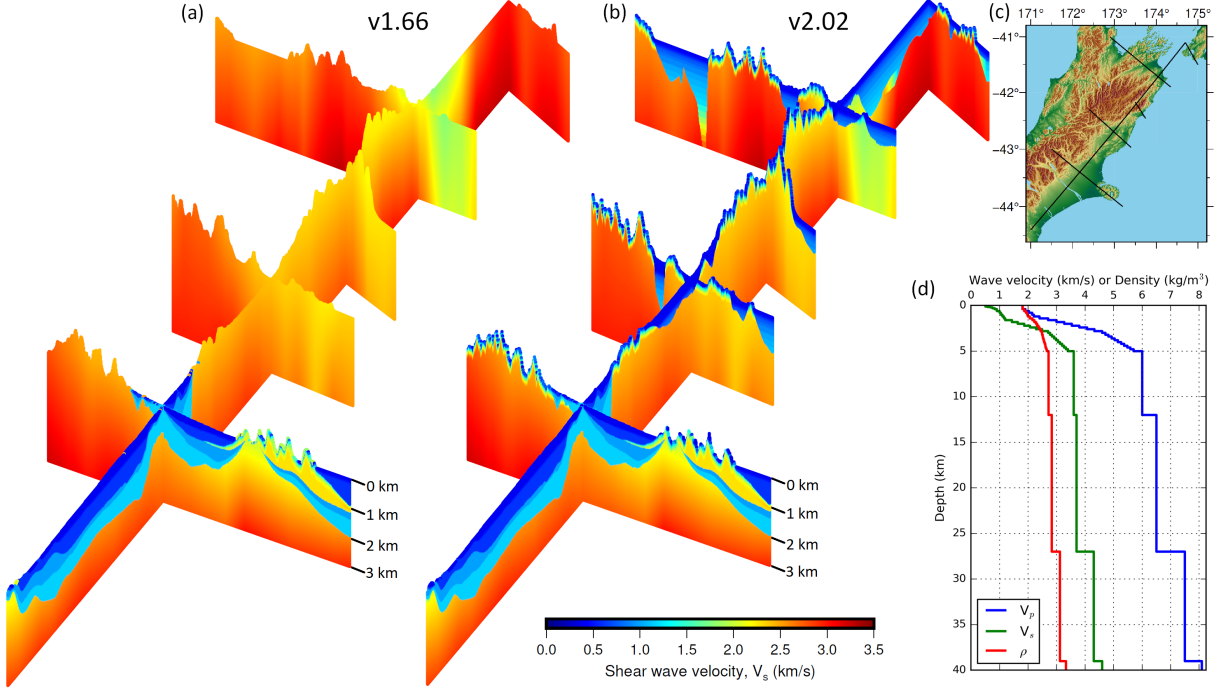


Figure 6: Crustal velocity models for ground-motion simulations. Fence diagram of six shear-wave velocity (V_s) cross sections, extending to 3 km below mean sea level, through the 3D velocity model in the upper South Island region for LF simulations: (a) NZVM v1.66; (b) NZVM v2.02; (c) location of cross section transects; and (d) 1D velocity model for HF simulations. The 1D velocity model has constant values below 38 km.

263 5 Illustrative Example Simulation: 22nd February 264 2016 M_w 4.8

265 As an example, simulation results from the 22nd February 2016 M_w 4.8 earthquake
266 (GeoNet Public ID: 2016p140897) located at $CD = 4$ km in the Marlborough region
267 (see Figure 1), are presented to provide insight on the salient attributes of the ground-
268 motion simulations. The focal mechanism of the event was associated with a reverse fault
269 (strike $\phi = 39^\circ$, dip $\delta = 62^\circ$, rake $\lambda = 115^\circ$) and had $NS_e = 20$ high-quality recordings.

270 Figure 7 presents velocity waveforms at four stations of interest (locations shown
271 in Figure 1) which highlight the ground-motion simulation modifications. The black, red
272 and blue waveforms correspond to observed, Standard simulation and Modified simulation
273 ground motions, respectively. At the LHUS site ($R_{rup} = 90.8$ km and $V_{s30} = 195$ m/s), the
274 Modified simulation waveform has longer duration of HF ground motion than the Standard

simulation, as well as lower velocity amplitudes, as a result of the increased HF path duration model (Figure 5a), which are more comparable to the observed waveforms. For the WEMS ($R_{rup} = 81.5$ km and $V_{s30} = 257$ m/s) and TEPS ($R_{rup} = 80.0$ km and $V_{s30} = 195$ m/s) sites, the Standard simulation has LF velocity amplitudes which are too large as a result of the V_{s30} -based empirical site amplification (Figure 5b). The Modified simulation doesn't apply this empirical site amplification and therefore produces more reasonable LF velocity amplitudes. The SEDS site is located in Marlborough, north-west of the causative fault ($R_{rup} = 28.8$ km and $V_{s30} = 289$ m/s). The Standard simulation does not have significant late-arriving LF amplitudes or coda waves, whereas the Modified simulation produces basin-generated waves, due to the inclusion of the Marlborough sedimentary basin in the NZVM, which are also present in the observed waveforms.

Figure 8 shows PGA, pSA(2.0s) and D_{s595} as a function of R_{rup} for the 20 observed and simulated ground motions for this event. The median and ± 1 standard deviation of the relevant empirical prediction models are shown as the solid and dashed lines, respectively. To show the empirical model median as a single line against R_{rup} , a reference V_{s30} of 250 m/s is used, a representative value for Site Class D (New Zealand Standards, 2004), while subsequent site-specific prediction bias comparisons use the value of each individual station. All predictions provide a generally good comparison with observed PGA values, although the Modified simulation is marginally better, as measured using misfit residuals. For pSA(2.0s), the Standard simulation significantly overpredicts for $R_{rup} = 70\text{--}100$ km (in Wellington), likely due to the aforementioned double-counting of site amplification, while the Modified simulation and empirical model only slightly overpredict. The Standard simulation significantly underpredicts D_{s595} values at all distances while the Modified simulation provides better predictions due to the new HF path duration model. Nonetheless, the empirical model provides a better prediction of significant duration than both simulations.

Figure 9 summarizes the bias and variability (as the mean and standard deviation, respectively) of the IM total residuals (more rigorously discussed in the next section) for this event. Overall, the biases for the Modified simulation are closer to zero than the

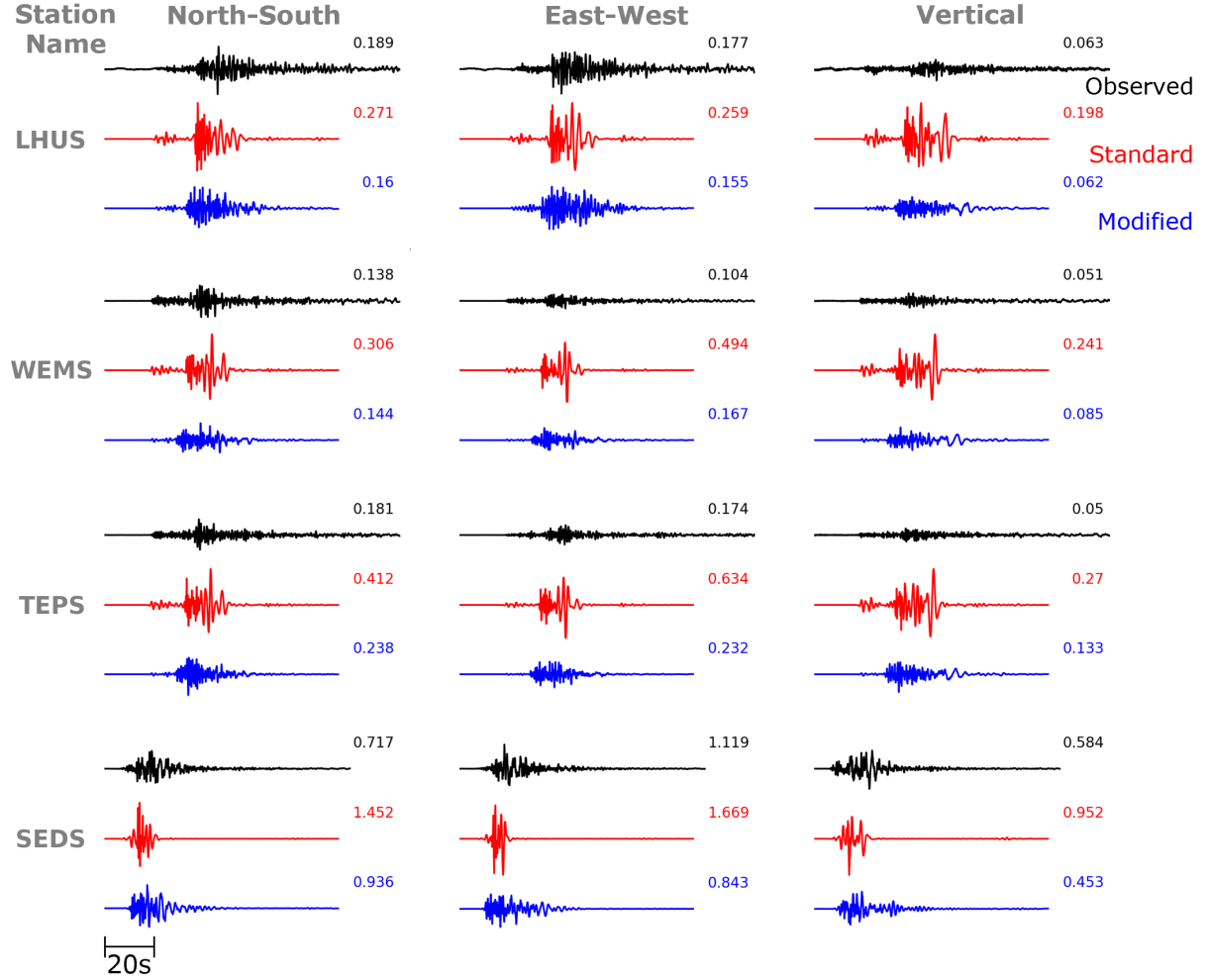


Figure 7: Comparison of observation (black), Standard simulation (red) and Modified simulation (blue) broadband velocity waveforms at four strong-motion stations of interest (LHUS, WEMS, TEPS in Wellington, and SEDS in Marlborough) for the 22nd February 2016 M_w 4.8 event. PGV values are provided to the right of each waveform in cm/s.

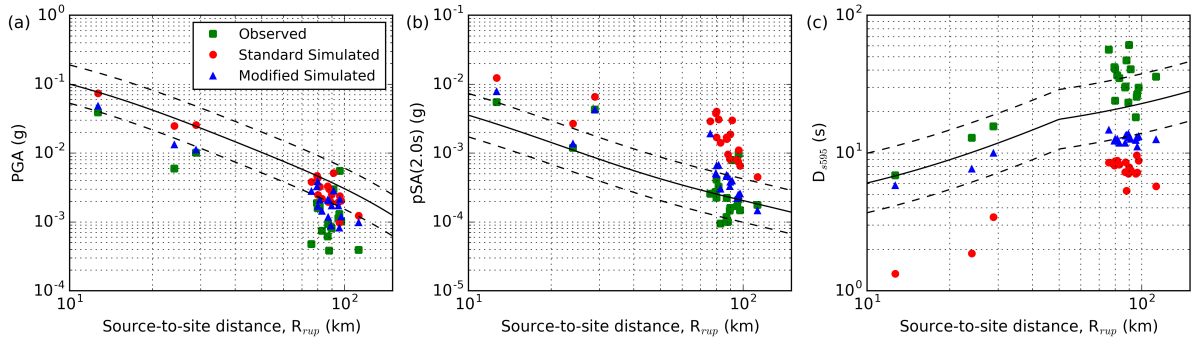


Figure 8: Observed, simulated and empirically predicted horizontal geometric mean ground-motion intensity measures as a function of source-to-site distance, R_{rup} , for the 22nd February 2016 M_w 4.8 event: (a) PGA; (b) pSA(2.0s); (c) D_{s595} .

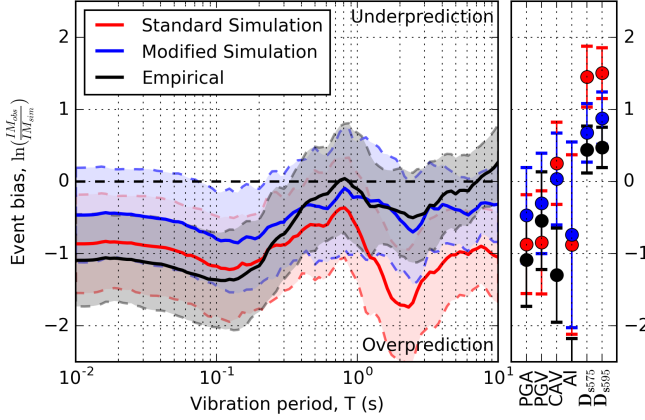


Figure 9: Systematic bias between observed and predicted IMs for all ground-motion recordings from the 22nd February 2016 M_w 4.8 earthquake. Solid lines and points indicate the systematic bias (mean residual), while the shaded regions and horizontal bars indicate ± 1 standard deviation.

³⁰⁴ Standard simulation for all IMs, where the latter is most overpredicted for 1.0–4.0 s pSA
³⁰⁵ and significant durations. While this analysis is for only one event, and therefore may be
³⁰⁶ subject to event-specific features, it illustrates the general simulation improvements.

³⁰⁷ 6 Validation Analysis Method

³⁰⁸ Due to the large number of earthquake events considered, the primary focus of the anal-
³⁰⁹ ysis are the systematic effects across the entire dataset of ground motions. To achieve
³¹⁰ this, the total prediction residuals are partitioned into various components associated
³¹¹ with ground motion variability using a partially-crossed linear mixed-effects regression
³¹² algorithm (Stafford, 2014; Bates et al., 2015). Following the notation of Al Atik et al.
³¹³ (2010), the general form of a GMM for an event, e , and site, s , pairing can be written as:

$$\ln \text{IM}_{es} = f_{es} + \Delta \quad (1)$$

³¹⁴ where $\ln \text{IM}_{es}$ is the natural logarithm of the observed IM; f_{es} is the mean of the predicted
³¹⁵ logarithmic intensity measure (given by either a single ground-motion simulation for each
³¹⁶ event or an empirical GMM) which is a function of the earthquake rupture, e , and site
³¹⁷ location, s ; and Δ is the total residual. The total residual can be further decomposed

³¹⁸ into fixed and random effects:

$$\ln \text{IM}_{es} = f_{es} + a + \delta B_e + \delta W_{es} \quad (2)$$

³¹⁹ where a is the (global) model prediction bias (fixed effect); δB_e is the between-event
³²⁰ residual (random effect) with zero mean and variance τ^2 ; and δW_{es} is the within-event
³²¹ residual (random effect) with zero mean and variance ϕ^2 . Comparison of Equations (1)
³²² and (2) illustrates that Δ has mean a and variance $\sigma^2 = \tau^2 + \phi^2$ assuming that δB_e and
³²³ δW_{es} are independent random variables. δB_e represents the systematic misfit between
³²⁴ observation and bias-corrected mean prediction for a given earthquake, e . Systematic
³²⁵ location-to-location effects are not modelled, thus those effects will be included in the
³²⁶ distribution of δB_e . δW_{es} represents the difference between observation and the bias-and-
³²⁷ event-corrected mean prediction for a ground-motion record corresponding to earthquake
³²⁸ e and site s . Lastly, δW_{es} can be further partitioned into a systematic effect and a
³²⁹ remaining residual:

$$\ln \text{IM}_{es} = f_{es} + a + \delta B_e + \delta S2S_s + \delta W_{es}^0 \quad (3)$$

³³⁰ where $\delta S2S_s$ is the systematic site-to-site residual, and δW_{es}^0 is the ‘remaining’ within-
³³¹ event residual which represents factors which are not systematically accounted for by the
³³² δB_e or $\delta S2S_s$, or not accounted for in the models themselves. $\delta S2S_s$ is a zero-mean random
³³³ effect with variance ϕ_{S2S}^2 , and δW_{es}^0 has residual variance ϕ_{ss}^2 so that $\phi^2 = \phi_{S2S}^2 + \phi_{ss}^2$.

³³⁴ 7 Results and Interpretation

³³⁵ 7.1 Model Prediction Bias, a

³³⁶ Model prediction bias (a) and total standard deviation (σ) for various IMs predicted
³³⁷ via the Standard and Modified simulations, as well as the relevant empirical GMMs,
³³⁸ are presented in Figure 10. The total standard deviations (and standard deviations of
³³⁹ partitioned components shown in subsequent sections) correspond to the bias-corrected

340 variances and therefore reflect the variability around the global biases. Therefore, the total
341 standard deviations presented should be considered in tandem with the global biases in the
342 assessment of the precision of each GMM. The Standard simulation shows the same trends
343 as previous validation carried out by Lee et al. (2020) for the Canterbury region, with
344 overprediction of PGA, PGV and pSA across all periods, and severe underprediction of
345 significant durations. D_{s575} and D_{s595} have $a = 1.63$ (a factor of 5.1) and $a = 1.94$ (a factor
346 of 7.0), respectively, which are beyond the axes of the plot but are placed at $a = 1.5$ for
347 visual completeness. The Modified simulation has less overprediction than the Standard
348 simulation for PGA, PGV and pSA across all periods. At short periods, $T \leq 1.0$ s, this
349 is a general result of the improved HF path duration model reducing HF acceleration
350 amplitudes (as discussed in Lee et al. (2020)), and at long periods, $T > 1.0$ s, due to the
351 removal of the ‘additional’ empirical V_{s30} -based site amplification. The decrease in HF
352 acceleration amplitudes also contributes toward some bias reduction at long periods as HF
353 acceleration amplitudes are generally larger than LF acceleration amplitudes for small M_w
354 earthquakes and tend to also influence long-period pSA values slightly beyond the period
355 corresponding to the LF-HF transition frequency, $T = 1/f_t = 1.0$ s (Bora et al., 2016). The
356 improvements to the NZVM result in minor increases to the moderate period pSA (not
357 explicitly evident) which are secondary compared the simulation method changes. The
358 triangular-shaped feature in the Modified simulation pSA bias at short periods indicate
359 increasing overprediction with period up to roughly $T = 0.8$ s. This overprediction has
360 the same general shape as the empirical site amplification function (for weak motions),
361 suggesting that empirical V_{s30} -based site amplification may be too large, likely caused by
362 estimated V_{s30} values that are too low, and is addressed subsequently in the discussion of
363 systematic site-to-site variability. The significant durations of the Modified simulation are
364 drastically less biased than the Standard simulation, again due to the HF path duration
365 model change. The empirical prediction of PGA, PGV, and most short-period pSA have
366 relatively small bias, while long-period pSA has more substantial underprediction, which
367 is similar to the trends identified in other studies (Bradley, 2015; Lee et al., 2020). The
368 empirical predictions of significant durations have practically no bias.

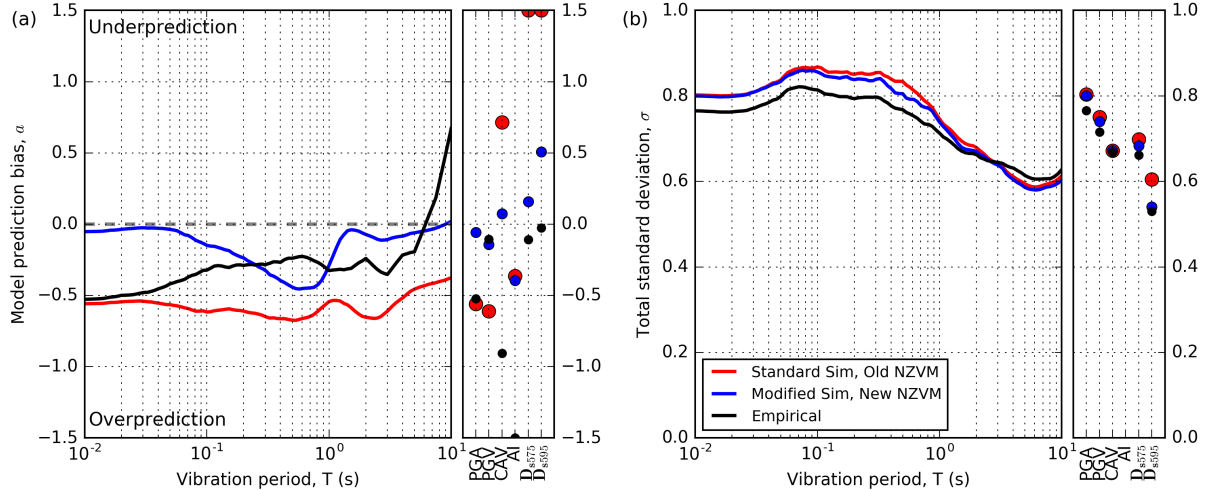


Figure 10: Simulated and empirical prediction of IMs for the entire dataset considered: (a) systematic model prediction bias, a ; and (b) total standard deviations, σ . For visual completeness, $a = 1.63$ and $a = 1.94$ for Standard simulation D_{s575} and D_{s595}, respectively, are plotted at $a = 1.5$, and $a = -2.24$ for empirical AI is plotted at $a = -1.5$.

The σ of the Modified simulation compared to the σ of the Standard simulation shows a slight decrease across all IMs indicating that the Modified simulation has more precise predictions. The empirical prediction σ are also slightly smaller than both simulation methods at short and moderate pSA periods but larger at long periods (crossing over at approximately $T = 3.0$ s). Compared to previous validation in the Canterbury region only (Lee et al., 2020), the σ for simulation and empirical predictions in this study are generally larger (previously pSA σ ranged from 0.7–0.5 compared to 0.8–0.6 in this study) as a result of moving to an NZ-wide application where there is a broader range of source, path and site conditions (emphasized by the change in the empirical σ), as well as more variable and lower average quality of inputs (particularly for site characterization and crustal velocity modelling).

Additional analysis of the bias associated with smoothed Fourier amplitude spectra (FAS) was carried out to identify the salient changes to the frequency content in the simulations and is included in Electronic Supplement D.

7.2 Between-event Residual, δB_e

In the ground-motion simulations, the between-event residuals, δB_e , are generally associated with errors in source attributes or deviations from average source model scaling.

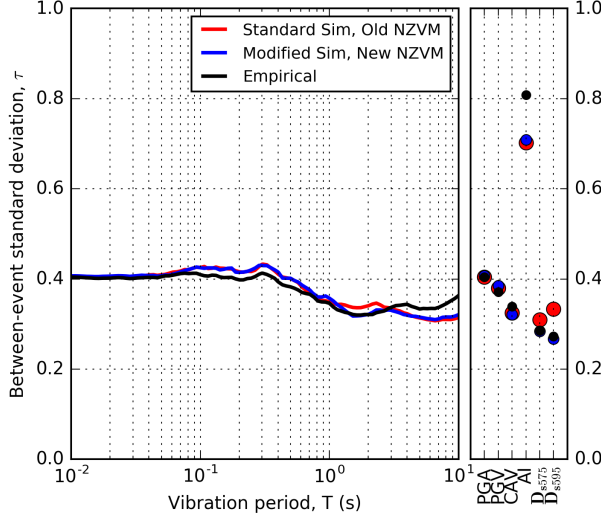


Figure 11: Between-event standard deviation, τ , for simulated and empirical predictions.

The primary parameters in this regard are earthquake magnitude, location in the Earth’s crust, faulting mechanism (Ristau, 2008) and HF stress parameter (Brune, 1970; Frankel, 2009; Graves and Pitarka, 2010) as point sources are used in this study. The empirical GMMs considered in this study represent the source effects through magnitude scaling, depth-to-rupture measures (e.g., Z_{TOR}), and faulting mechanism modifications.

7.2.1 Comparison for Entire Dataset

Figure 11 presents the between-event standard deviations, τ , for the simulated and empirical predictions. For PGA, PGV, and pSA at all periods, τ is similar for all prediction methods, with values between roughly 0.36–0.43, indicating similar between-event variability. The larger values of τ occur at shorter periods while the smaller values occur at longer periods. This may be a result of the spectral ordinates at the longer periods being driven by the Fourier amplitudes below the source corner frequency, so variability in factors such as stress parameter are not evident. The Modified simulation and empirical model significant durations have the smallest τ , below 0.3 while the Standard simulation significant durations have slightly larger τ , at around 0.35.

401 **7.2.2 Dependence on Source Parameters**

402 The obtained δB_e values were compared against several source parameters; M_w , CD and
403 focal mechanism, to determine the causes of the variability and identify any parameter de-
404 pendence within δB_e . However, interpretation of CD and focal mechanism dependence did
405 not yield any significant trends, and hence are omitted here, but presented in Electronic
406 Supplement E. Figure 12 provides comparisons between δB_e and M_w for PGA, pSA(2.0s)
407 and D_{s595} for the Standard simulation, Modified simulation and empirical predictions. In
408 these plots, the average trend is also indicated quantitatively via locally weighted linear
409 regression. For PGA and pSA(2.0s), predicted from both Standard and Modified simula-
410 tion methods, there is no significant trend except some slight relative underprediction for
411 $M_w < 4.0$. This is likely due to the selective CMT solution generation for earthquakes
412 $M_w < 4.0$, where only earthquakes with sufficient low-frequency energy are calculated,
413 which would correspond to statistically stronger earthquake ground motions for a given
414 M_w . The result on biases would be similar to instrument triggering biases, where sta-
415 tistically weaker ground motions with amplitudes near the instrument trigger threshold
416 would be omitted. For empirical prediction, pSA(2.0s) shows this same feature but it
417 is not present in PGA. The D_{s595} δB_e for the Standard simulation has a slight negative
418 linear trend which suggests better prediction at larger M_w when considering the model
419 prediction bias ($a = 1.94$), which was also identified in Lee et al. (2020). This trend is ex-
420 pectedly absent in the Modified simulation, as a result of changing the HF path duration
421 model; while the empirical prediction also has no trend.

422 **7.2.3 Spatial Dependence**

423 Figures 13a and 13b present plots of the spatial variation of PGA δB_e for the Modified
424 simulation and empirical prediction, respectively, showing the values at station locations
425 and a surface developed using geostatistical Kriging to illustrate spatial trends. Spatial
426 plots of δB_e for other IMs are included in Electronic Supplement F. The spatial distri-
427 butions are relatively similar between the Modified simulation and empirical prediction,
428 and differences are difficult to identify visually. A primary feature is the region of relative

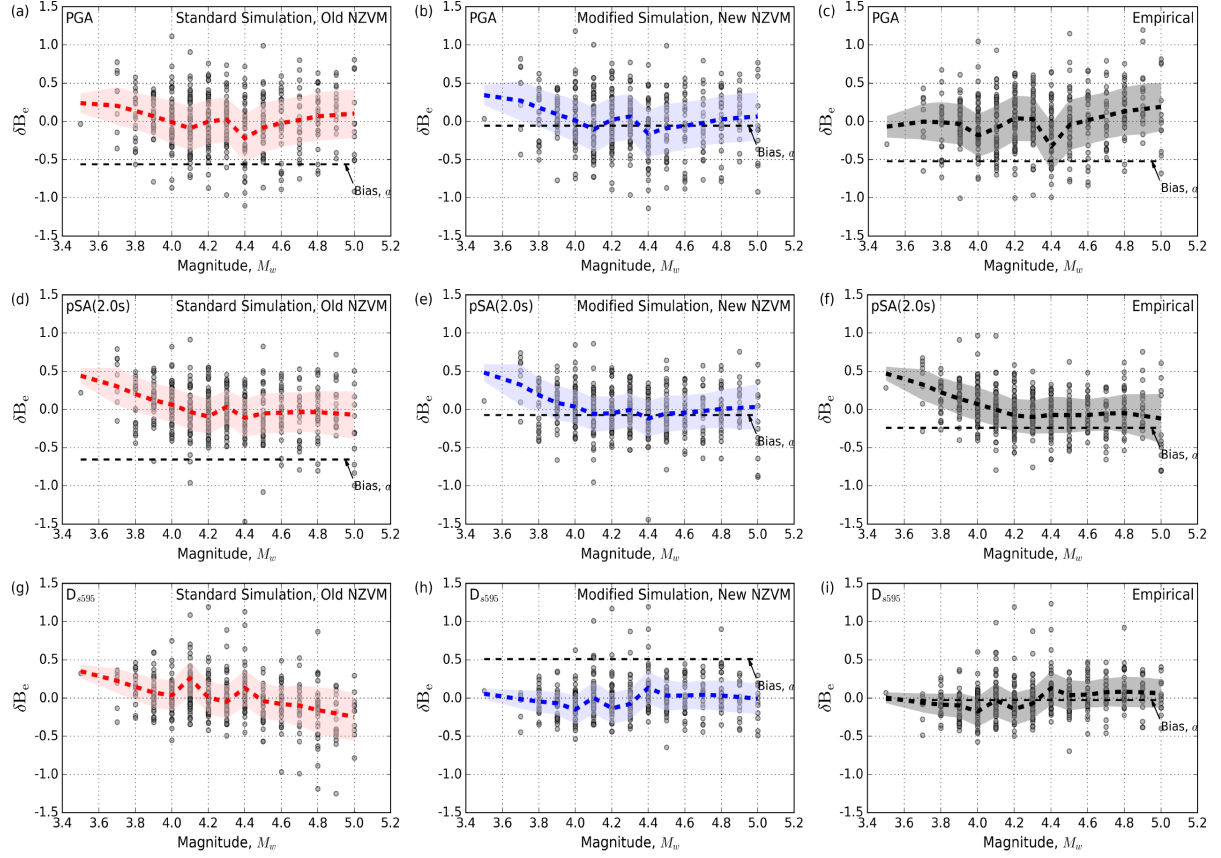


Figure 12: Comparison of simulated and empirically-predicted between-event residual, δB_e , against M_w for PGA, pSA(2.0s) and D_{s595} . The locally weighted scatterplot smoothing regression trend lines are represented as the thick dashed lines with shaded regions corresponding to 16-84th percentile confidence intervals, while the associated model prediction biases, a , are represented as the thin dashed line. For Standard simulation D_{s595} , (g), the model prediction bias is $a = 1.94$ and is therefore outside of the axes shown.

overprediction (blue) at the centre of the South Island. For the simulations, it is speculated that this overprediction may be due to the constant stress parameter adopted, $\Delta\sigma = 5$ MPa, as the stress conditions may be weaker in this region. This trend would be mirrored in empirical prediction as there is no explicit consideration of stress parameter in the Bradley (2013), or other, empirical GMMs. Although depth-dependent stress parameter effects may be implicitly considered in Z_{TOR} (Boore et al., 2014), as all earthquakes considered are active shallow crustal, the variations due to stress parameter are more likely to be associated with regional differences rather than depth-dependence. Figure 13c summarizes the correlation of δB_e between the different prediction methods for all IMs. The correlation between the two simulation methods is expectedly higher than the correlations between each simulation and empirical prediction. The high correlations at

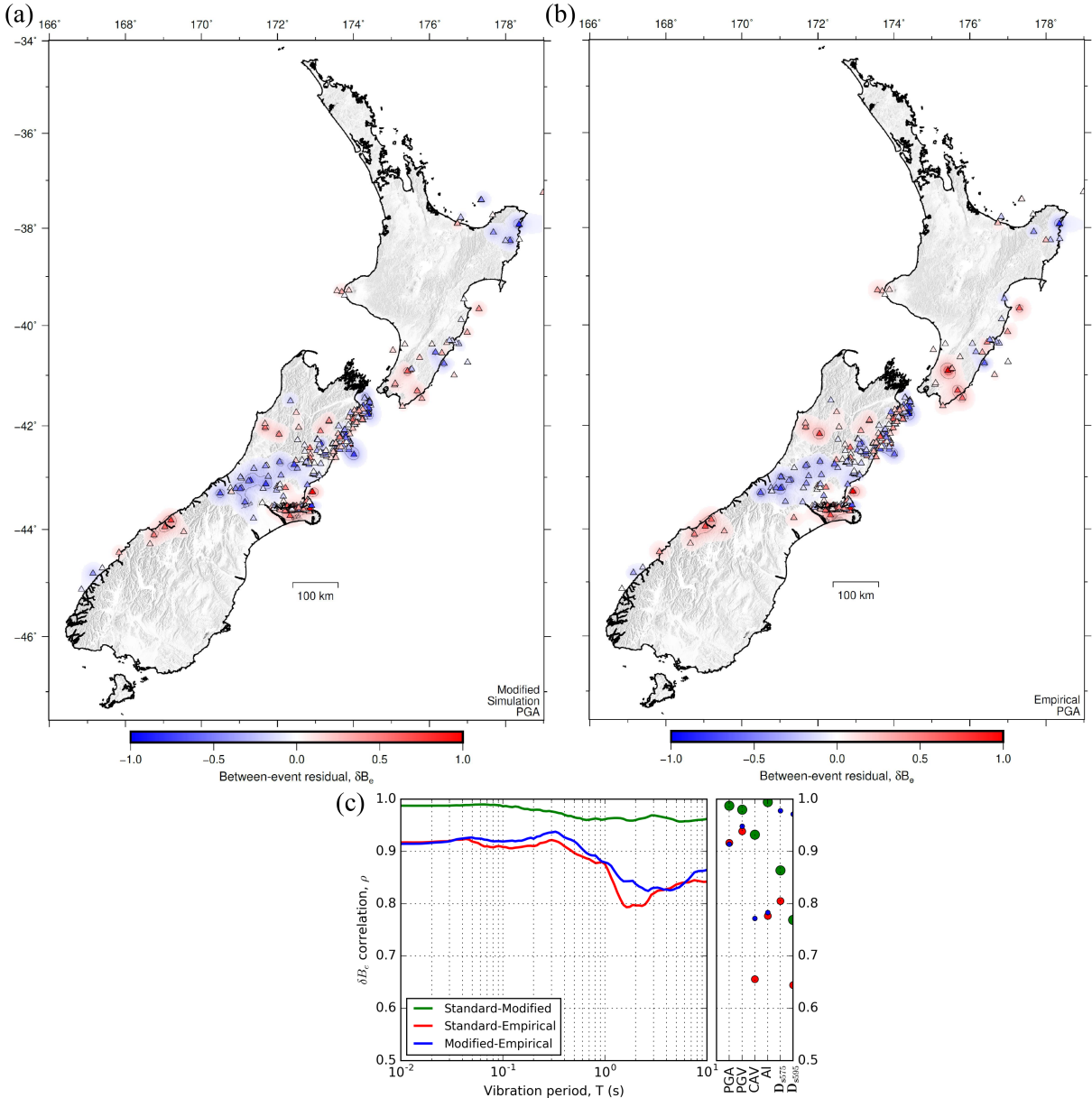


Figure 13: Spatial distribution of PGA between-event residual, δB_e , for: (a) Modified simulation; and (b) empirical prediction, for all 479 earthquake events across NZ; and (c) a summary of the correlation, ρ , between prediction methods for all IMs.

440 short vibration periods further indicates source properties such as the stress parameter
 441 could be considered regionally variable and a discussion of this is presented subsequently.

442 7.3 Site-to-site and Within-event Residuals, $\delta S2S_s$ and δW_{es}

443 A broad range of site conditions and crustal properties exist in NZ at the ground-motion
 444 station locations. Within-event residuals, δW_{es} , are inherently associated with wave prop-
 445 agation path and near-surface site effects given the number of ground motions per event

446 considered. For simulated ground motions, the path effect is dependent on the wave
447 propagation through the specific velocity model (3D NZVM and 1D velocity model for
448 LF and HF simulations, respectively). In this study, path effects are simply investigated
449 with respect to R_{rup} and azimuth-specific path effects are not investigated. Site effects
450 are also dependent on the velocity model, however, the spatial resolution of the velocity
451 models used in this study are unable to accurately capture all near-surface site effects,
452 which is the essential motivation for using empirical site amplification factors to adjust
453 the simulations for reference site conditions. Empirical GMMs commonly treat path ef-
454 fects through various source-to-site distance parameters, and site effects through V_{s30} and
455 depth-to-rock parameters.

456 7.3.1 Systematic Site-to-site and Within-event Residuals for All Stations

457 Figure 14a and 14b present the within-event standard deviations, ϕ_{S2S} and ϕ_{ss} , respec-
458 tively, for the simulated and empirical predictions. For all IMs considered, ϕ_{S2S} are similar
459 between simulation and empirical predictions, roughly 0.30–0.52, with the largest differ-
460 ences at long periods. Minor differences between the two simulation results at long periods
461 are due to the improvements to the NZVM and removal of the empirical V_{s30} -based site
462 amplification at low frequencies. The Modified simulation appears to have slightly higher
463 ϕ_{S2S} , possibly because the LF simulation component remains at the output reference ve-
464 locity (despite long periods being generally less influenced by near-surface soils than short
465 periods).

466 Previously, in the Canterbury-specific study by Lee et al. (2020), there was a relative
467 increase in ϕ_{S2S} for $T=1.0\text{--}4.0$ s which is not present in any of the predictions in this
468 study. This was found to be primarily due to a few sites which had poor estimates of V_{s30}
469 (e.g., CSHS previously had a V_{s30} consistent with rock as it was located in a mountainous
470 region but has since been identified to be on relatively soft soil). While the removal of
471 empirical site amplification for the LF simulation component removes such inconsistencies,
472 the revision of V_{s30} values still causes differences at short periods (as it is still applied to
473 HF simulation component). The empirical prediction has ϕ_{S2S} slightly lower than the

474 simulations at short periods and slightly larger at long periods. The size of ϕ_{S2S} , relative
475 to σ , indicates that significant improvements in ground-motion prediction are possible
476 through being able to capture this systematic phenomena (Rodriguez-Marek et al., 2011)
477 through further improvements in the simulation input models and method itself.

478 The ϕ_{ss} from the Modified simulation is slightly smaller than the ϕ_{ss} for Standard sim-
479 ulation for all IMs considered suggesting that the adopted modifications capture slightly
480 better the ‘remaining’ physical phenomena, most likely path effects. This may be through
481 changes resulting from the improved HF path duration model as there are record-specific
482 influences due to the R_{rup} dependence. Empirical GMMs have lower ϕ_{ss} than both simu-
483 lations, implying that they currently have less unexplained variability. However, as only
484 a single ground-motion simulation is run for each event, inherent stochastic features such
485 as the HF random phase spectrum can also contribute to ϕ_{ss} , particularly for short period
486 pSA. Running several simulations for each event and considering the mean of all realisa-
487 tions for each event could provide a more consistent comparison between empirical and
488 simulated ϕ_{ss} . It is also important to note that τ (Figure 11), ϕ_{S2S} and ϕ_{ss} are all of
489 similar size implying that the variability in δB_e , $\delta S2S_s$ and δW_{es}^0 are similar. While the
490 simulation method modifications have source-, site- and record-specific influences, their
491 effects are still relatively general, which has led to only small reductions in standard de-
492 viations. It is expected that further nonergodic modifications (e.g., event-specific stress
493 parameter, explicit physics-based site response analysis for modelling near-surface site
494 effects, among others) have the potential to more significantly reduce simulation standard
495 deviations.

496 7.3.2 Dependence on Site and Path Parameters

497 In order to evaluate the variability and biases resulting from site effects, $\delta S2S_s$ are com-
498 pared against V_{s30} . A comparison between δW_{es}^0 and R_{rup} did not identify any conclusive
499 trends and is therefore omitted from the main text but included in Electronic Supplement
500 E.

501 Figure 15 presents the comparisons of $\delta S2S_s$ with V_{s30} for PGA, pSA(2.0s) and D_{s595}

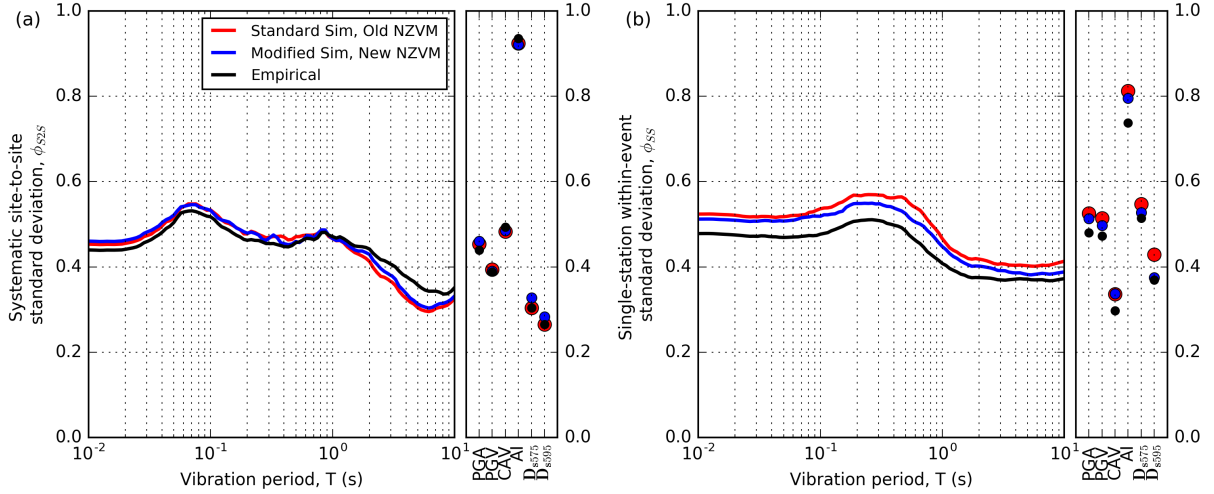


Figure 14: Within-event standard deviations: (a) systematic site-to-site uncertainty, ϕ_{S2S} ; and (b) single-station within-event variability, ϕ_{ss} .

for the Standard and Modified simulations, and empirical prediction. The comparison for PGA shows no significant trend while the comparison for pSA(2.0s) shows a slight negative trend at low V_{s30} for the Modified simulation which is likely a result of removing empirical site amplification for the LF simulation component (i.e., lower V_{s30} is relatively underpredicted). For both simulations and empirical prediction, the comparison for D_{s595} shows a strong negative trend at low V_{s30} . This was also identified in Lee et al. (2020) with the Standard simulation, and remains in the Modified simulation as no direct modification has been made on this aspect. This is attributed to the fact that the acceleration amplitudes have been modified by the period-dependent V_{s30} -based site amplification while the duration of the motion (reflected by D_{s595}) has had no modification (i.e., the site amplification is applied in the frequency domain to the FAS amplitudes) despite it being well understood that softer sites result in longer durations of motion (e.g., Afshari and Stewart (2016)). Additionally, the Boore and Thompson (2014) path duration model utilized in the Modified simulation is independent of site conditions and therefore does not address this issue either. Overall, the lack of site effect duration contributions in the HF simulations lead to its underestimation, and this is more significant for softer sites at shorter distances, where the ‘site contribution’ to duration is relatively larger.

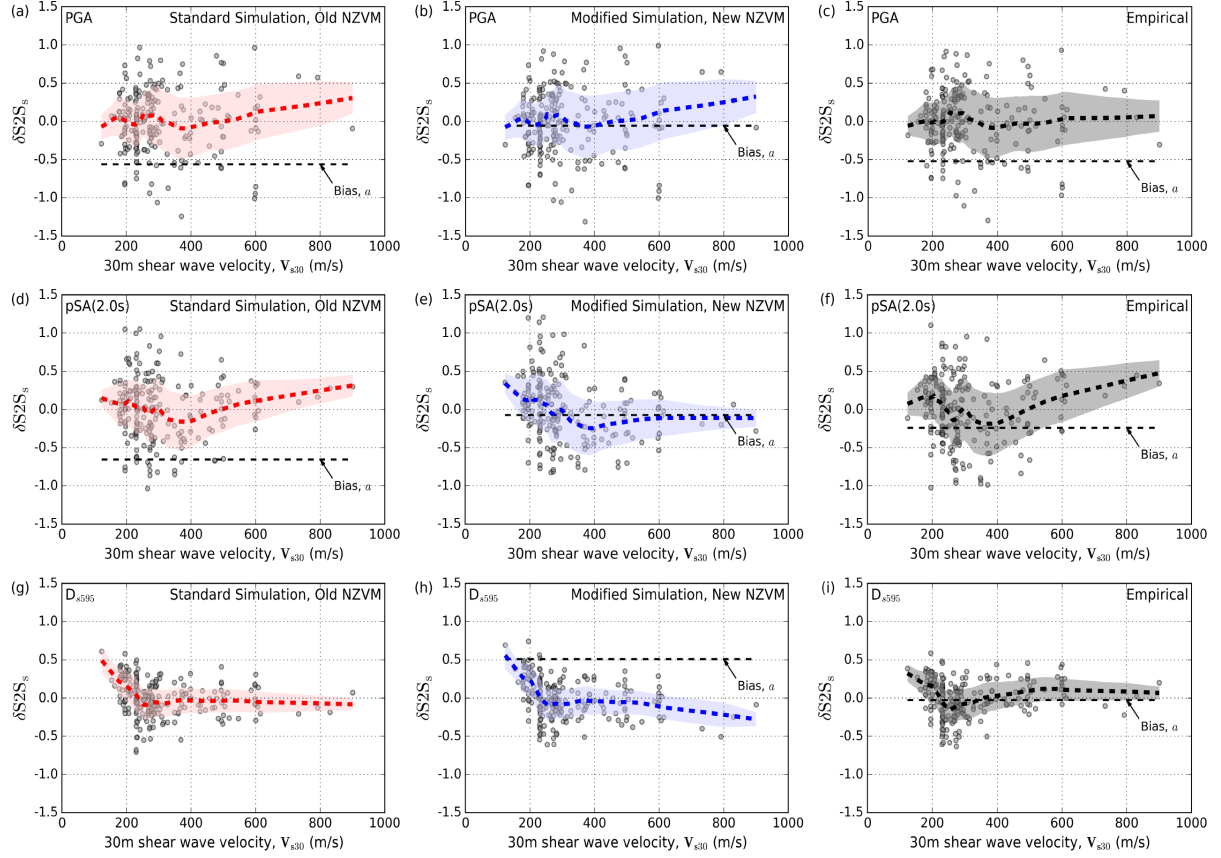


Figure 15: Comparison of simulated and empirically-predicted systematic site-to-site residual, $\delta S2S_s$, against V_{s30} for PGA, pSA(2.0s) and D_{s595} . The locally weighted scatterplot smoothing regression trend lines are represented as the thick dashed lines with shaded regions corresponding to 16-84th percentile confidence intervals, while the associated model prediction biases, a , are represented as the thin dashed line. For D_{s595} from Standard simulation, (g), the model prediction bias is $a = 1.94$ and is therefore outside of the axes shown.

519 7.3.3 Spatial Dependence

520 Figures 16a and 16b illustrate the spatial variation of $\delta S2S_s$ for pSA(2.0s) for the Modified
 521 Simulation and empirical prediction, respectively, showing the values at station locations
 522 and a surface developed using Kriging. Spatial plots of $\delta S2S_s$ for other IMs are included
 523 in Electronic Supplement F. The spatial distributions between the two methods are rel-
 524 atively similar but small localized differences are noticeable. Figure 16c summarizes the
 525 correlation of $\delta S2S_s$ between the different prediction methods for all IMs. The correlation
 526 between all methods at short periods is very high as the site effects are accounted for
 527 by V_{s30} -based amplification in all methods. At longer periods, the correlations reduce
 528 as a result of different methodological treatment of site effects. The largest difference,

529 between Modified simulation and empirical predictions, occurs because the Modified sim-
530 ulation does not have any direct dependence on V_{s30} since no site amplification is applied
531 (although V_{s30} is used in the 3D crustal model in non-basin regions, as discussed in the
532 Crustal Velocity and Site Response Models section). Figure 16d summarizes the correla-
533 tion of δW_{es}^0 between the different prediction methods for all IMs. Although the correlation
534 between methods are different, the Standard-Empirical and Modified-Empirical correla-
535 tions have similar shape. The size and spatial distribution of $\delta S2S_s$ values, and similarities
536 in treatment of site effects among all predictions (indicated by the high correlations in
537 Figure 16c and 16d), suggest that explicit site response is likely needed to better model
538 site-specific effects, although several improvements can also be made to the HF simula-
539 tions to better consider site-specific characteristics (e.g., site-specific 1D velocity models
540 and the near-surface diminution factor κ_0).

541 7.3.4 Station Subcategory Analysis

542 In addition to identifying significant trends through spatial plots, grouping stations with
543 similar site characteristics into subcategories and analysing them collectively can provide
544 insight into their systematic trends. Subcategories considered are: (1) stiff alluvial gravel
545 sites which have estimated V_{s30} values that are considered too low considering the age of
546 the deposits, or distance from any coastline or water feature (39 sites); (2) stiff rock sites
547 which have estimated V_{s30} values that are considered too low (34 sites); (3) sites with shal-
548 low soil overlying stiff rock (10 sites); and (4) sites which show strong basin amplification
549 in observed ground motions, but their sedimentary basin is not explicitly modelled in the
550 NZVM (11 sites). Each of the 212 stations was manually classified considering publically
551 available data on the site characteristics (e.g., previous V_{s30} estimates, depth-to-rock esti-
552 mates, site period (Kaiser et al., 2017), Google satellite imagery, and surface geology and
553 topography maps). Figure B.1 in Electronic Supplement B presents a plot of the station
554 locations corresponding to the subcategories. This analysis is only presented here for the
555 Modified simulation as it has been assessed to be the simulation method that provides the
556 better prediction of ground-motion IMs. Equivalent analyses for the Standard simulation

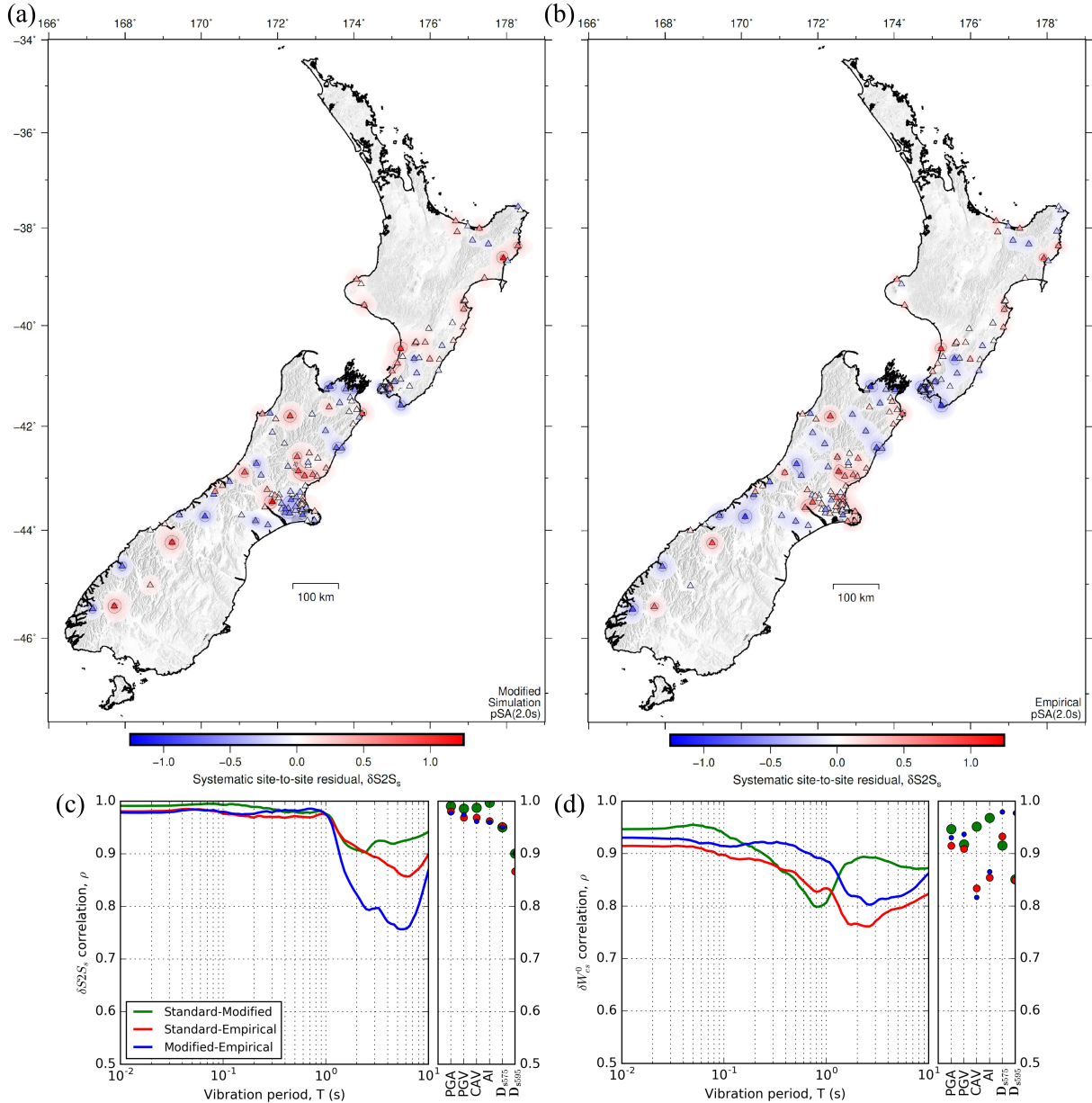


Figure 16: Spatial distribution of pSA(2.0s) $\delta S2S_s$ for: (a) Modified simulation; and (b) empirical prediction, for the 212 stations across NZ; (c) a summary of $\delta S2S_s$ correlation between prediction methods for all IMs; and (d) a summary of δW_{es}^0 correlation between prediction methods for all IMs

and empirical prediction are included in Electronic Supplement G, as well a comparison between prediction methods.

The results for all the subcategories are shown in Figure 17. To analyse the sub-categories, the sum of model prediction bias and systematic site-to-site residual (i.e., $a + \delta S2S_s$) for each station in that subcategory are plotted (grey), along with the average of those stations (black, termed the ‘subset bias’), and the global model prediction bias

563 for all sites (*a*) as a benchmark for comparison (blue). Shaded regions and error bars
564 indicate the 90% confidence interval of the respective mean bias estimates.

565 Figures 17a and 17b present the subcategory analyses for the stiff gravel, low V_{s30}
566 sites; and stiff rock, low V_{s30} sites, respectively. The subset bias for both subcategories are
567 significantly more negative than the global bias at all pSA periods, with largest difference at
568 the periods corresponding to greatest HF empirical site amplification (see Figure 5b). This
569 indicates that the sites in this subcategory are disproportionately overpredicted, and this is
570 possibly a primary contributor to the global overprediction at short periods. The inferred
571 low V_{s30} values would lead to overamplification from the empirical site amplification, which
572 causes the triangular-shaped feature in the global model prediction bias. The Foster et al.
573 (2019) V_{s30} model was found to predict estimates that are considered too low for these
574 sites, most likely because they reflect conditions not well represented in the limited data
575 used in the Foster et al. (2019) model. Specifically, some alluvial soil classifications are
576 dominated by the large amount of lower V_{s30} data values from the Christchurch central
577 business district, which is adjacent to the eastern coastline of the South Island, as well
578 as the lack of explicit age considerations and the broad deposition classifications. This
579 issue was identified at several sites located on the Canterbury alluvial plains (e.g., GDLC,
580 CACS, RKAC, ROLC, SWNC, TPLC, DFHS sites) which have measured V_{s30} values
581 between roughly 400–550 m/s, while surrounding stations which used the Foster et al.
582 (2019) model were prescribed lower V_{s30} ranging from approximately 200–350 m/s. In a
583 similar vein, rock sites were often also estimated with inferred low values due to missing
584 microfeatures and discretization issues with the Foster et al. (2019) model when used as
585 a raster as many rock sites are located near rock-soil boundaries.

586 Figure 17c presents the subcategory analysis for the shallow soil overlying stiff rock
587 sites. The short-period pSA of this subcategory are underpredicted compared to the
588 global bias. This is inferred as a result of the HF simulation using the quarter wavelength
589 (QWL) method with a generic 1D velocity model which does not capture the resonance
590 effects of such shallow impedance contrasts. An alternative, which was previously alluded
591 to, would be to carry out explicit physics-based site response analysis with a site-specific

592 velocity profile in a post-hoc manner (e.g., Hartzell et al. (2002), Roten et al. (2012),
593 Jeong and Bradley (2017a), Jeong and Bradley (2017b), de la Torre et al. (2020)).

594 Figure 17d presents the subcategory analysis for the sites located in a sedimentary
595 basin that is not explicitly modelled in the NZVM v2.02 and exhibit strong basin am-
596 plification. The largest difference between this subset bias and the global bias occurs at
597 moderate periods, between $T = 1.0\text{--}3.0$ s, which is expected to be the range of periods
598 corresponding to the basin responses at the sites. Over this period range, the subset bias
599 is most underpredicted as the basin reverberations would not be produced in the simula-
600 tions without an explicit sedimentary basin model. Therefore inclusion of more embedded
601 sedimentary basin models in the NZVM would improve the prediction at these sites.

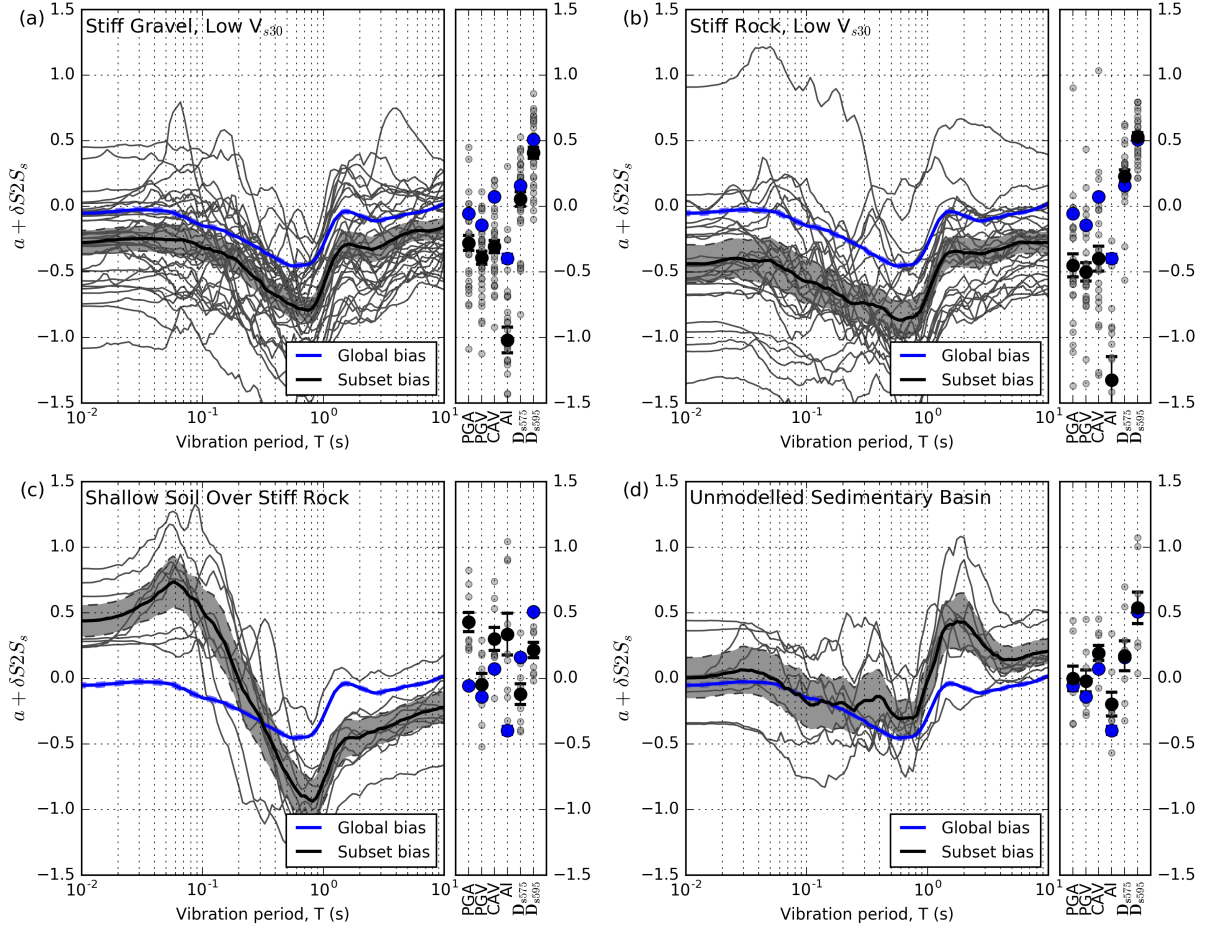


Figure 17: Bias and systematic site-to-site residuals of station subcategories based on Modified simulation prediction: (a) stiff gravel sites with V_{s30} that is too low; (b) stiff rock sites with V_{s30} that is too low; (c) shallow soil overlying stiff rock sites; and (d) sites located in a sedimentary basin that is not modelled in the NZVM. Blue lines show the global model prediction bias, a , for the Modified simulation while the grey lines show $a + \delta S2S_s$ for each station in the subcategory, and the black line is the average of the grey lines. Blue- and grey-shaded regions reflect the standard error in the a and $a + \delta S2S_s$ estimates, respectively.

602 8 Discussion

603 Throughout this paper, several further pathways for improved simulation prediction were
 604 identified. In this section, further discussion is presented on the underlying theoretical
 605 concepts, their potential implementation, and expected outcomes. Additionally, ideas
 606 which were not explicitly highlighted in the prior analysis are also discussed.

607 8.1 Spatially-Varying Stress Parameter

608 Analysis of the spatial variation of δB_e across NZ for short-period pSA provided evidence
609 toward a spatially-varying stress parameter for the HF simulations. While a spatial model
610 of stress parameter in NZ does not exist, comparisons of δB_e from the simulations against
611 inferred stress parameters from spectral inversion studies provide a basis for a prelim-
612 inary study to quantify the potential predictive improvement. Two independent stress
613 parameter studies have been recently carried out in NZ: Oth and Kaiser (2014) for the
614 2010-2011 Canterbury earthquake sequence, and Ren et al. (2018) for the 2016 Kaikōura
615 earthquake sequence. As the studies make different modelling assumptions (such as source
616 spectra model and reference site conditions), the estimated stress parameter values can
617 not be directly combined (Atkinson and Beresnev, 1997) and are therefore compared to
618 the simulations separately.

619 Of the 479 earthquake events simulated in this study, 158 were also considered in
620 Oth and Kaiser (2014) and 79 in Ren et al. (2018). Figure 18 presents histograms of
621 the inferred stress parameters of the two studies and corresponding summary statistics.
622 Comparison between the Modified simulation δB_e in this study and the inferred stress
623 parameters from these other two studies shows positive correlations at short-period pSA.
624 Figure 19a presents this comparison for PGA where the positive correlation can be seen,
625 while Figure 19b provides the summary of correlation coefficients for each study across
626 all periods. Overall, the short-period correlation coefficient is roughly $\rho_{OK} = 0.3$ for Oth
627 and Kaiser (2014) and $\rho_R = 0.5$ for Ren et al. (2018). While some studies have equated
628 ground-motion between-event variability with stress parameter variation in a random
629 vibration theory construct (i.e., Cotton et al. (2013)), the result shown here with $\rho << 1$
630 illustrates the nature of this idealization.

631 Preliminary simulations of the same events in this study were run with revised stress
632 parameters considering its correlation with δB_e (i.e., Figure 19) and it was found, as
633 expected, to significantly reduce between-event variability. However, the direct use of
634 δB_e for calculation of stress parameter is not possible for forward prediction of future
635 earthquake ground motions. One possibility would be to develop a spatially-varying

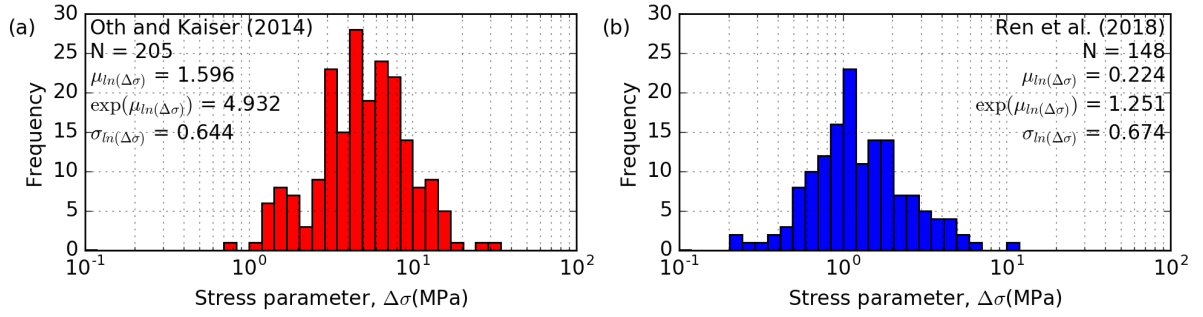


Figure 18: Distribution of inferred stress parameter of all events considered from spectral inversion studies: (a) Oth and Kaiser (2014), and (b) Ren et al. (2018).

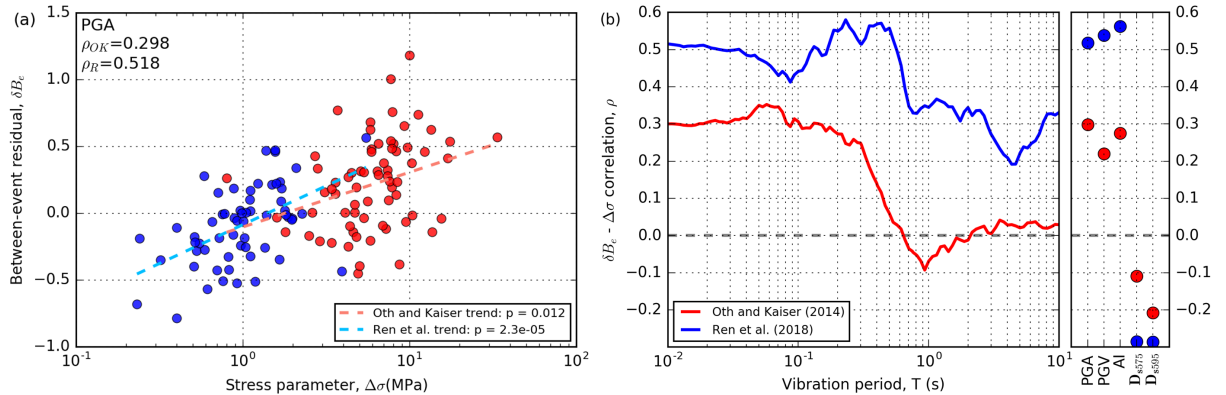


Figure 19: Correlation statistics of between-event residual and inferred stress parameter from Oth and Kaiser (2014) and Ren et al. (2018) for: (a) PGA as an example, and (b) summary for all IMs.

636 coefficient model of stress parameter across NZ based on the geostatistical Kriging of δB_e
 637 presented here which can be used in ground-motion simulations for active shallow crustal
 638 earthquakes (to provide mean and standard deviations of stress parameter).

639 8.2 HF Duration Modification for Soft Soil Sites

640 Systematic underprediction of significant durations at low V_{s30} sites was highlighted (from
 641 comparison of $\delta S2S_s$ and V_{s30}) and assumed to be due to the lack of site consideration
 642 in the HF simulation duration, which currently consists of only source and path com-
 643 ponents. The source component is simply the inverse of the Fourier amplitude spectra
 644 corner frequency and the path component depends only on R_{rup} for both GP10 and BT14
 645 models used in the Standard and Modified simulations, respectively. The BT14 model
 646 was developed using the NGA-West2 database and therefore corresponds to a duration

647 that is representative of the database's 'average' site (since there is no site dependence).
648 However, the percentage of records in the NGA-West2 database from sites with $V_{s30} \leq$
649 250 m/s is relatively small (approximately 7.5%, especially compared to 34.8% of such
650 sites in this study) and therefore the BT14 model gives path durations which are more
651 representative of a stiff soil or rock site. The residual analysis of Boore and Thompson
652 (2014) also identified this relative underprediction at low V_{s30} (as well as some weak M_w
653 and Z_{TOR} dependence) but those authors decided that the advantages of small adjust-
654 ments to the model to account for such biases did not outweigh the simplicity of the model
655 for applications. The range of V_{s30} for which there were no biases corresponded well to
656 the reference output velocities commonly used in 'stochastic' simulations (i.e., $V_{s30} \geq 500$
657 m/s) and their recommendations were to use the reference motions as inputs into local site
658 response modelling for sites with low V_{s30} values, which echo the sentiments of this study.
659 Additionally, it is also plausible to consider a V_{s30} -based empirical modification factor to
660 the HF path duration, analogous to the empirical site amplification for amplitudes.

661 8.3 V_{s30} Model Sensitivity

662 The V_{s30} used for empirical site amplification was shown to be a significant contributor to
663 model prediction bias and uncertainty. While this study used a combination of measured
664 values and estimated values from the Foster et al. (2019) model, it is acknowledged that
665 there are other V_{s30} models available which can provide values at many ground-motion
666 recording stations, such as Kaiser et al. (2017). However, Kaiser et al. (2017) is primarily
667 based on geologic categories, similar to the Foster et al. (2019) model, and high-quality
668 estimates of V_{s30} from that model are also included in the Foster et al. (2019) model.
669 Preliminary simulations using V_{s30} values from Kaiser et al. (2017) resulted in minor
670 differences in model prediction bias and uncertainty compared to simulations using the
671 Foster et al. (2019) model. One subcategory where the Kaiser et al. (2017)-based results
672 perform better is with stiff rock sites (particularly broadband stations,) where high V_{s30}
673 values are prescribed, whereas Foster et al. (2019) generally predicts values that are
674 considered as too low. The benefit of Foster et al. (2019) is its ability to prescribe V_{s30}

675 at any arbitrary location in NZ, which is important for many seismic hazard analysis
676 applications. To improve such models, subsequent research toward the V_{s30} estimation
677 method and increasing the number of V_{s30} measurements are clearly necessary.

678 8.4 Examination of Topographic Effects

679 As the LF and HF simulations both do not consider explicit topographic representation
680 in the wave propagation or near-surface site response, biases associated with topographic
681 effects may exist. This possibility is examined through comparisons of $\delta S2S_s$ and relative
682 elevation (the ratio of elevation at the site to the average surrounding elevation), a simple
683 proxy for topographic character (Rai et al., 2016). 250 m and 1250 m relative elevation
684 (H_{250} and H_{1250} , respectively, where the distance is the radius over which elevation is
685 averaged) were calculated from digital elevation model rasters with a 25 m grid resolu-
686 tion. Comparisons of $\delta S2S_s$ against H_{250} and H_{1250} for PGA, pSA(2.0s) and D_{s595} for
687 the Standard and Modified simulations, and empirical prediction are presented in Elec-
688 tronic Supplement E. While the locally weighted linear regression lines often deviate from
689 $\delta S2S_s = 0$, it is difficult to determine any systematic trends as most of the data (73.1%)
690 lies in the range of $-15 \leq H_{250} \leq 15$ (and roughly equivalent ranges for H_{1250}) which gen-
691 erally corresponds to no evident topographic effects (Rai et al., 2016, 2017). Therefore,
692 while some biases may exist due to topographic effects, the current residual analysis via
693 H_{250} and H_{1250} metrics is not able to diagnose it. Topographic effects may be considered
694 in simulations either explicitly (through appropriate meshing in finite element methods),
695 through additional 2D or 3D site response analyses which model the topographic features,
696 or using empirical topographic amplification factors.

697 9 Conclusions

698 This paper has provided a comprehensive validation of the Graves and Pitarka (2010,
699 2015, 2016) hybrid broadband ground-motion simulation method in a NZ context with
700 small M_w active shallow crustal point source ruptures using an extensive set of 5218

701 ground motions recorded at 212 sites from 479 earthquakes. The simulations utilized
702 recent models of crustal velocity and near-surface site characteristics, as well as a Modified
703 simulation method based on previous validation for active shallow crustal events. Ground-
704 motion predictions using the Standard and Modified simulations, as well as commonly-
705 used empirical predictions for benchmarking purposes, were compared against observed
706 ground motions to quantify their predictive capability, and identify biases and potential
707 improvements.

708 Through the validation considering the entire dataset, it was found that the modifica-
709 tions in the Modified simulations reduced the overprediction bias of pSA across all periods
710 and drastically reduced the underprediction bias of significant durations. The spatial dis-
711 tribution and high correlation of δB_e between methods indicated that modelling of the
712 spatial variation of source parameters, such as the stress parameter, could improve the
713 prediction. Likewise for $\delta S2S_s$, the spatial distribution and high correlation indicated
714 that changes to the modelling of near-surface site response, such as explicit physics-based
715 wave propagation methods, could improve the prediction. This advanced approach to
716 site response would also improve the underprediction of significant durations at soft soil
717 sites (relative to stiffer sites, based on V_{s30}), where site contributions to ground-motion
718 duration are large, which was identified in comparisons between $\delta S2S_s$ and V_{s30} . Lastly, a
719 station subcategory analysis identified specific types of sites which appeared to be system-
720 atically biased, such as inland stiff gravel sites and stiff rock sites, which have estimated
721 V_{s30} values from Foster et al. (2019) that are expected to be too low, resulting in overam-
722 plification from the V_{s30} -based empirical site amplification. Improvements to the Foster
723 et al. (2019) model to better characterise such sites would lead to improved prediction.

724 To extend the findings of this study, future work should consider moderate and large
725 M_w earthquakes, which would require additional attention to source modelling as the
726 point source approximation would no longer be valid, as well as subduction earthquakes
727 where the fundamental source rupture and wave propagation processes may differ from
728 active shallow crustal earthquakes. Additional improvements can be made to crustal ve-
729 locity modelling to include explicit modelling of more sedimentary basins in the NZVM

730 with the aim of complete NZ-wide coverage with simple topographically-inferred models,
731 followed by more refined models incorporating available subsurface data. Inclusion of
732 small-scale crustal velocity heterogeneities will also be important for appropriately sim-
733 ulating high frequencies deterministically and would increase simulated ground-motion
734 durations through wave-scattering. Finally, the uncertainty in simulations needs to be
735 explicitly quantified for use in probabilistic seismic hazard analyses.

736 **10 Data and resources**

737 Earthquake source descriptions used in this study were obtained from the GeoNet
738 New Zealand earthquake centroid moment tensor catalogue (<https://github.com/>
739 `GeoNet/data/tree/master/moment-tensor`), recorded ground motions were obtained
740 from the GeoNet file transfer protocol (<ftp://ftp.geonet.org.nz/strong/>), the 3D
741 crustal velocity models were created using the NZVM code (<https://github.com/>
742 `ucgmsim/Velocity-Model`), estimated V_{s30} were obtained from <https://github.com/>
743 `fostergeotech/Vs30_NZ`, and measured V_{s30} values were provided by Dr Liam Wothe-
744 spoon.

745 The ground-motion simulations were computed on NeSI high performance comput-
746 ing resources using the workflow developed by the QuakeCoRE Technology Platform 4
747 (https://github.com/ucgmsim/slurm_gm_workflow). Linear mixed effects regression
748 was carried out using the lme4 package on RStudio.

749 Figures were prepared using Generic Mapping Tools ([http://gmt.soest.hawaii.](http://gmt.soest.hawaii.edu/)
750 `edu/`), Python (<https://www.python.org/>) and Matplotlib (<https://matplotlib.org/>).
751

752 **11 Acknowledgements**

753 Financial support of this research from the University of Canterbury, QuakeCoRE: The
754 NZ Centre for Earthquake Resilience, Royal Society of New Zealand's Marsden Fund,
755 Rutherford Discovery Fellowship and Rutherford Postdoctoral Fellowship are greatly ap-

756 appreciated. High performance computing resources under the NeSI merit allocation are
757 also greatly appreciated. The authors would like to thank Ruizhi Wen and Yefei Ren
758 for providing data from their work on the 2016 Kaikōura earthquake sequence. This is
759 QuakeCoRE publication number... .

760 **References**

- 761 Afshari, K. and Stewart, J. P. (2016). Physically parameterized prediction equations for
762 significant duration in active crustal regions. *Earthquake Spectra*, 32(4):2057–2081.
- 763 Al Atik, L., Abrahamson, N., Bommer, J. J., Scherbaum, F., Cotton, F., and Kuehn,
764 N. (2010). The variability of ground-motion prediction models and its components.
765 *Seismological Research Letters*, 81(5):794–801.
- 766 Ancheta, T. D., Darragh, R. B., Stewart, J. P., Seyhan, E., Silva, W. J., Chiou, B. S.-J.,
767 Wooddell, K. E., Graves, R. W., Kottke, A. R., Boore, D. M., et al. (2014). Nga-west2
768 database. *Earthquake Spectra*, 30(3):989–1005.
- 769 Atkinson, G. M. and Assatourians, K. (2015). Implementation and validation of exsim
770 (a stochastic finite-fault ground-motion simulation algorithm) on the scec broadband
771 platform. *Seismological Research Letters*, 86(1):48–60.
- 772 Atkinson, G. M. and Beresnev, I. (1997). Don't call it stress drop. *Seismological Research
773 Letters*, 68(1):3–4.
- 774 Bates, D., Mächler, M., Bolker, B., and Walker, S. (2015). Fitting linear mixed-effects
775 models using lme4. *Journal of Statistical Software*, 67(1):1–48.
- 776 Bellagamba, X., Lee, R., and Bradley, B. A. (2019). A neural network for automated qual-
777 ity screening of ground motion records from small magnitude earthquakes. *Earthquake
778 Spectra*, 35(4):1637–1661.
- 779 Bijelić, N., Lin, T., and Deierlein, G. G. (2018). Validation of the scec broadband platform
780 simulations for tall building risk assessments considering spectral shape and duration of
781 the ground motion. *Earthquake Engineering & Structural Dynamics*, 47(11):2233–2251.
- 782 Boore, D. M. and Bommer, J. J. (2005). Processing of strong-motion accelerograms:
783 needs, options and consequences. *Soil Dynamics and Earthquake Engineering*, 25(2):93–
784 115.
- 785 Boore, D. M., Joyner, W. B., and Fumal, T. E. (1993). Estimation of response spectra
786 and peak accelerations from western north american earthquakes: an interim report.
787 Technical report, US Geological Survey.
- 788 Boore, D. M., Stewart, J. P., Seyhan, E., and Atkinson, G. M. (2014). Nga-west2 equations
789 for predicting pga, pgv, and 5% damped psa for shallow crustal earthquakes. *Earthquake
790 Spectra*, 30(3):1057–1085.
- 791 Boore, D. M. and Thompson, E. M. (2014). Path durations for use in the stochastic-
792 method simulation of ground motions. *Bulletin of the Seismological Society of America*,
793 104(5):2541–2552.
- 794 Bora, S. S., Scherbaum, F., Kuehn, N., and Stafford, P. (2016). On the relationship
795 between fourier and response spectra: Implications for the adjustment of empirical
796 ground-motion prediction equations (gmpe). *Bulletin of the Seismological Society of
797 America*, 106(3):1235–1253.

- 798 Bradley, B. A. (2013). A New Zealand-specific pseudospectral acceleration ground-motion
799 prediction equation for active shallow crustal earthquakes based on foreign models.
800 *Bulletin of the Seismological Society of America*, 103(3):1801–1822.
- 801 Bradley, B. A. (2015). Systematic ground motion observations in the canterbury earth-
802 quakes and region-specific non-ergodic empirical ground motion modeling. *Earthquake*
803 *Spectra*, 31(3):1735–1761.
- 804 Bradley, B. A., Pettinga, D., Baker, J. W., and Fraser, J. (2017a). Guidance on the
805 utilization of earthquake-induced ground motion simulations in engineering practice.
806 *Earthquake Spectra*, 33(3):809–835.
- 807 Bradley, B. A., Razafindrakoto, H. N., and Polak, V. (2017b). Ground-motion observa-
808 tions from the 14 november 2016 m_w 7.8 kaikoura, new zealand, earthquake and insights
809 from broadband simulations. *Seismological Research Letters*, 88(3):740–756.
- 810 Brune, J. N. (1970). Tectonic stress and the spectra of seismic shear waves from earth-
811 quakes. *Journal of geophysical research*, 75(26):4997–5009.
- 812 Campbell, K. W. and Bozorgnia, Y. (2010). A ground motion prediction equation for
813 the horizontal component of cumulative absolute velocity (cav) based on the peer-nga
814 strong motion database. *Earthquake Spectra*, 26(3):635–650.
- 815 Campbell, K. W. and Bozorgnia, Y. (2012). A comparison of ground motion predic-
816 tion equations for arias intensity and cumulative absolute velocity developed using a
817 consistent database and functional form. *Earthquake Spectra*, 28(3):931–941.
- 818 Campbell, K. W. and Bozorgnia, Y. (2014). Nga-west2 ground motion model for the
819 average horizontal components of pga, pgv, and 5% damped linear acceleration response
820 spectra. *Earthquake Spectra*, 30(3):1087–1115.
- 821 Chiou, B., Youngs, R., Abrahamson, N., and Addo, K. (2010). Ground-motion atten-
822 uation model for small-to-moderate shallow crustal earthquakes in california and its
823 implications on regionalization of ground-motion prediction models. *Earthquake spec-
824 tra*, 26(4):907–926.
- 825 Cotton, F., Archuleta, R., and Causse, M. (2013). What is sigma of the stress drop?
826 *Seismological Research Letters*, 84(1):42–48.
- 827 Crempien, J. G. and Archuleta, R. J. (2015). Ucsb method for simulation of broadband
828 ground motion from kinematic earthquake sources. *Seismological Research Letters*,
829 86(1):61–67.
- 830 de la Torre, C., Bradley, B. A., and Lee, R. L. (2020). Modeling Nonlinear Site
831 Effects in Physics-Based Ground Motion Simulations of the 2010–2011 Canter-
832 bury Earthquake Sequence. *Earthquake Spectra (in press)*. Available online at
833 10.1177/8755293019891729.
- 834 Dreger, D. S. and Jordan, T. H. (2015). Introduction to the focus section on validation of
835 the scec broadband platform v14. 3 simulation methods. *Seismological Research Letters*,
836 86(1):15–16.

- 837 Eberhart-Phillips, D., Reyners, M., Bannister, S., Chadwick, M., and Ellis, S. (2010).
838 Establishing a versatile 3-D seismic velocity model for New Zealand. *Seismological*
839 *Research Letters*, 81(6):992–1000.
- 840 Ely, G. P., Jordan, T., Small, P., and Maechling, P. J. (2010). A vs30-derived nearsurface
841 seismic velocity model. In *Abstract S51A-1907, Fall Meeting*. AGU San Francisco, CA.
- 842 Foster, K. M., Bradley, B. A., McGann, C. R., and Wotherspoon, L. M. (2019). A
843 vs30 map for new zealand based on geologic and terrain proxy variables and field
844 measurements. *Earthquake Spectra*, 0(0):null.
- 845 Frankel, A. (2009). A constant stress-drop model for producing broadband synthetic
846 seismograms: Comparison with the next generation attenuation relations. *Bulletin of*
847 *the Seismological Society of America*, 99(2A):664–680.
- 848 Galasso, C., Zhong, P., Zareian, F., Iervolino, I., and Graves, R. W. (2013). Validation
849 of ground-motion simulations for historical events using mdof systems. *Earthquake*
850 *Engineering & Structural Dynamics*, 42(9):1395–1412.
- 851 Goulet, C. A., Abrahamson, N. A., Somerville, P. G., and Wooddell, K. E. (2015). The
852 scec broadband platform validation exercise: Methodology for code validation in the
853 context of seismic-hazard analyses. *Seismological Research Letters*, 86(1):17–26.
- 854 Graves, R., Jordan, T. H., Callaghan, S., Deelman, E., Field, E., Juve, G., Kesselman,
855 C., Maechling, P., Mehta, G., Milner, K., et al. (2011). Cybershake: A physics-based
856 seismic hazard model for southern california. *Pure and Applied Geophysics*, 168(3–
857 4):367–381.
- 858 Graves, R. and Pitarka, A. (2015). Refinements to the graves and pitarka (2010) broad-
859 band ground-motion simulation method. *Seismological Research Letters*, 86(1):75–80.
- 860 Graves, R. and Pitarka, A. (2016). Kinematic ground-motion simulations on rough faults
861 including effects of 3d stochastic velocity perturbations. *Bulletin of the Seismological*
862 *Society of America*, 106(5):2136–2153.
- 863 Graves, R. W. and Pitarka, A. (2010). Broadband ground-motion simulation using a
864 hybrid approach. *Bulletin of the Seismological Society of America*, 100(5A):2095–2123.
- 865 Harmsen, S., Hartzell, S., and Liu, P. (2008). Simulated ground motion in santa clara
866 valley, california, and vicinity from m 6.7 scenario earthquakes. *Bulletin of the Seismo-*
867 *logical Society of America*, 98(3):1243–1271.
- 868 Hartzell, S., Leeds, A., Frankel, A., Williams, R. A., Odum, J., Stephenson, W., and Silva,
869 W. (2002). Simulation of broadband ground motion including nonlinear soil effects for
870 a magnitude 6.5 earthquake on the seattle fault, seattle, washington. *Bulletin of the*
871 *Seismological Society of America*, 92(2):831–853.
- 872 Jeong, S. and Bradley, B. A. (2017a). Amplification of strong ground motions at heathcote
873 valley during the 2010–2011 canterbury earthquakes: Observation and 1d site response
874 analysis. *Soil Dynamics and Earthquake Engineering*, 100:345–356.

- 875 Jeong, S. and Bradley, B. A. (2017b). Amplification of strong ground motions at heathcote
876 valley during the 2010–2011 canterbury earthquakes: The role of 2d nonlinear site
877 response. *Bulletin of the Seismological Society of America*, 107(5):2117–2130. In press.
- 878 Kaiser, A., Van Houtte, C., Perrin, N., Wotherspoon, L., and McVerry, G. (2017). Site
879 characterisation of geonet stations for the new zealand strong motion database. *Bulletin*
880 *of the New Zealand Society for Earthquake Engineering*, 50(1):39–49.
- 881 Lee, R. L., Bradley, B. A., Stafford, P. J., Graves, R. W., and Rodriguez-Marek, A.
882 (2020). Hybrid broadband ground motion simulation validation of small magnitude
883 earthquakes in canterbury, new zealand. *Earthquake Spectra*, 36(2):673–699.
- 884 Leonard, M. (2010). Earthquake fault scaling: Self-consistent relating of rupture length,
885 width, average displacement, and moment release. *Bulletin of the Seismological Society*
886 *of America*, 100(5A):1971–1988.
- 887 Maufroy, E., Chaljub, E., Hollender, F., Bard, P.-Y., Kristek, J., Moczo, P., De Martin,
888 F., Theodoulidis, N., Manakou, M., Guyonnet-Benaize, C., et al. (2016). 3d numerical
889 simulation and ground motion prediction: Verification, validation and beyond—lessons
890 from the e2vp project. *Soil Dynamics and Earthquake Engineering*, 91:53–71.
- 891 Maufroy, E., Chaljub, E., Hollender, F., Kristek, J., Moczo, P., Klin, P., Priolo, E., Iwaki,
892 A., Iwata, T., Etienne, V., et al. (2015). Earthquake ground motion in the mygdonian
893 basin, greece: the e2vp verification and validation of 3d numerical simulation up to 4
894 hz. *Bulletin of the Seismological Society of America*, 105(3):1398–1418.
- 895 New Zealand Standards (2004). Structural design actions - part 5: Earthquake actions -
896 new zealand. Standard, Standards New Zealand, Wellington, New Zealand.
- 897 Olsen, K. and Takedatsu, R. (2015). The sdsu broadband ground-motion generation
898 module bbtoolbox version 1.5. *Seismological Research Letters*, 86(1):81–88.
- 899 Oth, A. and Kaiser, A. E. (2014). Stress release and source scaling of the 2010–2011
900 canterbury, new zealand earthquake sequence from spectral inversion of ground motion
901 data. *Pure and Applied Geophysics*, 171(10):2767–2782.
- 902 Rai, M., Rodriguez-Marek, A., and Chiou, B. S. (2017). Empirical terrain-based topo-
903 graphic modification factors for use in ground motion prediction. *Earthquake Spectra*,
904 33(1):157–177.
- 905 Rai, M., Rodriguez-Marek, A., and Yong, A. (2016). An empirical model to predict to-
906 topographic effects in strong ground motion using california small-to medium-magnitude
907 earthquake database. *Earthquake Spectra*, 32(2):1033–1054.
- 908 Razafindrakoto, H. N., Bradley, B. A., and Graves, R. W. (2018). Broadband Ground-
909 Motion Simulation of the 2011 M_w 6.2 Christchurch Earthquake, New Zealand. *Bulletin*
910 *of the Seismological Society of America*, 108(4):2130–2147.
- 911 Ren, Y., Zhou, Y., Wang, H., and Wen, R. (2018). Source characteristics, site effects, and
912 path attenuation from spectral analysis of strong-motion recordings in the 2016 kaikōura
913 earthquake sequencesource characteristics, site effects, and path attenuation of strong-
914 motion recordings. *Bulletin of the Seismological Society of America*, 108(3B):1757–1773.

- 915 Ristau, J. (2008). Implementation of routine regional moment tensor analysis in new
916 zealand. *Seismological Research Letters*, 79(3):400–415.
- 917 Ristau, J. (2013). Update of regional moment tensor analysis for earthquakes in new
918 zealand and adjacent offshore regions. *Bulletin of the Seismological Society of America*,
919 103(4):2520–2533.
- 920 Ristau, J. (2018). Overview of moment tensor analysis in new zealand. In *Moment Tensor
921 Solutions*, pages 281–305. Springer.
- 922 Rodriguez-Marek, A., Montalva, G. A., Cotton, F., and Bonilla, F. (2011). Analysis of
923 single-station standard deviation using the kik-net data. *Bulletin of the Seismological
924 Society of America*, 101(3):1242–1258.
- 925 Roten, D., Olsen, K., and Pechmann, J. (2012). 3d simulations of m 7 earthquakes on
926 the wasatch fault, utah, part ii: Broadband (0–10 hz) ground motions and nonlinear
927 soil behavior. *Bulletin of the Seismological Society of America*, 102(5):2008–2030.
- 928 Savran, W. and Olsen, K. (2019). Ground motion simulation and validation of the
929 2008 chino hills earthquake in scattering media. *Geophysical Journal International*,
930 219(3):1836–1850.
- 931 Stafford, P. J. (2014). Crossed and nested mixed-effects approaches for enhanced model
932 development and removal of the ergodic assumption in empirical ground-motion models.
933 *Bulletin of the Seismological Society of America*, 104(2):702–719.
- 934 Taborda, R., Azizzadeh-Roodpis, S., Khoshnevis, N., and Cheng, K. (2016). Evaluation
935 of the southern california seismic velocity models through simulation of recorded events.
936 *Geophysical Journal International*, 205(3):1342–1364.
- 937 Thomson, E. M., Bradley, B. A., and Lee, R. L. (2019). Methodology and computational
938 implementation of a new zealand velocity model (nzvm2. 0) for broadband ground
939 motion simulation. *New Zealand Journal of Geology and Geophysics*, pages 1–18.
- 940 Wirth, E. A., Frankel, A. D., and Vidale, J. E. (2017). Evaluating a kinematic method
941 for generating broadband ground motions for great subduction zone earthquakes: Ap-
942 plication to the 2003 mw 8.3 tokachi-oki earthquakeevaluating a kinematic method for
943 generating broadband ground motions. *Bulletin of the Seismological Society of America*,
944 107(4):1737–1753.
- 945 Withers, K. B., Olsen, K. B., Shi, Z., and Day, S. M. (2019). Validation of deterministic
946 broadband ground motion and variability from dynamic rupture simulations of buried
947 thrust earthquakesvalidation of deterministic broadband ground motion and variability.
948 *Bulletin of the Seismological Society of America*, 109(1):212–228.
- 949 Yenier, E. and Atkinson, G. M. (2015). An equivalent point-source model for stochastic
950 simulation of earthquake ground motions in california. *Bulletin of the Seismological
951 Society of America*, 105(3):1435–1455.

952 **Appendices**

953 **A Electronic Supplement A: Event Information**

954 Table A.1 provides details and metadata of the 479 earthquake events including public
955 ID, date, geographic location, source characteristics and number of sites which recorded
956 the event.

Table A.1: Earthquake event date, location and source characteristics.

Event ID	Date	Longitude (°)	Latitude (°)	M_w	CD (km)	Strike (°)	Dip (°)	Rake (°)	NS _e
2122842	29/09/2003	172.923096	-43.2859	4.5	20	49	85	12	8
2128373	14/10/2003	172.8909	-43.288898	3.9	18	283	60	80	5
2252479	23/06/2004	171.379395	-42.831501	4.7	8	166	74	34	4
2266910	19/07/2004	172.493896	-41.738499	4.4	16	17	51	96	5
2302372	02/10/2004	173.137405	-42.341202	4.6	10	53	75	148	3
2352244	16/01/2005	171.056198	-43.209702	4.1	4	26	54	123	3
2353002	18/01/2005	175.801193	-41.4636	4.9	8	358	84	60	10
2378887	19/03/2005	171.621796	-43.219799	4	8	0	79	22	3
2442827	06/08/2005	171.670898	-41.956501	4.2	12	204	48	106	5
2450807	24/08/2005	170.766602	-43.209301	4.1	4	243	88	104	4
2453272	30/08/2005	177.301605	-39.660099	3.9	20	351	56	-92	4
2471995	12/10/2005	171.676605	-42.032799	4.2	6	331	82	9	5
2472534	13/10/2005	172.483597	-42.678398	4.5	10	68	74	158	5
2480520	31/10/2005	174.185898	-41.659599	4.1	6	75	68	-151	3
2480685	01/11/2005	174.190796	-41.658501	4.5	6	250	74	-159	4
2481737	03/11/2005	174.262802	-41.741798	4.5	16	156	81	-46	5
2618685	10/04/2005	171.027206	-42.9995	3.8	4	194	57	75	3
2626467	02/05/2005	169.037704	-43.951199	5	14	62	82	167	4
2706265	07/03/2007	175.351898	-40.380402	4.3	20	27	64	90	4
2717514	30/03/2007	176.730499	-37.897598	3.9	16	199	78	149	3
2733202	02/05/2007	176.736801	-37.906601	3.9	8	38	79	-134	3
2800955	29/09/2007	176.824493	-37.775902	4.7	8	214	54	-129	3
2808426	15/10/2007	167.146393	-44.8269	4.5	18	193	59	66	3
2812053	24/10/2007	172.040405	-42.166401	4.5	6	141	89	-62	6
2836573	14/12/2007	176.822098	-37.781399	4	8	64	58	-93	3
2893675	13/04/2008	166.842194	-45.127602	4.8	8	179	65	58	3
2902528	01/05/2008	171.019501	-43.2253	4.5	5	240	64	141	3

Continued on next page

Table A.1 continued from previous page

Event ID	Date	Longitude (°)	Latitude (°)	M_w	CD (km)	Strike (°)	Dip (°)	Rake (°)	NS _e
2937330	12/07/2008	172.830994	-42.7243	4	12	337	89	-34	3
2964018	05/09/2008	172.713104	-42.376598	4.5	7	71	83	165	7
2974058	24/09/2008	173.908493	-42.339001	5	16	206	45	85	4
2974665	26/09/2008	173.913193	-42.306499	5	16	222	48	112	4
3010357	05/12/2008	169.196198	-43.8242	4.3	6	233	88	-122	5
3016538	17/12/2008	172.850906	-42.434898	4.6	6	246	83	-144	4
3074697	13/04/2009	171.599701	-43.490501	4	6	37	65	65	3
3252455	05/02/2010	167.392197	-44.7286	5	18	186	62	57	3
3275801	16/03/2010	173.903702	-42.1609	4.3	12	247	90	165	4
3307585	15/05/2010	177.682205	-38.087799	4.4	10	53	84	-169	3
3366213	03/09/2010	172.225906	-43.617699	4.6	16	64	85	161	14
3366241	03/09/2010	172.391098	-43.585899	4.4	4	152	74	-26	6
3366376	04/09/2010	172.333496	-43.597301	4.1	4	102	87	154	6
3366452	04/09/2010	171.96696	-43.571602	4.8	8	207	84	-22	17
3366499	04/09/2010	172.374695	-43.602402	4	10	176	69	27	7
3366503	04/09/2010	172.368393	-43.6021	4.3	6	351	89	21	7
3366504	04/09/2010	172.371597	-43.5923	4.4	6	160	90	-12	7
3366544	04/09/2010	171.855896	-43.5653	4.3	6	27	66	36	8
3366585	04/09/2010	172.381104	-43.622799	4	6	69	87	-173	7
3366586	04/09/2010	171.977295	-43.251999	4.6	8	154	83	16	9
3366726	04/09/2010	172.055496	-43.6147	4	8	259	75	-154	6
3366750	04/09/2010	172.1427	-43.626301	4.3	4	309	85	-23	6
3366751	04/09/2010	172.172501	-43.594898	4.7	6	232	88	154	9
3366858	04/09/2010	172.410904	-43.5709	4	8	352	88	-9	4
3366933	05/09/2010	172.382004	-43.630901	4.5	4	299	70	-91	10
3367278	05/09/2010	171.910599	-43.5947	4.2	6	243	55	114	5
3367476	06/09/2010	172.291794	-43.577702	4.1	16	339	86	7	9
3367535	06/09/2010	172.376297	-43.591999	4.1	10	255	84	170	10

Continued on next page

Table A.1 continued from previous page

Event ID	Date	Longitude (°)	Latitude (°)	M_w	CD (km)	Strike (°)	Dip (°)	Rake (°)	NS _e
3367608	06/09/2010	172.326401	-43.617901	4.2	8	244	83	166	11
3367742	06/09/2010	172.387802	-43.569901	4.8	6	350	85	23	18
3367749	06/09/2010	171.891403	-43.588501	5	6	232	51	84	16
3367765	06/09/2010	171.921402	-43.5439	4.2	8	212	48	68	6
3367832	06/09/2010	172.239899	-43.653999	4.8	12	245	73	160	23
3368287	07/09/2010	172.416199	-43.590099	4.3	6	265	84	-172	12
3368361	07/09/2010	172.159698	-43.511501	4.3	8	24	64	127	14
3368445	07/09/2010	172.690002	-43.574001	4.7	4	161	67	27	22
3368471	07/09/2010	172.397507	-43.557301	4	4	257	87	156	10
3368607	08/09/2010	172.370102	-43.618198	4	4	271	76	-159	11
3369048	08/09/2010	172.073593	-43.626202	4	6	241	67	136	6
3369682	09/09/2010	172.380203	-43.605701	4.2	8	324	88	8	15
3370677	11/09/2010	172.392303	-43.641998	4.2	6	321	54	-63	12
3370916	12/09/2010	172.387802	-43.590698	4.2	4	165	78	-13	13
3372087	14/09/2010	172.376205	-43.626999	4	4	346	73	18	10
3372561	15/09/2010	172.506699	-43.605	4	10	179	68	33	11
3372661	15/09/2010	172.495804	-43.628799	4	4	162	87	28	10
3373089	16/09/2010	172.448196	-43.611698	4	8	187	89	21	10
3373091	16/09/2010	172.462402	-43.639599	4.2	4	261	83	-157	10
3373119	16/09/2010	171.940903	-43.5574	4.1	4	107	63	134	7
3373723	17/09/2010	172.160599	-43.459301	4.1	6	147	78	13	10
3373925	17/09/2010	172.446503	-43.615101	4.2	10	180	83	16	12
3374803	19/09/2010	172.374298	-43.573502	4.2	8	182	88	6	12
3376639	22/09/2010	172.462296	-43.5602	4.1	6	57	81	154	10
3377148	23/09/2010	172.372192	-43.6082	4.2	8	69	86	168	12
3377880	24/09/2010	172.427399	-43.614498	4	10	261	78	151	9
3380440	29/09/2010	172.3806	-43.6278	4.1	6	173	72	21	12
3382676	04/10/2010	172.403107	-43.562698	4.8	4	149	76	-25	18

Continued on next page

Table A.1 continued from previous page

Event ID	Date	Longitude (°)	Latitude (°)	M_w	CD (km)	Strike (°)	Dip (°)	Rake (°)	NS _e
3384315	07/10/2010	172.329697	-43.737701	4	6	153	85	13	8
3388384	13/10/2010	172.413101	-43.589901	4.3	6	67	84	169	11
3389582	15/10/2010	172.485901	-43.6339	4.3	6	352	75	-21	13
3390805	17/10/2010	172.405807	-43.6166	4.1	8	188	70	26	11
3391440	18/10/2010	172.563599	-43.625599	4.8	4	246	84	159	20
3392462	19/10/2010	172.408707	-43.5933	4.1	8	80	90	167	10
3394581	24/10/2010	172.769394	-43.460098	4.4	4	353	69	36	13
3400620	01/11/2010	172.3797	-43.624802	4.2	4	273	81	-154	10
3403219	06/11/2010	172.059998	-43.2118	4.6	6	72	87	157	15
3406713	13/11/2010	172.395294	-43.600201	4.4	6	155	77	-18	12
3407078	14/11/2010	172.413101	-43.5989	4.4	6	157	87	-17	11
3413873	28/11/2010	175.533401	-40.876202	5	18	210	76	-103	29
3437366	26/12/2010	172.615997	-43.531601	4	4	72	87	166	9
3439993	01/01/2011	172.418304	-43.5522	4	4	153	87	5	8
3450113	19/01/2011	172.549698	-43.615299	4.8	8	177	80	15	17
3450491	20/01/2011	172.5186	-43.606602	4	8	178	74	21	9
3459803	03/02/2011	172.032806	-43.162399	4.2	10	159	89	-9	4
3460014	04/02/2011	172.357895	-43.632301	4.3	4	329	79	-29	12
3468622	22/02/2011	172.674805	-43.593102	4.4	8	91	86	175	4
3468666	22/02/2011	172.560303	-43.587299	4.1	8	64	70	153	7
3468672	22/02/2011	172.647003	-43.565201	4.5	4	342	89	-5	8
3468705	22/02/2011	172.751495	-43.602299	4.2	6	85	55	125	4
3468722	22/02/2011	172.740997	-43.626801	4	6	229	89	-155	3
3468746	22/02/2011	172.764999	-43.638599	4.3	6	149	79	-14	5
3468765	22/02/2011	172.724792	-43.620701	4.4	4	166	86	17	5
3468797	22/02/2011	172.560394	-43.599499	4.3	8	50	73	135	4
3468858	22/02/2011	172.695694	-43.5676	4.1	6	80	77	156	5
3468873	22/02/2011	172.692093	-43.604698	4	4	67	76	159	3

Continued on next page

Table A.1 continued from previous page

Event ID	Date	Longitude (°)	Latitude (°)	M_w	CD (km)	Strike (°)	Dip (°)	Rake (°)	NS _e
3468918	22/02/2011	172.716599	-43.580101	4.2	4	89	87	177	5
3468931	22/02/2011	172.676605	-43.605499	4.2	4	64	88	-173	6
3468980	22/02/2011	172.722702	-43.6036	4.3	4	246	83	-163	4
3469360	23/02/2011	172.751099	-43.5648	3.8	6	71	77	157	6
3470222	25/02/2011	172.660599	-43.579102	4.2	4	47	88	169	5
3471449	27/02/2011	172.848297	-43.598499	4	6	174	56	47	9
3471884	28/02/2011	172.846603	-43.615101	4.1	6	75	82	162	10
3474093	05/03/2011	172.733704	-43.5686	4.6	6	82	71	155	15
3474473	06/03/2011	173.897095	-42.3624	4.7	16	71	62	146	4
3476510	10/03/2011	172.739395	-43.5518	4.3	6	92	74	161	8
3478149	13/03/2011	172.898605	-43.544899	4.2	14	117	89	17	6
3481489	20/03/2011	172.697403	-43.521999	4.5	6	68	62	142	5
3495817	22/02/2011	172.631195	-43.594101	4.3	4	239	75	-163	6
3497857	16/04/2011	172.788605	-43.6134	5	4	83	89	165	37
3503071	26/04/2011	176.991699	-40.139702	4.4	15	225	88	111	4
3505099	29/04/2011	171.986801	-43.1842	4.9	7	69	90	151	25
3509905	09/05/2011	172.406799	-43.5994	4.9	6	149	79	-14	28
3525417	06/06/2011	172.4039	-43.584599	4.1	4	81	83	157	13
3528800	13/06/2011	172.155899	-43.366798	4	4	7	89	16	6
3529125	13/06/2011	172.738205	-43.595901	4.2	6	88	86	145	16
3529424	14/06/2011	171.145004	-43.481201	4.5	8	249	87	-162	6
3529702	14/06/2011	172.838196	-43.646099	4.8	4	241	76	-154	18
3529858	15/06/2011	172.854706	-43.654598	4.6	3	330	87	26	18
3529888	15/06/2011	172.869507	-43.659401	4	5	74	88	154	10
3530742	16/06/2011	172.793198	-43.589699	4.1	8	69	86	164	14
3530917	17/06/2011	172.756607	-43.530602	4.3	4	273	80	-157	16
3530953	17/06/2011	172.769394	-43.601898	4.2	6	247	83	-160	15
3531220	17/06/2011	172.799805	-43.572701	4.1	4	276	90	-156	16

Continued on next page

Table A.1 continued from previous page

Event ID	Date	Longitude (°)	Latitude (°)	M_w	CD (km)	Strike (°)	Dip (°)	Rake (°)	NS _e
3533219	21/06/2011	172.528595	-43.594799	4.1	6	336	89	-2	14
3540318	04/07/2011	177.003006	-40.741699	4.8	18	51	49	117	4
3541921	07/07/2011	172.210495	-43.206699	4.1	16	81	84	164	12
3550173	21/07/2011	172.195404	-43.644501	4.7	6	47	83	-158	26
3550782	23/07/2011	173.131104	-42.1045	4	20	56	87	-174	4
3556574	03/08/2011	172.884201	-43.599899	4	6	244	87	-144	14
3566526	22/08/2011	172.074905	-43.5742	4	8	88	89	166	12
3571192	31/08/2011	172.441498	-43.6022	4.3	6	267	74	-157	20
3572067	01/09/2011	172.813705	-43.571098	4.6	6	161	84	-8	23
3577039	10/09/2011	172.763504	-43.603901	4.3	8	62	60	132	19
3590805	21/06/2011	172.530899	-43.597099	4.3	4	172	84	-17	9
3591999	09/10/2011	172.789902	-43.579899	4.9	6	250	86	-160	31
3603873	01/11/2011	174.292297	-41.634399	4.4	14	340	83	27	10
3631369	23/12/2011	172.800201	-43.525799	4.4	4	248	79	-141	24
3631409	23/12/2011	172.834503	-43.4734	4.2	6	215	65	87	19
3631432	23/12/2011	172.773407	-43.495499	4.7	4	210	56	77	29
3631755	23/12/2011	172.839706	-43.663799	4.9	4	254	80	163	38
3634529	29/12/2011	172.806595	-43.5341	4	6	245	86	-159	18
3634645	29/12/2011	172.800003	-43.4604	4.1	4	213	50	82	16
3635309	31/12/2011	172.775406	-43.5173	4.5	4	357	67	28	25
3791909	03/09/2010	172.402496	-43.6138	4.1	4	357	90	11	6
3792018	03/09/2010	172.159698	-43.554901	4.9	6	248	86	-175	15
2012p001403	01/01/2012	172.832504	-43.462502	4.8	4	222	53	101	31
2012p002254	01/01/2012	172.793503	-43.440701	3.8	4	242	60	124	5
2012p003376	02/01/2012	172.820099	-43.4473	4.6	4	24	55	64	28
2012p010301	04/01/2012	172.842606	-43.496201	4.4	6	212	54	73	26
2012p014309	06/01/2012	172.744202	-43.558201	4.2	6	209	51	87	21
2012p014905	06/01/2012	172.772705	-43.536301	4.8	4	76	67	129	37

Continued on next page

Table A.1 continued from previous page

Event ID	Date	Longitude (°)	Latitude (°)	M_w	CD (km)	Strike (°)	Dip (°)	Rake (°)	NS _e
2012p023269	09/01/2012	172.808807	-43.498299	3.8	6	41	63	134	10
2012p030624	12/01/2012	172.793198	-43.428799	4.3	4	61	57	111	20
2012p043955	17/01/2012	172.793594	-43.638699	3.7	6	166	84	15	13
2012p044955	17/01/2012	176.526306	-40.300098	4.4	6	30	78	110	5
2012p052719	20/01/2012	172.4151	-43.573601	3.9	8	87	78	165	15
2012p053801	20/01/2012	172.412399	-43.596901	3.7	8	88	89	-170	11
2012p058758	22/01/2012	172.780899	-43.521301	4.2	4	60	59	114	20
2012p071137	27/01/2012	172.255295	-43.5597	4.2	6	247	79	-163	21
2012p073274	28/01/2012	172.827698	-43.453899	3.9	6	56	59	133	10
2012p075555	28/01/2012	172.559006	-42.033199	4.2	11	173	80	43	4
2012p103394	08/02/2012	172.69402	-43.581299	3.8	8	91	72	152	15
2012p103840	08/02/2012	172.754395	-43.6259	3.9	6	78	68	138	15
2012p104038	08/02/2012	172.766205	-43.631699	3.8	4	252	81	-159	15
2012p123336	15/02/2012	172.781998	-43.5196	3.8	4	11	55	90	10
2012p142382	22/02/2012	172.770203	-43.483002	3.8	8	40	47	83	4
2012p149826	25/02/2012	172.832596	-43.462399	4.1	6	49	47	103	13
2012p161604	29/02/2012	172.372604	-43.575401	3.7	6	77	85	171	8
2012p167881	03/03/2012	172.758896	-43.492699	3.7	6	359	50	73	3
2012p206748	17/03/2012	172.7099	-43.602901	3.9	8	185	74	28	18
2012p260761	06/04/2012	172.370499	-43.582401	3.8	8	179	87	-18	19
2012p275677	12/04/2012	172.757004	-43.512901	4.2	8	74	87	175	22
2012p303845	22/04/2012	172.7836	-43.5243	3.8	4	231	62	116	18
2012p309560	24/04/2012	172.720795	-42.497398	4.1	10	52	67	149	4
2012p365028	15/05/2012	172.75	-43.4893	4.2	4	41	63	100	29
2012p378107	19/05/2012	172.408707	-43.608501	3.9	20	81	82	157	14
2012p378954	20/05/2012	172.767899	-43.567799	4.4	4	56	61	134	32
2012p392201	25/05/2012	172.772293	-43.534	5	6	222	48	83	35
2012p399212	27/05/2012	172.786499	-43.5033	4.3	6	46	52	107	23

Continued on next page

Table A.1 continued from previous page

Event ID	Date	Longitude (°)	Latitude (°)	M_w	CD (km)	Strike (°)	Dip (°)	Rake (°)	NS _e
2012p407935	30/05/2012	171.368607	-43.791199	4.4	18	248	81	-69	4
2012p413162	01/06/2012	172.761902	-43.579399	4.1	4	260	86	-152	22
2012p416981	03/06/2012	172.720001	-43.5331	3.9	4	23	66	104	18
2012p505798	06/07/2012	172.338303	-43.601501	4.7	8	226	89	-168	39
2012p517515	10/07/2012	172.541107	-43.638199	3.9	4	4	87	-9	25
2012p560243	26/07/2012	176.158493	-40.540798	4.9	10	11	79	87	11
2012p656266	30/08/2012	168.752396	-44.102402	4.8	6	158	80	18	5
2012p713691	21/09/2012	172.807098	-43.480701	4.2	6	67	58	118	27
2012p764736	09/10/2012	172.783707	-43.4692	3.9	6	11	46	101	22
2012p781523	16/10/2012	169.536606	-44.0438	4.2	4	65	89	-160	3
2012p801609	23/10/2012	172.861206	-43.480598	4	6	55	50	119	17
2012p988084	31/12/2012	173.567398	-39.2911	4.6	14	22	87	-177	3
2013p027657	11/01/2013	173.694107	-39.312599	4.1	20	197	81	-164	3
2013p049577	19/01/2013	172.456802	-43.603802	4.3	4	168	89	-15	24
2013p128381	17/02/2013	173.984802	-41.848301	4.3	14	55	86	175	4
2013p368016	17/05/2013	172.359207	-43.639301	3.9	4	341	76	-22	14
2013p538215	19/07/2013	174.429901	-41.536098	4.5	20	345	51	76	21
2013p542688	20/07/2013	174.3918	-41.570202	3.9	20	345	70	57	3
2013p542958	20/07/2013	174.348099	-41.620602	4.5	15	240	86	159	15
2013p543121	20/07/2013	174.388199	-41.568001	4.6	18	222	55	134	38
2013p543283	21/07/2013	174.344894	-41.611198	4.3	10	349	70	38	11
2013p543788	21/07/2013	174.367401	-41.547001	4.1	14	336	81	16	4
2013p544030	21/07/2013	174.400894	-41.5392	4.7	14	356	54	67	30
2013p544085	21/07/2013	174.294693	-41.648102	4.3	10	238	83	162	4
2013p544117	21/07/2013	174.246597	-41.649601	4.1	14	348	80	37	4
2013p544317	21/07/2013	174.303802	-41.6544	4.4	13	158	87	-7	16
2013p544344	21/07/2013	174.350998	-41.543598	4.3	14	346	75	51	20
2013p544418	21/07/2013	174.255005	-41.624199	3.9	20	240	78	161	3

Continued on next page

Table A.1 continued from previous page

Event ID	Date	Longitude (°)	Latitude (°)	M_w	CD (km)	Strike (°)	Dip (°)	Rake (°)	NS _e
2013p544668	21/07/2013	174.342606	-41.584599	4.4	17	340	85	10	10
2013p544960	21/07/2013	174.299194	-41.450298	5	10	263	84	-163	9
2013p544974	21/07/2013	174.291595	-41.455101	4.6	14	153	89	14	37
2013p545809	21/07/2013	174.255295	-41.601898	5	12	153	83	16	35
2013p545900	21/07/2013	174.233093	-41.673199	4.3	11	255	80	166	8
2013p546148	22/07/2013	174.326096	-41.560799	4.2	19	138	90	1	7
2013p546702	22/07/2013	174.215195	-41.653198	4.3	11	65	86	-159	7
2013p547077	22/07/2013	174.254303	-41.665901	4.2	15	203	79	151	4
2013p547469	22/07/2013	174.347305	-41.563099	4.4	17	47	90	178	27
2013p548356	22/07/2013	174.196198	-41.666599	4.4	9	250	90	-177	6
2013p548878	23/07/2013	174.222595	-41.644901	3.9	15	270	89	153	4
2013p550724	23/07/2013	174.229599	-41.681198	4	14	190	86	-26	5
2013p550922	23/07/2013	174.228394	-41.683899	4.1	7	167	78	-26	4
2013p551065	23/07/2013	174.240097	-41.755699	4.2	5	58	83	164	5
2013p552596	24/07/2013	174.395203	-41.7211	4.1	16	237	84	163	4
2013p552776	24/07/2013	174.227707	-41.6936	3.9	14	173	89	-6	3
2013p552956	24/07/2013	174.243698	-41.674301	3.9	19	221	84	-173	5
2013p554277	25/07/2013	174.156097	-41.739101	3.8	14	227	87	-160	3
2013p561823	27/07/2013	174.198502	-41.698002	4	4	77	86	163	5
2013p563639	28/07/2013	174.295502	-41.694801	4.9	12	259	85	169	41
2013p565386	29/07/2013	172.647293	-42.667	4.5	6	250	88	-130	6
2013p572271	31/07/2013	174.333801	-41.780998	4.1	10	23	49	75	4
2013p572878	31/07/2013	174.387497	-41.556702	4.5	19	229	53	126	33
2013p574429	01/08/2013	174.308807	-41.7178	4.7	13	214	46	105	24
2013p575071	01/08/2013	174.3927	-41.553101	4.2	15	350	62	45	21
2013p577138	02/08/2013	174.0979	-41.6996	4	5	262	86	-166	4
2013p611600	15/08/2013	174.151901	-41.709999	4.3	8	173	89	5	4
2013p614184	16/08/2013	174.313705	-41.687	4.8	14	339	57	61	27

Continued on next page

Table A.1 continued from previous page

Event ID	Date	Longitude (°)	Latitude (°)	M_w	CD (km)	Strike (°)	Dip (°)	Rake (°)	NS _e
2013p614268	16/08/2013	174.2854	-41.709999	4.7	18	214	66	129	33
2013p614345	16/08/2013	174.234207	-41.878601	4.5	7	228	88	153	5
2013p614487	16/08/2013	174.114502	-41.7379	4.8	16	245	90	-170	28
2013p615178	16/08/2013	174.320206	-41.695099	4.6	13	357	84	14	20
2013p616443	17/08/2013	174.139099	-41.7388	3.9	10	108	84	170	3
2013p616527	17/08/2013	173.924103	-41.739799	4	4	8	84	-11	3
2013p616691	17/08/2013	173.992294	-41.779301	4.7	6	140	85	11	14
2013p617640	17/08/2013	174.112106	-41.722801	4	15	159	89	-33	5
2013p618032	17/08/2013	174.102402	-41.730999	4.7	20	333	74	33	29
2013p618439	17/08/2013	174.087097	-41.761002	4.1	9	132	90	18	5
2013p619176	18/08/2013	174.147995	-41.762001	4.1	4	352	76	24	3
2013p624208	19/08/2013	174.222397	-41.7346	4.2	14	330	88	-14	4
2013p626288	20/08/2013	174.247299	-41.702301	3.9	16	233	66	144	3
2013p653606	30/08/2013	172.176498	-43.602299	4.1	9	243	83	152	15
2013p658515	01/09/2013	174.080505	-41.7481	3.9	7	151	83	11	4
2013p666224	04/09/2013	174.423492	-41.500301	4.8	18	243	83	170	42
2013p686840	12/09/2013	173.871094	-41.8325	4	9	54	88	166	4
2013p690484	13/09/2013	174.398895	-41.5686	4.1	9	148	87	6	8
2013p695265	15/09/2013	174.157196	-41.772499	3.8	17	133	88	14	3
2013p708602	20/09/2013	172.444305	-43.574902	3.9	7	180	78	15	25
2013p739681	01/10/2013	174.395599	-41.544102	4.5	20	230	64	138	33
2013p750727	05/10/2013	174.393295	-41.527699	4	15	333	75	35	9
2013p783083	17/10/2013	174.053894	-41.775902	4	10	227	86	-164	5
2013p817946	30/10/2013	172.397507	-43.564999	3.9	8	73	81	-161	22
2013p868761	18/11/2013	172.525208	-43.589699	4.3	7	67	85	156	20
2013p916300	06/12/2013	174.025101	-41.6954	4.3	14	153	87	-20	5
2014p083861	01/02/2014	173.098999	-42.3694	4	4	270	84	-142	3
2014p125882	16/02/2014	168.645203	-44.273701	4.5	9	168	68	69	3

Continued on next page

Table A.1 continued from previous page

Event ID	Date	Longitude (°)	Latitude (°)	M_w	CD (km)	Strike (°)	Dip (°)	Rake (°)	NS _e
2014p211339	20/03/2014	172.123901	-43.594898	3.5	7	194	69	58	3
2014p237547	29/03/2014	172.708801	-43.573299	3.8	6	188	68	30	27
2014p686520	12/09/2014	172.784897	-43.151798	4.1	9	41	53	94	14
2014p753812	06/10/2014	176.772293	-40.367699	4.5	19	153	90	1	5
2014p933966	12/12/2014	172.367004	-43.644699	4.2	4	284	70	-129	27
2014p952799	19/12/2014	178.002808	-38.2617	4.8	18	193	82	-112	10
2014p965622	24/12/2014	172.720398	-43.557499	4	9	66	71	155	25
2015p013444	05/01/2015	171.236298	-43.073299	4.5	6	256	86	172	11
2015p013973	06/01/2015	171.285797	-43.062801	4.6	8	252	82	150	15
2015p030316	12/01/2015	176.064194	-40.3773	4.3	15	359	85	71	10
2015p080815	30/01/2015	172.091904	-42.9627	3.8	9	57	88	-176	3
2015p150076	25/02/2015	173.352005	-41.912399	4.3	7	175	74	-25	6
2015p218255	22/03/2015	173.357605	-41.896702	3.9	7	81	89	161	3
2015p228514	26/03/2015	172.867401	-42.55698	3.9	6	250	63	-125	3
2015p278276	13/04/2015	178.360397	-37.929001	4.4	17	252	81	69	3
2015p278423	14/04/2015	178.354401	-37.9226	4.6	15	243	82	55	5
2015p302546	22/04/2015	174.308502	-41.7327	4	19	348	67	26	4
2015p330493	03/05/2015	171.757095	-42.986401	4	7	242	67	140	5
2015p353480	11/05/2015	172.068405	-43.140598	3.8	11	65	76	144	4
2015p362790	15/05/2015	174.097794	-41.687099	4.3	8	142	74	-58	5
2015p523441	13/07/2015	175.0383	-40.500301	4	18	161	64	40	3
2015p653589	30/08/2015	175.740906	-40.6451	4.1	17	225	76	-149	5
2015p706760	19/09/2015	172.528503	-42.276901	3.9	12	347	86	-14	3
2015p768685	12/10/2015	176.3255	-40.553902	4.2	20	12	83	82	7
2015p794154	21/10/2015	173.880493	-39.282398	4.4	11	282	80	12	3
2015p795690	22/10/2015	175.079895	-41.196098	4	7	344	67	70	19
2015p796404	22/10/2015	178.1203	-38.2607	4.8	11	18	69	-96	7
2015p913186	04/12/2015	170.903198	-43.2178	4.1	11	59	87	-170	4

Continued on next page

Table A.1 continued from previous page

Event ID	Date	Longitude (°)	Latitude (°)	M_w	CD (km)	Strike (°)	Dip (°)	Rake (°)	NS _e
2015p936904	13/12/2015	172.341293	-41.508701	4.3	7	341	82	21	4
2016p072907	27/01/2016	172.505295	-43.554501	3.9	5	69	75	148	18
2016p119534	14/02/2016	172.760696	-43.5257	4	4	87	85	-166	25
2016p140897	22/02/2016	174.254807	-41.891998	4.8	4	39	62	115	20
2016p155711	27/02/2016	176.455597	-40.3479	4.2	11	21	87	-93	6
2016p158394	28/02/2016	172.619797	-43.568001	4.1	4	156	80	12	29
2016p188781	10/03/2016	174.453598	-41.5952	4.2	18	230	76	149	12
2016p198476	14/03/2016	173.048203	-42.263599	4.8	11	66	87	160	11
2016p198491	14/03/2016	173.059097	-42.273102	4.3	11	56	84	167	8
2016p275188	11/04/2016	175.4944	-40.893002	4.9	18	240	71	-92	43
2016p355041	11/05/2016	172.701996	-43.5891	4.2	7	69	86	154	28
2016p356297	11/05/2016	175.422607	-40.917099	4.9	20	226	68	-93	42
2016p390950	24/05/2016	176.906601	-39.463402	4.1	15	5	80	49	7
2016p395423	26/05/2016	174.409698	-41.5228	4.1	16	53	79	145	11
2016p500086	04/07/2016	174.019608	-41.695599	4.1	11	164	89	20	4
2016p665425	03/09/2016	178.989395	-37.256401	5	14	12	75	92	3
2016p842451	07/11/2016	173.765198	-39.384102	4.7	17	191	90	146	3
2016p858455	13/11/2016	173.870102	-42.2701	4.6	7	54	63	134	3
2016p858527	13/11/2016	173.640106	-42.226601	4.4	8	62	83	167	3
2016p858603	13/11/2016	174.032501	-41.9011	4.7	12	124	88	6	6
2016p858704	13/11/2016	173.678802	-42.4147	4.9	4	12	66	61	9
2016p858788	13/11/2016	174.281296	-41.728199	4.4	19	338	65	38	10
2016p858803	13/11/2016	172.969894	-42.724602	4.4	6	216	46	103	6
2016p858815	13/11/2016	173.207901	-42.571499	4.6	6	33	71	105	5
2016p858828	13/11/2016	174.074493	-41.828899	4.5	16	333	87	28	6
2016p858848	13/11/2016	174.208405	-41.802799	4.8	17	59	87	-160	44
2016p858876	13/11/2016	174.051605	-41.877399	4.4	7	223	73	159	6
2016p858913	13/11/2016	174.149002	-41.7034	4.5	17	345	70	48	17

Continued on next page

Table A.1 continued from previous page

Event ID	Date	Longitude (°)	Latitude (°)	M_w	CD (km)	Strike (°)	Dip (°)	Rake (°)	NS _e
2016p859051	13/11/2016	173.815506	-42.312599	4.6	11	247	86	-145	4
2016p859060	13/11/2016	172.803604	-42.698299	4.6	4	244	76	-157	9
2016p859091	13/11/2016	173.916901	-42.367401	4.2	17	55	61	138	3
2016p859336	13/11/2016	173.543198	-42.3256	4.8	15	149	85	-10	11
2016p859378	13/11/2016	173.854599	-42.129398	4.8	8	45	51	118	8
2016p859439	13/11/2016	174.345703	-41.710899	4.9	20	337	53	81	53
2016p859625	14/11/2016	173.981003	-42.0522	4.9	16	239	84	154	7
2016p859872	14/11/2016	174.3871	-41.744099	4.7	20	352	47	84	23
2016p859920	14/11/2016	173.658203	-42.308899	4.6	11	236	80	-157	5
2016p859929	14/11/2016	173.595398	-42.1553	4.6	5	172	79	-16	7
2016p860053	14/11/2016	173.486603	-42.444099	4.8	11	70	75	147	11
2016p860189	14/11/2016	174.299301	-41.752899	4.4	7	56	72	154	8
2016p860435	14/11/2016	174.313004	-41.723301	4.1	18	148	86	-21	3
2016p860592	14/11/2016	173.297195	-42.5979	4.6	11	253	88	-124	8
2016p860725	14/11/2016	174.268204	-41.691898	4.5	19	209	50	122	18
2016p860729	14/11/2016	174.266205	-41.7052	4.8	19	326	78	13	17
2016p860810	14/11/2016	174.289703	-41.692501	4.2	12	152	86	-22	3
2016p860816	14/11/2016	173.626907	-42.4156	4.5	14	101	76	153	3
2016p860963	14/11/2016	174.308701	-41.731499	4.4	17	335	67	37	6
2016p861086	14/11/2016	173.141006	-42.7383	4.3	9	191	71	41	7
2016p861190	14/11/2016	174.172104	-41.652401	4.4	17	16	89	-168	7
2016p861251	14/11/2016	173.037903	-42.487801	4.7	4	36	63	89	12
2016p861632	14/11/2016	173.690399	-42.2626	4.9	15	46	66	124	12
2016p861719	14/11/2016	173.202103	-42.537701	4.1	4	52	65	97	4
2016p861727	14/11/2016	174.406998	-41.650902	4	10	236	85	-175	3
2016p862636	15/11/2016	174.011902	-42.560799	4.8	9	47	56	94	8
2016p862855	15/11/2016	174.230103	-41.712601	4.1	14	228	69	147	5
2016p863064	15/11/2016	173.2565	-42.508301	4.3	6	20	63	57	5

Continued on next page

Table A.1 continued from previous page

Event ID	Date	Longitude (°)	Latitude (°)	M_w	CD (km)	Strike (°)	Dip (°)	Rake (°)	NS _e
2016p863486	15/11/2016	173.413406	-42.628399	3.9	15	244	69	147	4
2016p863723	15/11/2016	174.181305	-41.690498	4.5	14	342	80	36	3
2016p864224	15/11/2016	173.570206	-42.4683	4.5	5	23	71	126	6
2016p864401	15/11/2016	174.3871	-41.655602	4.9	13	147	84	12	3
2016p864842	15/11/2016	174.039505	-41.834599	4.3	8	169	86	-38	6
2016p865404	16/11/2016	174.350998	-41.615398	4.3	13	339	58	42	14
2016p865557	16/11/2016	174.363495	-41.694698	4.4	14	165	70	45	18
2016p865907	16/11/2016	175.6763	-41.312099	4.5	8	2	81	92	36
2016p866561	16/11/2016	173.466003	-42.506599	4.6	13	317	82	20	8
2016p867480	16/11/2016	173.798492	-42.238899	4.5	18	214	45	97	10
2016p869561	17/11/2016	172.839493	-42.684399	4	11	338	80	23	3
2016p869603	17/11/2016	172.810699	-42.6712	4.1	4	258	73	-159	6
2016p869902	17/11/2016	172.522598	-42.827599	4.2	9	319	69	26	7
2016p869914	17/11/2016	173.804901	-42.285599	4.1	10	30	59	75	3
2016p869983	17/11/2016	173.811798	-42.1754	4.6	8	68	79	148	6
2016p870237	17/11/2016	174.079697	-41.932999	4	18	216	49	117	3
2016p870286	18/11/2016	174.396103	-41.676701	4.2	19	155	88	9	6
2016p871569	18/11/2016	174.392303	-41.772301	4.2	15	164	76	37	8
2016p871629	18/11/2016	173.610703	-42.004101	4.2	9	159	74	-47	5
2016p871791	18/11/2016	173.459595	-42.347599	4.4	8	249	80	-127	5
2016p871992	18/11/2016	174.25	-41.745998	4.4	16	341	87	-5	9
2016p872063	18/11/2016	173.126099	-42.513401	4.4	4	16	56	85	9
2016p873325	19/11/2016	173.851593	-42.306198	4.1	10	88	74	149	3
2016p873821	19/11/2016	174.298706	-41.8288	4.2	13	155	70	46	5
2016p873890	19/11/2016	174.049301	-41.980701	3.9	11	204	56	108	4
2016p876450	20/11/2016	173.534897	-42.620499	4.7	11	208	83	24	10
2016p878954	21/11/2016	174.000793	-41.932999	4.2	13	305	83	-14	6
2016p880389	21/11/2016	173.636703	-42.1861	4.7	9	163	82	-18	9

Continued on next page

Table A.1 continued from previous page

Event ID	Date	Longitude (°)	Latitude (°)	M_w	CD (km)	Strike (°)	Dip (°)	Rake (°)	NS _e
2016p881704	22/11/2016	172.955399	-42.926399	4.3	11	249	83	-167	7
2016p881727	22/11/2016	172.956604	-42.945999	4.4	4	3	67	68	15
2016p881756	22/11/2016	172.951904	-42.891102	4.4	6	20	54	88	17
2016p882181	22/11/2016	172.918701	-42.938	3.8	5	242	52	94	5
2016p882187	22/11/2016	173.010803	-42.953098	4.6	4	354	64	67	27
2016p883896	23/11/2016	174.276398	-41.737499	4.7	19	57	81	167	25
2016p884917	23/11/2016	174.279007	-41.738899	4.2	17	236	89	-168	6
2016p886502	24/11/2016	174.029404	-41.966499	4.2	12	163	82	-15	8
2016p890609	25/11/2016	173.276398	-42.483601	3.9	7	53	60	118	4
2016p895574	27/11/2016	174.236603	-41.726299	4.8	14	320	85	-7	24
2016p897263	27/11/2016	173.483307	-42.361301	4.4	10	2	78	34	5
2016p898701	28/11/2016	173.752197	-42.087601	4	6	250	85	-165	5
2016p898762	28/11/2016	173.768799	-42.0784	4.2	8	257	82	-159	6
2016p903817	30/11/2016	174.072906	-41.803501	3.9	20	341	79	-12	6
2016p906876	01/12/2016	174.388702	-41.734901	3.9	17	333	88	5	4
2016p907628	01/12/2016	174.268204	-41.694199	3.9	16	235	76	-164	4
2016p916295	05/12/2016	172.807007	-42.704201	3.9	5	152	80	-10	5
2016p921247	06/12/2016	174.229599	-41.7607	4.4	11	355	58	64	10
2016p922917	07/12/2016	173.462296	-42.3578	4.4	14	243	78	-155	5
2016p935725	12/12/2016	174.161606	-41.8088	4.4	19	155	88	13	4
2016p959735	21/12/2016	173.715195	-42.382301	4.3	14	28	56	65	4
2016p962803	22/12/2016	174.120102	-41.772598	4.2	13	325	48	65	4
2016p965164	23/12/2016	174.278107	-41.728901	4.3	14	5	58	68	8
2016p969664	24/12/2016	174.246002	-41.674099	4.5	20	227	81	171	17
2016p976987	27/12/2016	173.878494	-42.4716	4.5	11	233	55	106	6
2016p977108	27/12/2016	173.554703	-42.386101	4.2	10	69	71	147	5
2017p003805	02/01/2017	173.532104	-42.340698	4.1	11	30	68	53	5
2017p014499	06/01/2017	174.275299	-41.6385	4.4	14	62	90	-174	15

Continued on next page

Table A.1 continued from previous page

Event ID	Date	Longitude (°)	Latitude (°)	M_w	CD (km)	Strike (°)	Dip (°)	Rake (°)	NS _e
2017p016396	07/01/2017	173.270096	-42.571499	4.4	11	220	51	125	5
2017p027063	11/01/2017	174.250198	-41.692402	4.6	19	61	86	171	30
2017p029455	11/01/2017	171.684204	-42.785599	4.1	6	76	79	-154	4
2017p084950	01/02/2017	173.764297	-42.311501	4.8	19	240	75	-161	8
2017p095843	05/02/2017	172.748596	-42.7192	4	11	340	84	15	4
2017p100431	07/02/2017	172.759796	-42.705799	4.1	8	219	66	138	5
2017p124453	16/02/2017	172.0569	-42.703999	4	9	73	87	-176	4
2017p135277	20/02/2017	172.829407	-42.756802	4.5	11	72	88	-171	13
2017p144774	23/02/2017	171.695297	-43.1306	4.7	8	163	86	-4	23
2017p158022	28/02/2017	173.876297	-42.4216	4	8	81	84	152	3
2017p159158	28/02/2017	173.1008	-42.969002	4.5	6	23	50	80	29
2017p161294	01/03/2017	173.088898	-42.955101	4.5	6	228	53	94	26
2017p161601	01/03/2017	173.094894	-42.960098	4.8	6	224	50	108	50
2017p168407	04/03/2017	174.118607	-41.830002	4.3	11	355	57	57	4
2017p182004	09/03/2017	173.102402	-42.972099	4	7	34	61	86	4
2017p250334	03/04/2017	173.704895	-42.1777	4.3	6	77	70	155	6
2017p260291	07/04/2017	173.867203	-41.9823	4.4	12	321	78	35	6
2017p266099	09/04/2017	175.289505	-41.617199	4.3	19	8	78	20	18
2017p303640	23/04/2017	173.488098	-42.5051	3.7	16	57	78	142	4
2017p311750	26/04/2017	174.224899	-41.710602	3.7	14	320	79	20	3
2017p371954	18/05/2017	171.057297	-43.023701	4.1	4	345	79	32	5
2017p381325	22/05/2017	173.777206	-42.2924	4.3	8	35	82	158	5
2017p433631	10/06/2017	172.419403	-43.555199	3.8	7	161	89	5	17
2017p449317	16/06/2017	172.441299	-42.758598	4.1	8	340	82	-24	7
2017p512943	09/07/2017	175.098495	-41.165401	3.9	7	336	63	31	27
2017p515062	10/07/2017	174.028503	-41.926601	3.8	14	1	55	49	3
2017p517915	11/07/2017	174.175995	-41.691101	4.1	18	321	84	17	3
2017p666283	04/09/2017	173.469406	-42.456001	4.1	11	354	69	49	4

Continued on next page

Table A.1 continued from previous page

Event ID	Date	Longitude (°)	Latitude (°)	M_w	CD (km)	Strike (°)	Dip (°)	Rake (°)	NS _e
2017p675772	08/09/2017	172.861099	-42.630699	4.2	13	240	61	127	5
2017p723159	25/09/2017	178.3647	-38.235401	4.3	18	10	80	105	3
2017p795065	22/10/2017	173.458893	-42.358101	5	11	347	76	33	20
2017p819775	31/10/2017	177.364899	-37.4081	4.9	8	263	58	-76	3
2017p821508	31/10/2017	177.347702	-37.4132	4.9	5	241	65	-78	3
2017p847270	10/11/2017	172.839203	-42.693001	3.9	14	225	56	118	6
2017p860319	15/11/2017	176.383194	-40.765598	4.1	12	27	48	79	5
2017p865076	17/11/2017	172.407303	-43.593399	3.8	9	238	88	-177	16
2017p952681	19/12/2017	173.645203	-42.4669	4.5	5	27	65	79	6
2018p012973	05/01/2018	173.991699	-41.8759	4.2	19	198	68	69	5
2018p049948	19/01/2018	172.620895	-43.582199	3.7	5	137	80	13	9
2018p109067	10/02/2018	170.490997	-43.310299	4.4	7	327	80	-26	4
2018p124237	15/02/2018	171.7164	-42.773102	4	5	348	85	-10	3
2018p177486	07/03/2018	173.441696	-42.356899	4.6	17	64	79	140	11
2018p248771	03/04/2018	170.789993	-43.279499	4.3	5	346	74	19	5
2018p248784	03/04/2018	170.777405	-43.2742	4.5	4	345	85	31	9
2018p249209	03/04/2018	173.826202	-42.2924	4.2	19	43	60	80	4
2018p328394	02/05/2018	174.064499	-41.876301	4.2	11	151	64	-98	3
2018p356381	12/05/2018	174.138702	-41.681499	4.1	20	229	88	173	3
2018p375166	19/05/2018	176.696899	-40.339802	4	14	51	75	120	3
2018p424369	07/06/2018	174.111404	-41.856998	4	11	341	55	58	3
2018p460630	20/06/2018	177.662506	-37.723499	4.5	15	326	72	154	5
2018p465460	22/06/2018	176.6241	-40.318401	3.8	14	7	59	115	3
2018p465580	22/06/2018	176.597504	-40.306499	4.7	12	0	70	120	18
2018p510780	08/07/2018	173.302399	-42.513599	3.9	15	227	80	-164	4
2018p528060	15/07/2018	172.798294	-43.480598	3.7	5	44	81	160	18
2018p595488	09/08/2018	172.733398	-42.728001	4	11	344	67	40	6
2018p752434	06/10/2018	167.830307	-44.4352	4.7	12	180	61	58	4

Continued on next page

Table A.1 continued from previous page

Event ID	Date	Longitude (°)	Latitude (°)	M_w	CD (km)	Strike (°)	Dip (°)	Rake (°)	NS_e
2018p765813	11/10/2018	173.1604	-42.529202	4	9	56	63	118	4
2018p806140	26/10/2018	174.173096	-41.725498	4.3	20	330	71	38	4
2018p830804	04/11/2018	176.832703	-39.880199	4.3	17	11	78	82	7
2019p005106	02/01/2019	176.648697	-40.998798	4.3	14	194	64	88	3

957 B Electronic Supplement B: Station Information

958 Table B.1 provides details of the 212 ground-motion recording stations with sufficient high-
 959 quality recordings considered including the station code, geographic location, modelled
 960 V_{s30} and number of earthquakes observed NE_s .

961 Figure B.1 indicates the geographic regions of Wellington and Canterbury and shows
 962 the spatial distribution of ground-motion recording stations corresponding to subcate-
 963 gories that are analyzed.

Table B.1: Station geographic location, site characteristics and NE_s of ground-motion recording stations considered.

Site	Longitude (°)	Latitude (°)	V_{s30} (m/s)	H_{250} (m)	H_{1250} (m)	NE_s
ADCS	171.747604	-43.902401	230	-0.46	-0.41	11
AKSS	172.963501	-43.810902	265	-3.01	-7.88	39
AMBC	172.730896	-43.154701	231	0.0	-0.92	20
APPS	171.567703	-42.948898	282	0.71	-1.47	15
ARKS	174.944107	-41.2421	262	0.11	0.96	21
ASHS	172.595901	-43.274399	230	-0.01	-0.86	84
BFZ	176.246201	-40.6796	384	-2.77	-37.59	3
BMTS	174.925995	-41.191399	398	-1.05	-15.13	37
BOWS	174.776306	-41.279202	267	-0.16	-4.46	10
BSWZ	173.875702	-41.714901	599	-2.08	-8.17	20
BWHS	172.682205	-43.4804	199	-4.86	-54.77	6
BWRS	173.905106	-41.439499	608	0.75	-10.65	109
CACS	172.529999	-43.4832	435	-0.19	-4.53	127
CBGS	172.619904	-43.529301	197	-0.2	-0.99	125
CCCC	172.6474	-43.538101	177	0.19	27.44	8
CECS	173.274902	-42.813499	231	0.18	-5.25	61
CHHC	172.627502	-43.5359	206	-0.05	-2.66	11
CMHS	172.624207	-43.565601	205	-0.99	-34.34	138
CMWZ	174.213806	-41.749001	301	-0.19	-3.28	19
COLD	172.1026	-43.600498	253	10.96	23.36	25
CPFS	176.220993	-40.8988	195	-0.25	0.47	10
CRLZ	172.623199	-43.574699	900	3.54	29.04	87
CSHS	171.723602	-43.226501	278	0.31	-0.98	38
CSTC	172.381302	-43.312302	284	-0.04	-1.12	26
CUBS	174.774399	-41.295502	289	8.41	58.41	5
CULC	172.802597	-42.759399	232	-0.69	-3.57	18
D09C	172.632599	-43.532299	181	0.35	-9.54	18
D14C	172.624695	-43.6325	733	3.87	14.66	55
DALS	172.673203	-43.512001	188	0.3	-3.91	11
DAVS	174.954407	-41.205799	251	-0.15	-9.78	4
DCZ	167.153503	-45.464699	473	2.34	-8.25	3
DFHS	172.102203	-43.4897	518	-4.83	-29.58	82
DHSS	172.727203	-43.630299	366	-0.04	-1.74	28
DSLC	172.197906	-43.6675	230	1.24	2.08	81

Continued on next page

Table B.1 continued from previous page

Site	Longitude (°)	Latitude (°)	V _{s30} (m/s)	H ₂₅₀ (m)	H ₁₂₅₀ (m)	NE _s
DSZ	171.804596	-41.744999	368	0.39	-0.64	5
EBPS	174.900208	-41.289398	349	-6.0	-46.57	8
EKTS	175.708801	-40.649502	228	0.18	-0.72	6
EYRS	172.355392	-43.421398	231	0.34	0.72	46
FAIS	174.940094	-41.207401	380	-4.99	-53.23	33
FKPS	174.778793	-41.287899	400	0.14	0.95	26
FXBS	175.225998	-40.461399	306	-0.29	0.44	6
GKBS	178.031906	-38.682201	396	0.19	-0.02	3
GLWS	172.511002	-42.5942	293	-0.0	0.04	21
GODS	172.769302	-43.5784	586	-0.36	-0.57	63
GOVS	172.635696	-43.652401	479	27.44	138.02	19
GVZ	173.034805	-42.9674	484	-0.15	-0.02	41
GWTS	177.9216	-38.625702	229	-0.04	-6.32	3
HAFS	170.556107	-43.148899	269	0.02	0.44	5
HALS	172.569504	-43.5909	183	1.45	3.69	35
HAVS	173.784698	-41.272301	599	0.48	-9.98	21
HDWS	169.044098	-43.882999	230	-1.59	3.66	3
HHSS	172.592804	-43.557499	179	0.27	-0.22	48
HNPS	176.880096	-39.671001	265	-0.3	-9.2	4
HOCS	175.279404	-40.621601	231	-4.54	-19.78	3
HPSC	172.702194	-43.501598	207	-6.19	-16.64	8
HSES	172.830505	-42.523201	232	0.47	0.68	77
HUNS	172.657196	-43.579399	614	0.57	-5.29	29
HWHS	174.2742	-39.585098	212	-1.29	-45.17	4
INGS	171.952499	-41.857101	292	-0.23	-1.39	4
INHS	174.190506	-39.1562	303	0.76	1.09	4
INZ	171.444107	-42.724499	270	0.38	0.35	7
KAFS	176.709305	-38.0835	225	0.08	0.49	4
KEKS	173.9814	-41.9557	494	0.32	-1.09	127
KHZ	173.539001	-42.416	296	-0.42	-14.71	17
KIKS	173.682098	-42.4258	600	0.27	0.86	63
KILS	172.640594	-43.526901	192	-0.02	-0.12	7
KIRS	175.229996	-41.0769	287	0.22	1.19	5
KOKS	171.135605	-42.891701	235	25.1	66.25	4
KOWC	171.854797	-43.321499	244	0.21	0.78	14
KPOC	172.663803	-43.376499	257	0.17	-15.38	26
KVSD	172.277695	-43.5854	231	-0.02	-0.13	20
LHBS	174.892303	-41.196602	504	0.06	-4.95	12
LHES	174.903305	-41.2117	249	0.61	-4.63	21
LHRS	174.893204	-41.2047	498	6.17	39.27	8
LHUS	174.8936	-41.230801	195	0.02	-1.36	9
LINC	172.468002	-43.623199	292	-0.04	0.53	5
LNBS	174.926605	-41.205002	309	-0.34	-1.18	10
LPCC	172.724792	-43.6078	792	-4.78	-43.6	3
LPLS	169.423096	-43.714699	195	-0.1	-0.49	4

Continued on next page

Table B.1 continued from previous page

Site	Longitude (°)	Latitude (°)	V _{s30} (m/s)	H ₂₅₀ (m)	H ₁₂₅₀ (m)	NE _s
LRSS	174.904205	-41.229401	251	-0.27	-2.09	8
LSRC	172.543304	-42.869499	368	0.03	0.1	8
LTZ	172.270996	-42.7817	370	-0.2	-4.39	35
MAVS	175.461502	-41.210899	231	0.07	1.33	10
MAYC	171.421707	-43.823101	231	-0.05	0.35	16
MCAS	172.328003	-41.7999	230	-2.02	2.6	9
MCNS	170.097198	-43.736401	272	0.0	-0.03	3
MECS	169.232895	-44.2304	271	0.54	1.43	6
MENS	172.711502	-43.558498	500	-0.8	-1.39	23
MGCS	173.944397	-41.507702	303	0.01	-1.02	48
MISS	174.818405	-41.314899	203	-0.32	-0.39	49
MKBS	174.698105	-41.225899	348	5.8	12.48	59
MKVS	174.705505	-41.2654	269	-0.15	0.27	8
MNZS	172.973801	-43.637402	600	0.08	0.91	23
MOLS	173.257401	-42.088001	282	0.0	0.26	73
MORS	172.621399	-43.539501	179	-0.01	-0.27	27
MPSS	172.642303	-43.499401	180	1.04	8.57	31
MQZ	172.653793	-43.7061	473	2.8	7.26	103
MRZ	175.578506	-40.6605	272	-0.12	-4.14	9
MSZ	167.926407	-44.673302	500	0.7	11.08	4
MTHS	171.666397	-43.563202	284	-0.02	0.01	34
MTPS	172.725601	-43.584702	830	8.76	29.61	22
MWFS	176.6689	-37.8591	494	-0.81	-4.07	4
MWZ	177.527802	-38.334	457	-0.18	1.44	4
MXZ	178.306595	-37.562302	597	-0.79	-12.2	6
NBLC	172.7314	-43.506901	190	-0.52	-6.67	9
NBSS	174.953796	-41.202301	200	-1.0	-8.21	26
NCDS	176.876099	-39.498402	163	9.15	30.66	4
NCHS	176.896805	-39.506599	179	1.15	-0.15	5
NELS	173.2742	-41.2878	360	0.64	58.27	4
NEWS	174.821793	-41.231998	493	2.98	3.54	44
NGHS	176.914902	-39.485901	272	0.49	-0.01	4
NLMS	173.276794	-41.266499	276	7.02	60.17	4
NNBS	172.718002	-43.495399	212	0.16	0.1	121
NNZ	173.379501	-41.217098	370	0.05	0.43	15
NPCS	174.073395	-39.062401	299	0.01	-0.05	4
NSBS	168.660904	-43.996201	235	0.28	-2.89	6
NSPS	176.915894	-39.489601	256	0.39	1.81	3
NWFS	175.233994	-41.5891	272	5.72	74.55	13
OHSS	172.660507	-43.444599	196	-6.0	-29.75	23
OPCS	177.2892	-38.014099	229	-0.06	-0.3	4
OPWS	172.664307	-43.556198	179	-0.0	-0.12	15
OTKS	175.143799	-40.754902	239	-0.0	-0.07	3
OXZ	172.0383	-43.325901	429	7.37	84.87	106
PAPS	175.005005	-40.914299	309	-0.28	-0.5	8

Continued on next page

Table B.1 continued from previous page

Site	Longitude (°)	Latitude (°)	V _{s30} (m/s)	H ₂₅₀ (m)	H ₁₂₅₀ (m)	NE _s
PARS	172.750702	-43.567902	606	-15.01	-29.7	66
PFAS	174.8461	-41.1385	314	0.37	-0.03	5
PGFS	176.611801	-40.3022	235	-10.42	-22.18	14
PGMS	174.879395	-41.224499	210	1.41	-2.14	26
PHHS	174.904297	-41.252102	600	-1.75	-6.48	21
PNBS	175.607605	-40.3489	230	0.03	0.44	7
PNMS	175.593094	-40.3629	229	-4.4	-37.0	3
PNRS	175.633698	-40.330299	231	-1.28	-5.55	4
POKS	174.831497	-41.124901	274	0.04	-1.36	5
POLS	174.839096	-41.131401	233	-0.18	-0.71	8
POTS	174.774597	-41.272202	422	0.52	1.59	24
PPHS	172.606903	-43.492802	187	0.33	0.17	149
PRPC	172.6828	-43.525799	196	5.27	-23.13	19
PTOS	174.860306	-41.223	293	0.08	0.22	28
PUZ	178.257202	-38.071499	348	0.43	1.3	7
PVCS	174.873901	-41.224701	208	-0.03	-0.63	16
PWES	174.825897	-41.127499	494	0.23	0.31	38
PXZ	176.862106	-40.030602	384	-0.25	-16.58	3
QCCS	174.023102	-41.279598	265	-1.45	-17.13	26
QTPS	168.662903	-45.0322	275	-0.04	-0.08	3
RCS1	173.629303	-41.5397	278	0.17	1.65	33
RCS2	174.076401	-41.672199	289	0.23	0.58	7
RDCS	171.864395	-42.119701	242	-0.82	-36.18	5
REHS	172.635101	-43.5219	154	0.27	6.18	137
RHSC	172.564407	-43.536201	286	0.4	-12.85	7
RPZ	171.053894	-43.7146	272	5.12	41.38	7
RQGS	174.781204	-41.296501	278	4.83	-18.21	7
SACS	172.616196	-43.506699	185	0.36	-0.29	15
SCAC	172.9216	-42.938599	280	0.35	1.15	9
SEAS	174.837601	-41.326401	195	-0.57	-2.41	5
SEDS	174.076401	-41.672298	289	0.96	2.18	59
SEVS	174.902206	-41.247002	195	-0.22	0.19	13
SHFC	172.025803	-43.391201	231	4.0	6.83	20
SHLC	172.663406	-43.505299	210	-0.39	-27.3	16
SJFS	172.180298	-42.334599	275	-9.46	-31.64	18
SLRC	172.317505	-43.675098	327	-0.23	-6.15	12
SMHS	172.336304	-43.262199	231	1.06	9.4	32
SNZO	174.704193	-41.308701	494	14.27	-1.76	3
SOCS	174.915894	-41.2043	267	-22.57	-49.23	12
SOMS	174.865005	-41.2575	349	-0.01	-8.3	37
SPFS	171.928894	-43.338001	231	0.14	-1.17	39
SPRS	171.930099	-43.3368	233	-2.28	-4.13	32
STAS	172.641098	-43.513599	179	-0.0	0.01	19
STKS	172.644897	-43.606499	444	-16.52	-72.4	44
SUMS	172.756805	-43.569199	465	-9.15	-52.91	35

Continued on next page

Table B.1 continued from previous page

Site	Longitude (°)	Latitude (°)	V _{s30} (m/s)	H ₂₅₀ (m)	H ₁₂₅₀ (m)	NE _s
SWNC	172.495407	-43.3694	546	-1.7	-16.73	38
TAFS	167.719101	-45.416698	232	0.04	-0.09	3
TBAS	178.300797	-38.372799	206	-0.51	-8.24	4
TDHS	178.365402	-37.633301	195	1.43	-64.44	4
TEPS	174.781097	-41.2906	195	-0.31	-8.08	50
TFSS	174.783096	-41.275398	298	4.76	24.73	30
THZ	172.905197	-41.762501	329	5.81	-23.5	28
TLED	172.201294	-43.595798	231	-0.5	-4.03	17
TOKS	172.780807	-43.822399	597	0.24	0.9	9
TOTS	175.085403	-41.1049	257	-16.56	-70.96	6
TPLC	172.472	-43.549999	398	0.02	-0.04	25
TRMS	175.990997	-40.671299	494	-1.52	56.11	11
RTS	174.773895	-41.298698	278	-11.69	-56.93	18
TSZ	175.961105	-40.058601	428	22.45	56.83	8
UHCS	175.040894	-41.126801	232	11.19	79.12	11
UHSS	175.065094	-41.1264	254	5.87	72.77	3
URZ	177.110901	-38.259201	278	0.94	1.9	5
VUWS	174.778397	-41.2799	312	-2.49	-3.12	20
WAKC	172.7052	-42.9631	240	-0.01	-0.33	88
WANS	174.931	-41.231201	377	6.49	23.03	25
WBCS	171.599792	-41.755699	229	-1.88	-11.16	4
WBFS	176.311096	-40.400902	360	-6.41	-13.68	6
WCSS	171.863495	-43.457699	241	-0.04	0.53	14
WDAS	174.948502	-41.257401	123	0.2	-8.69	20
WDFS	174.138397	-41.8274	281	-1.55	-10.12	125
WDPS	175.869797	-40.3382	231	-0.02	-7.22	12
WEL	174.768204	-41.284	513	-0.02	-0.83	32
WEMS	174.779297	-41.2743	257	-0.3	-0.12	52
WFSS	177.424896	-39.034199	195	0.14	-0.52	3
WHAS	170.326797	-43.316002	272	-17.6	-40.43	5
WHFS	170.358994	-43.2612	260	0.15	0.96	6
WIGC	172.800293	-42.701199	232	1.13	-28.41	3
WKHS	176.985504	-37.961498	215	5.56	7.86	7
WNAS	174.809006	-41.326401	230	0.83	-33.57	30
WNHS	174.775497	-41.3008	277	0.0	-0.1	20
WNKS	174.742096	-41.284801	271	-0.33	-8.62	29
WPWS	176.584305	-39.943901	326	-0.06	-5.47	11
WRCS	175.647797	-40.950401	231	-9.38	-28.39	8
WSTS	174.7845	-41.278099	195	0.24	-63.18	3
WTMC	173.053604	-42.619499	267	0.17	-3.69	9
WVAS	170.737198	-43.071602	374	-4.44	-37.5	13
WVFS	173.350906	-41.620201	231	0.42	0.09	6
WVZ	170.736801	-43.074402	370	-0.03	-10.65	13

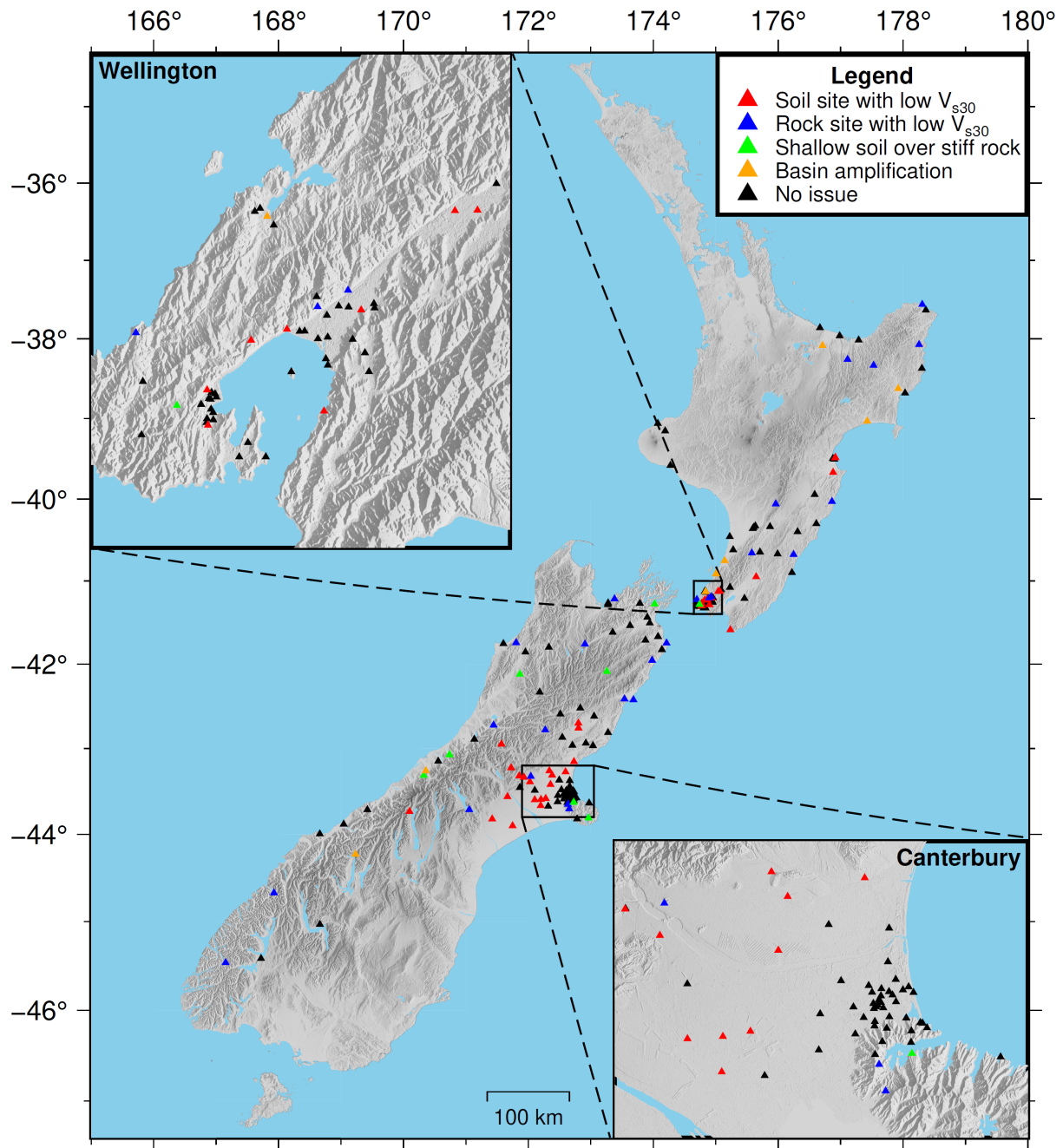


Figure B.1: Spatial distribution of ground-motion recording stations across NZ colored based on their subcategory. Insets show the regions of Wellington and Canterbury where the density of stations are higher.

964 C Electronic Supplement C: Ground-Motion Simulation Method and Computational Considerations

966 The LF simulation component uses a comprehensive representation of source and wave
 967 propagation physics by solving the 3D viscoelastic wave equation using a staggered-grid
 968 finite difference scheme with fourth-order spatial and second-order temporal accuracies.
 969 For the small magnitude earthquake events considered, the earthquake source is modelled
 970 as a double-couple point source with location, magnitude and focal mechanism obtained

971 from centroid moment tensor solutions. The point source models each comprise a single
 972 subfault, in the standard rupture format. The slip for the subfault is determined from the
 973 centroid moment tensor magnitude and a magnitude-area scaling relationship. Leonard
 974 (2010) is used here for active shallow crustal earthquakes. A constant rise time of 0.5 s
 975 is used. Anelastic attenuation is incorporated with quality factors given by the relations
 976 $Q_s = 50V_s$ and $Q_p = 2Q_s$, where V_s is in units of km/s.

977 The HF simulation component is computed using a simplified physics-based simulation
 978 which considers a stochastic source radiation pattern and simplified wave propagation
 979 through a 1D layered velocity model. Attenuation is incorporated using a travel-time
 980 weighted average of the quality factors for each of the 1D velocity model layers and a
 981 HF attenuation factor of $\kappa_0 = 0.045$ to account for the attenuation due to site effects.
 982 A constant Brune stress parameter of $\Delta\sigma = 5$ MPa was also used. These are typical
 983 values for active shallow crustal regions (Graves and Pitarka, 2010). A spatially-averaged
 984 radiation pattern coefficient of 0.55 is used.

985 Table C.1 provides the details of the differences between Standard and Modified sim-
 986 ulation methods used in this study.

Table C.1: Ground-motion simulation method differences between the Standard and Modified simulations.

Simulation Item	Standard Simulation	Modified Simulation
HF Path Duration Model	GP10	BT14
LF Empirical Site Amplification	CB14 with log-linear taper to unity from 2-5 s	None
HF Empirical Site Amplification	CB14 with log-linear taper to unity from 2-5 s	CB14 with log-linear taper to unity from 1-2 s
LF 3D Velocity Model	NZVM v1.66	NZVM v2.02

987 Event-specific finite difference computational domains are an optimization adopted due
 988 to the progression from regional (e.g., Canterbury) ground-motion simulation validation
 989 efforts to a nationwide effort, to balance the tradeoff between computational expense and
 990 number of records included in the validation. To estimate an initial simulation domain
 991 that is appropriate for a given earthquake (smaller domains for smaller M_w earthquakes
 992 and larger domains for larger M_w earthquakes), the extents were obtained by calculating
 993 the R_{rup} at which a specified peak ground velocity (PGV) would occur based on a given
 994 empirical GMM, for which the NZ-specific active shallow crustal model of Bradley (2013)
 995 was adopted. The lateral (X and Y) extents of the domains were taken to be twice the
 996 calculated R_{rup} and the domain was centered on the source epicentre. However, it was
 997 found that a constant PGV threshold did not scale well across the M_w considered, giving
 998 simulation domains that were too small at smaller M_w (and thus excessively excluded
 999 recorded ground motions of use). Therefore, a variable PGV threshold was developed as a
 1000 function of M_w . Figure C.1a presents the adopted function of PGV threshold for this study
 1001 and Figure C.1b the corresponding lateral extents. The simulation domains were further
 1002 optimized by rotating the square domain to be parallel to the country's 'centreline' and
 1003 then resizing the lateral extents by trimming most of the offshore area, ultimately resulting
 1004 in a rotated rectangular domain. The depth (Z) extents of the simulation domains were
 1005 also optimized as a function of the M_w and centroid depth of the earthquake source.

1006 The LF simulation domains have a finite difference grid spacing of 0.1 km and a
 1007 minimum shear-wave velocity of $V_{s,min} = 500$ m/s is enforced to achieve a maximum

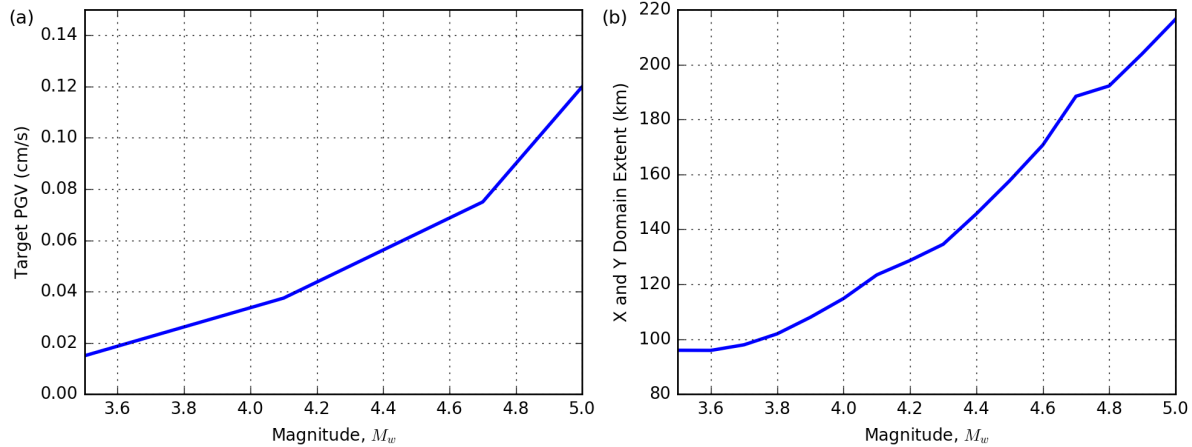


Figure C.1: Simulation computational domain size relationships: (a) M_w -target PGV threshold; (b) M_w -lateral (X and Y) domain extent.

frequency of 1.0 Hz based on 5 points per wavelength for a 4th order spatial finite difference method, which is subsequently the transition frequency where the LF and HF components are merged. A time increment of $\Delta t = 0.005$ s was utilized to ensure numerical stability. The simulation domains adopt a ‘squashed-tapered’ topography to include the effect of crustal velocities above mean sea level (Harmsen et al., 2008).

D Electronic Supplement D: Fourier Amplitude Spectra Validation

Additional analysis of the bias associated with smoothed Fourier amplitude spectra (FAS) was carried out to identify the salient changes to the frequency content in the simulations. Each record’s FAS was smoothed with Konno-Ohmachi matrices with bandwidth parameter $b=20$ before carrying out the mixed-effects regression. Figure D.1 presents the model prediction bias, a , and total standard deviation, σ , of the smoothed FAS. At low frequencies, the Standard simulation (red) is overpredicted, with a negative peak in the bias at around 0.5Hz. This overprediction is due to the overamplification from the empirical V_{s30} -based site amplification. An intermediate result utilizing the Modified simulation method with the old NZVM v1.66 (green) is shown here alongside the Modified simulation method with the new NZVM v2.02 (blue). Comparing the intermediate result to the Standard simulation shows that the removal of empirical site amplification changes the overprediction to underprediction at low frequencies. Comparing the intermediate result to the Modified simulation, the effect of the new NZVM version on the frequency content can be explicitly quantified as the underprediction is slightly reduced across the same period range as basin effects are included at many more sites in the simulations. τ for smoothed FAS is not shown as all prediction methods are practically identical, suggesting there is negligible difference between each simulation methods between-event variability.

Figure D.2 presents ϕ_{S2S} and ϕ_{ss} for smoothed FAS. For ϕ_{S2S} , the simulations are practically equivalent at higher frequencies ($f \geq 1.0$ Hz) but have significant differences at lower frequencies ($f < 1.0$ Hz) as a result of the removal of empirical site amplification and NZVM changes, showing larger values for the Modified simulation. This is likely

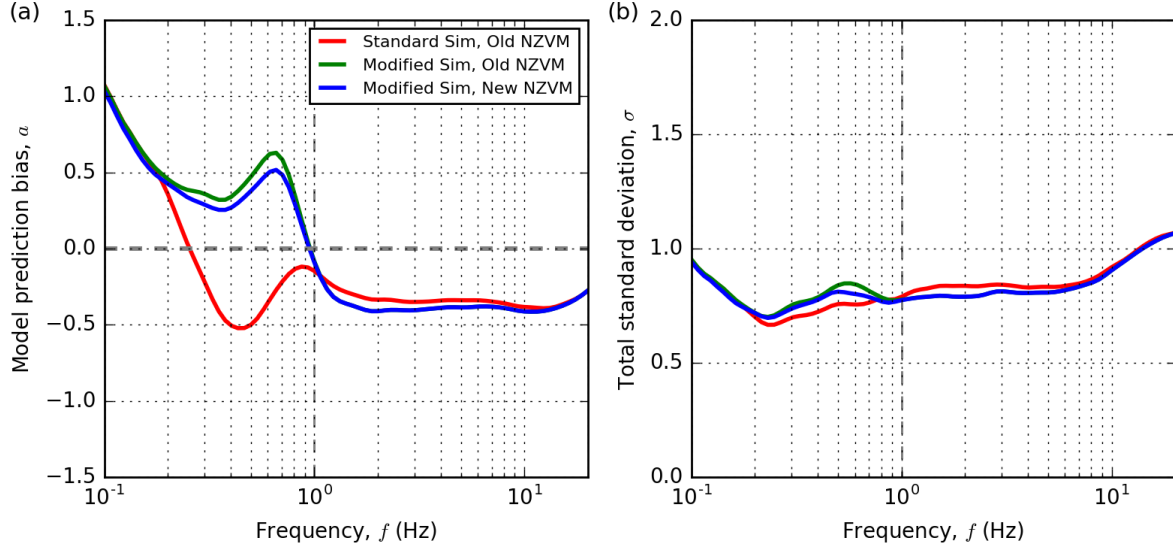


Figure D.1: Simulated prediction of smoothed Fourier amplitude spectra: (a) systematic model prediction bias, a ; and (b) total standard deviations, σ .

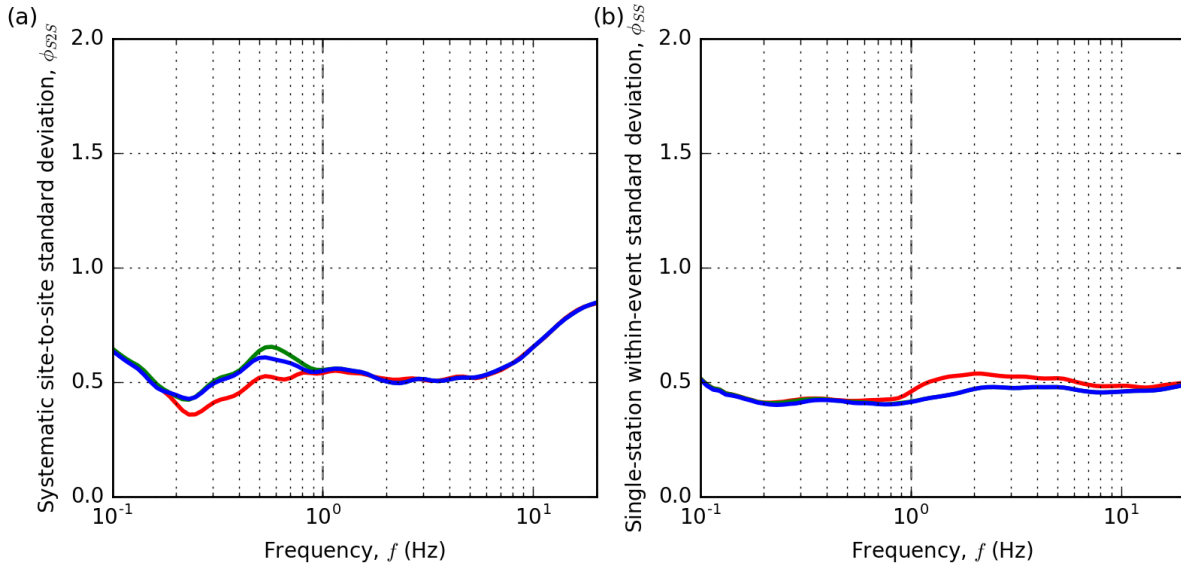


Figure D.2: Within-event standard deviations: (a) systematic site-to-site uncertainty; and (b) single-station within-event variability.

due to the lack V_{s30} correction from output reference velocities and could be improved by lowering the minimum shear-wave velocity in the simulations. For ϕ_{ss} , the lower frequencies are practically equivalent but differences manifest at higher frequencies which indicate the Modified simulation is more precise. This is likely due to the change in HF path duration model causing record-specific changes as it is dependent on R_{rup} .
 1036
 1037
 1038
 1039
 1040

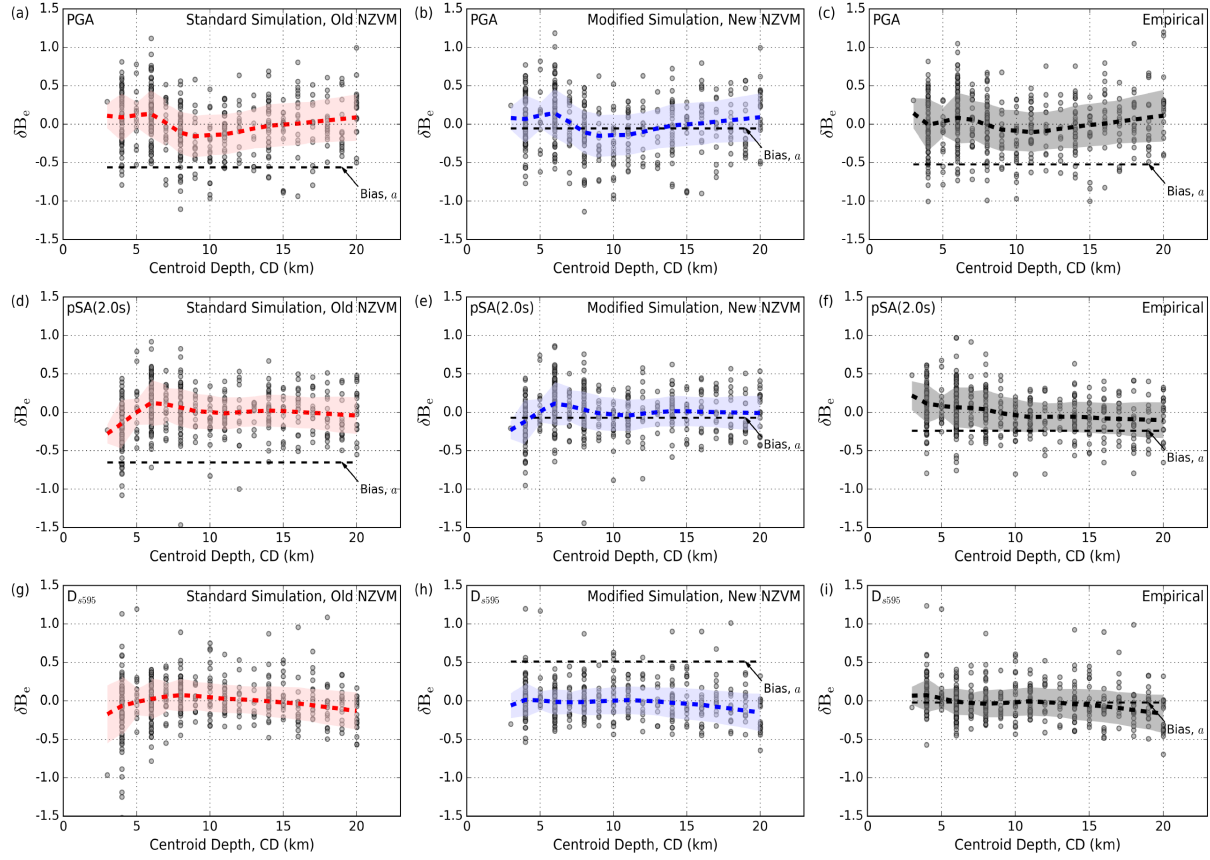


Figure E.1: Comparison of simulated and empirically-predicted between-event residual, δB_e , against centroid depth for PGA, pSA(2.0s) and D_{s595} . The locally weighted scatterplot smoothing regression trend lines are represented as the thick dashed lines with shaded regions corresponding to 16-84th percentile confidence intervals, while the associated model prediction biases, a , are represented as the thin dashed line. For Standard simulation D_{s595} , (g), the model prediction bias is $a = 1.94$ and is therefore outside of the axes shown.

1041 E Electronic Supplement E: Comparison of Residu- 1042 als Against Source, Path and Site parameters

1043 Figures E.1 to E.5 provide sets of plots illustrating the dependence of between-event,
1044 systematic site-to-site, and 'remaining' within-event residuals on source, path and site
1045 parameters, that were omitted from the main text. The significant trends and features
1046 of the dependencies were elaborated upon in the main text and therefore no further
1047 discussion is presented here.

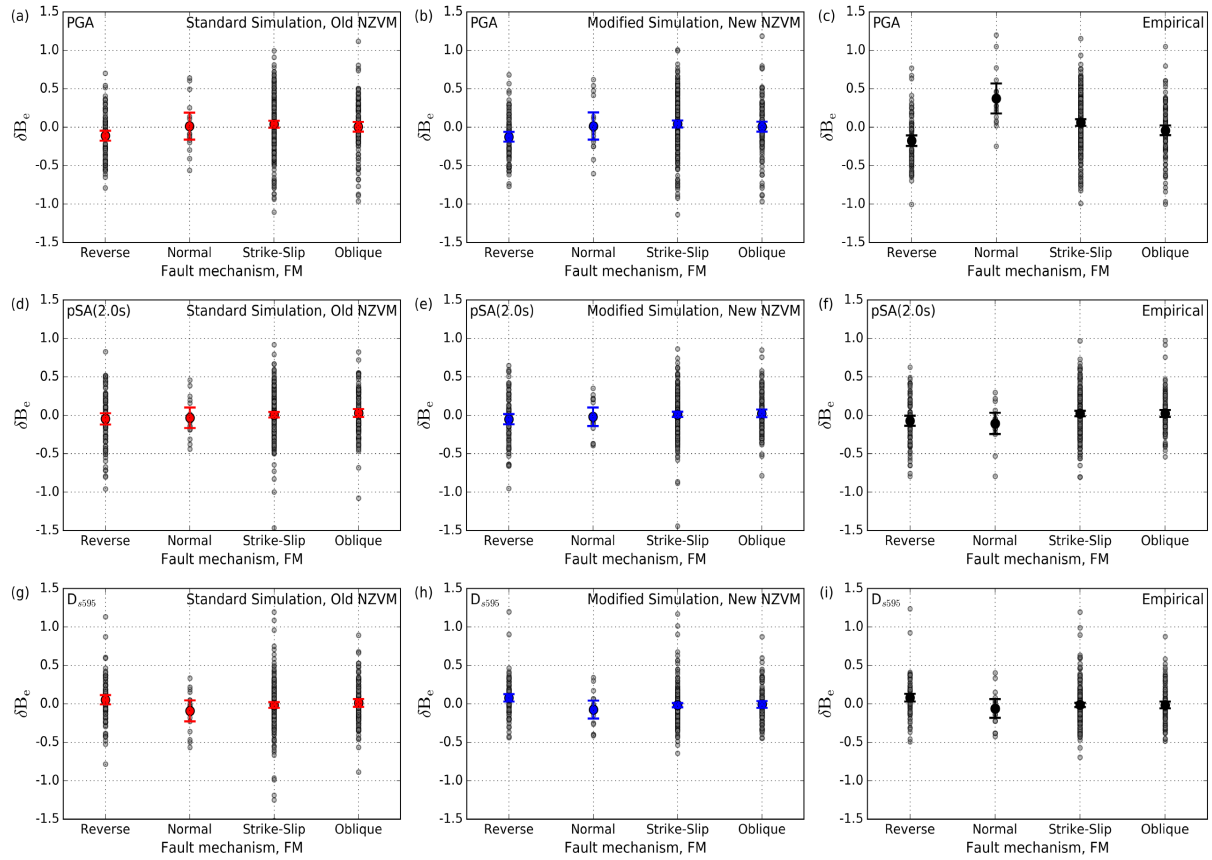


Figure E.2: Comparison of simulated and empirically-predicted between-event residual, δB_e , against focal mechanism for PGA, pSA(2.0s) and D_{s595} . The mean for each focal mechanism is indicated by the circle marker and the error bars correspond to 16-84th percentile confidence intervals.

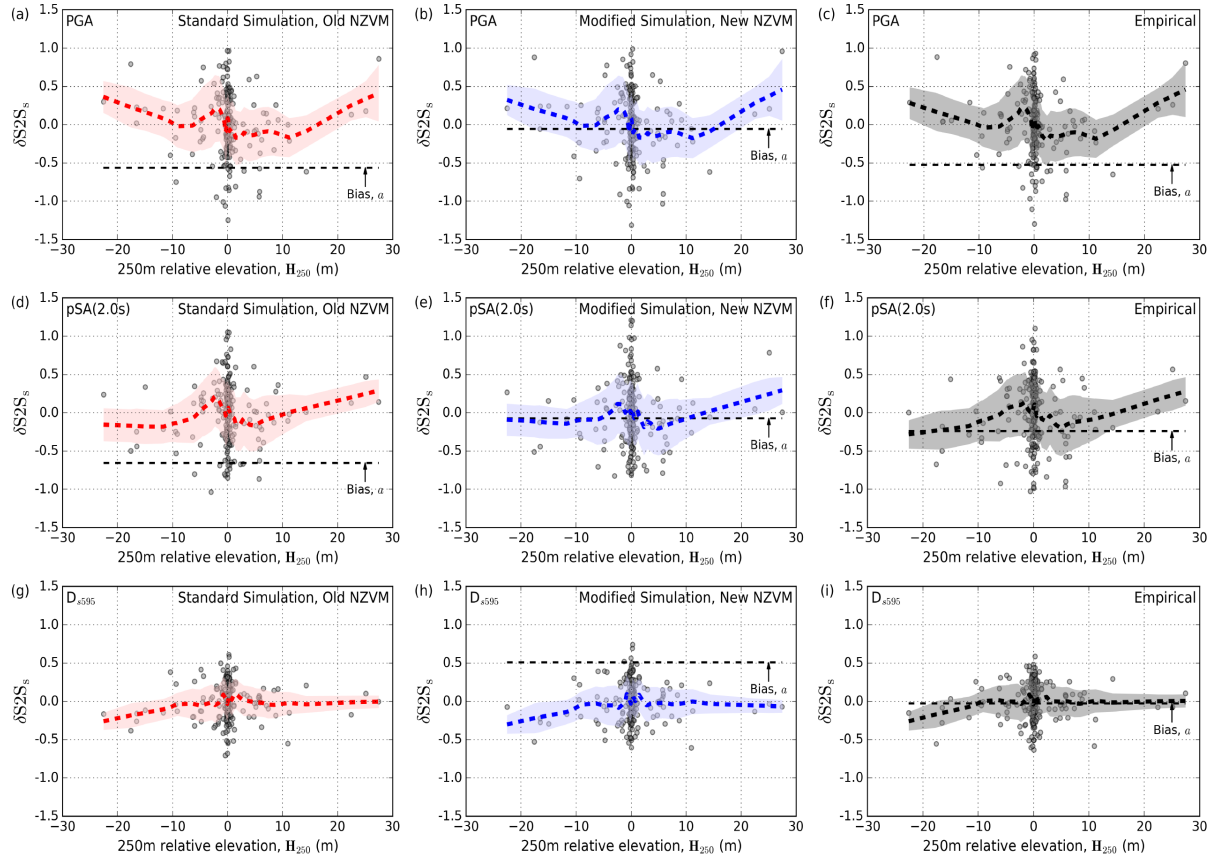


Figure E.3: Comparison of simulated and empirically-predicted systematic site-to-site residual, $\delta S2S_s$, against 250 m relative elevation for PGA, pSA(2.0s) and D_{s595} . The locally weighted scatterplot smoothing regression trend lines are represented as the thick dashed lines with shaded regions corresponding to 16-84th percentile confidence intervals, while the associated model prediction biases, a , are represented as the thin dashed line. For Standard simulation D_{s595} , (g), the model prediction bias is $a = 1.94$ and is therefore outside of the axes shown.

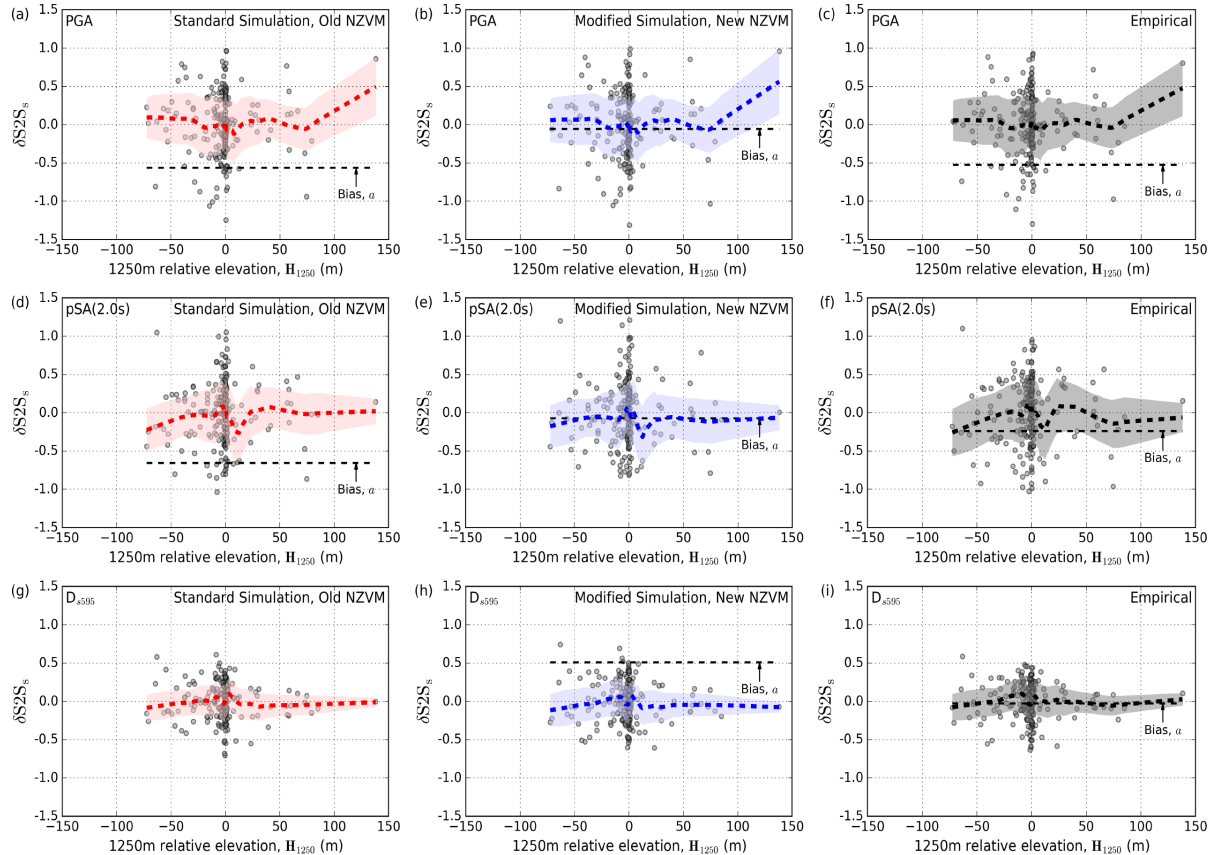


Figure E.4: Comparison of simulated and empirically-predicted systematic site-to-site residual, $\delta S2S_s$, against 1250 m relative elevation for PGA, pSA(2.0s) and D_{s595} . The locally weighted scatterplot smoothing regression trend lines are represented as the thick dashed lines with shaded regions corresponding to 16-84th percentile confidence intervals, while the associated model prediction biases, a , are represented as the thin dashed line. For Standard simulation D_{s595} , (g), the model prediction bias is $a = 1.94$ and is therefore outside of the axes shown.

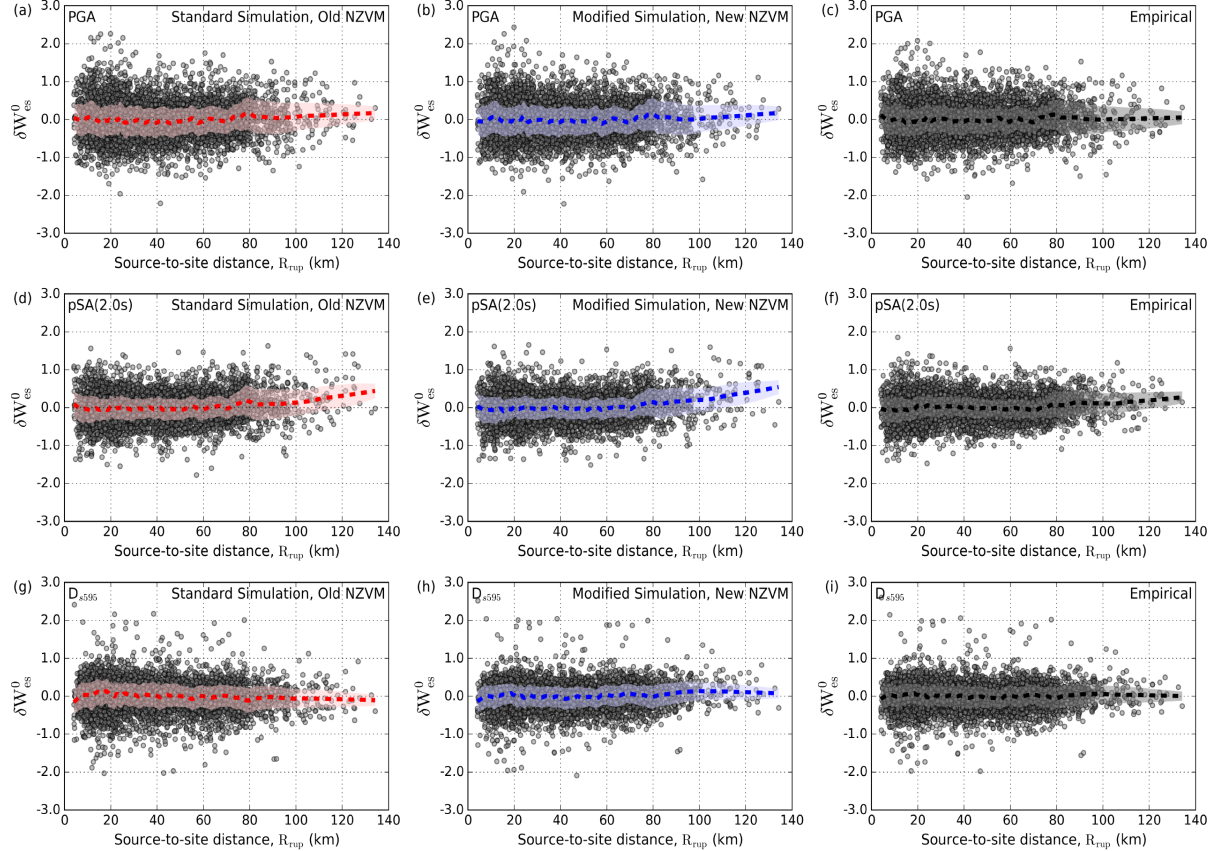


Figure E.5: Comparison of simulated and empirically-predicted ‘remaining’ within-event residual, δW_{es}^0 , against source-to-site distance for PGA, pSA(2.0s) and D_{s595} . The locally weighted scatterplot smoothing regression trend lines are represented as the thick dashed lines with shaded regions corresponding to 16–84th percentile confidence intervals, while the associated model prediction biases, a , are represented as the thin dashed line. For Standard simulation D_{s595} , (g), the model prediction bias is $a = 1.94$ and is therefore outside of the axes shown.

₁₀₄₈ **F Electronic Supplement F: Spatial Maps of δB_e and**
₁₀₄₉ **$\delta S2S_s$**

₁₀₅₀ Figures F.1 to F.6 provide a larger set of plots illustrating the spatial variation in between-
₁₀₅₁ event and systematic site-to-site residuals for simulation and empirical predictions for
₁₀₅₂ PGA, pSA(2.0s) and D_{s595}.

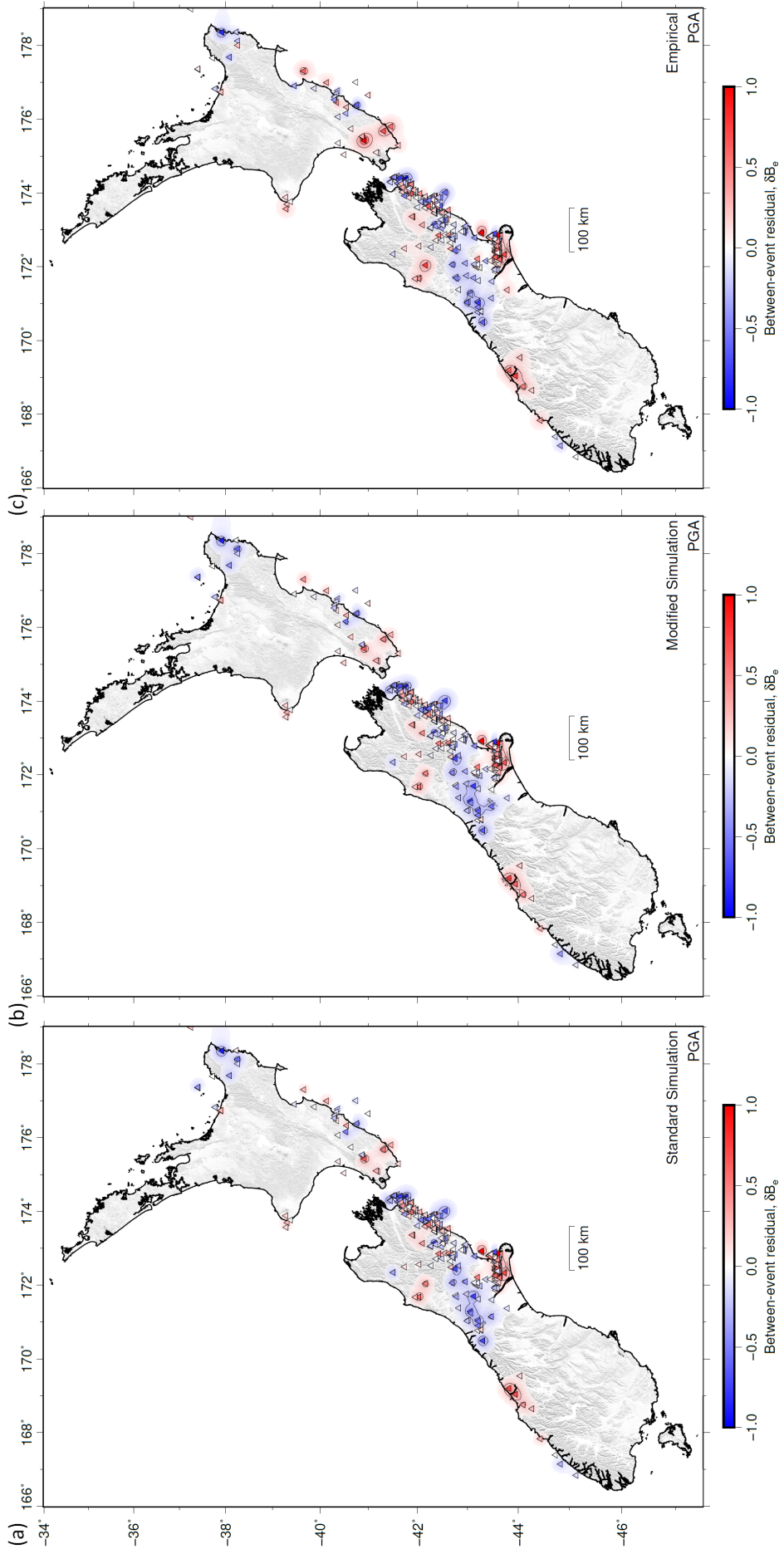


Figure F.1: Spatial distribution of PGA between-event residuals, δB_e , for 479 earthquakes from: (a) Standard simulation; (b) Modified simulation; and (c) empirical prediction.

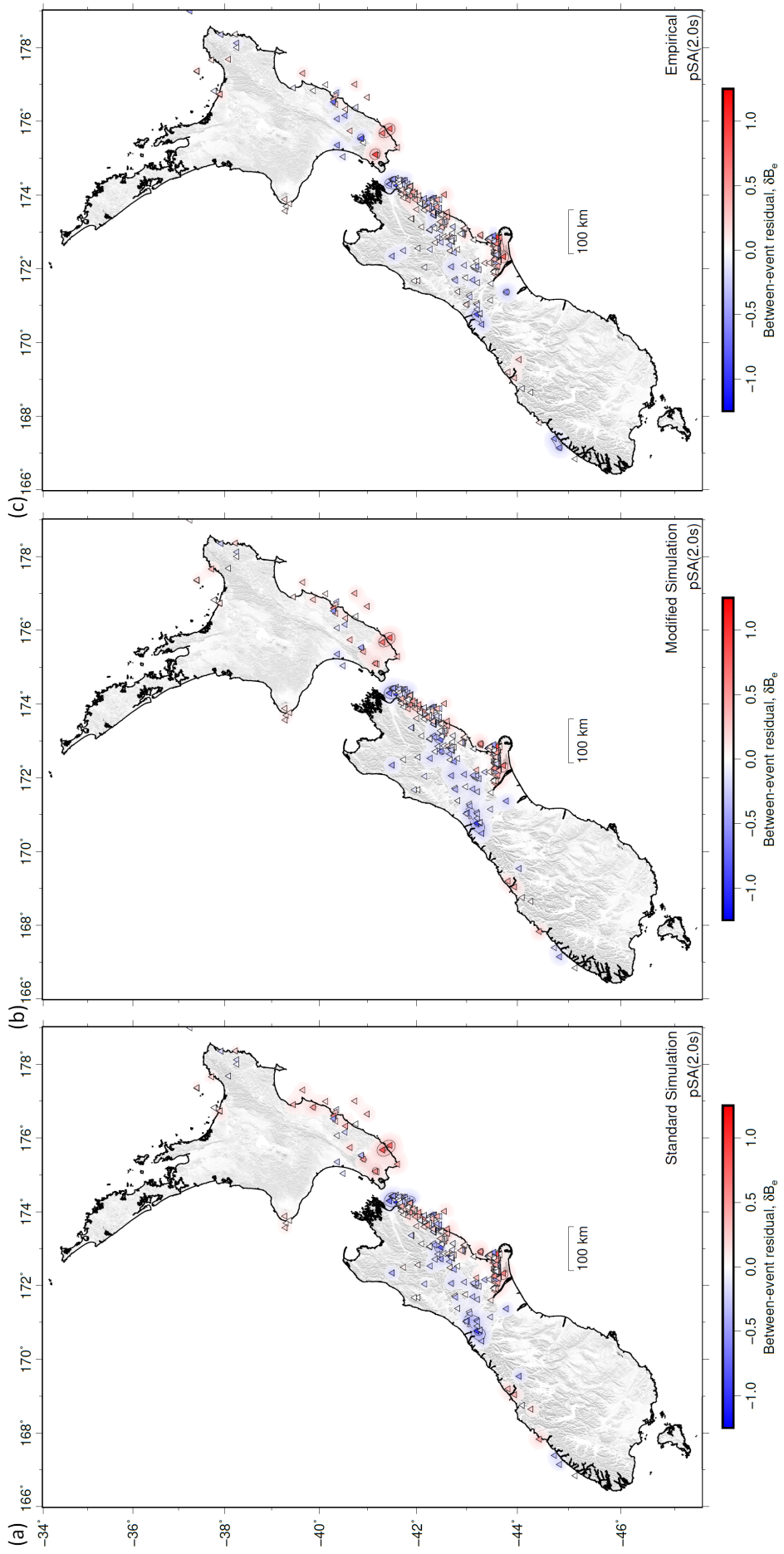


Figure F.2: Spatial distribution of pSA(2.0s) between-event residuals, δB_e , for 479 earthquakes from: (a) Standard simulation; (b) Modified simulation; and (c) empirical prediction.

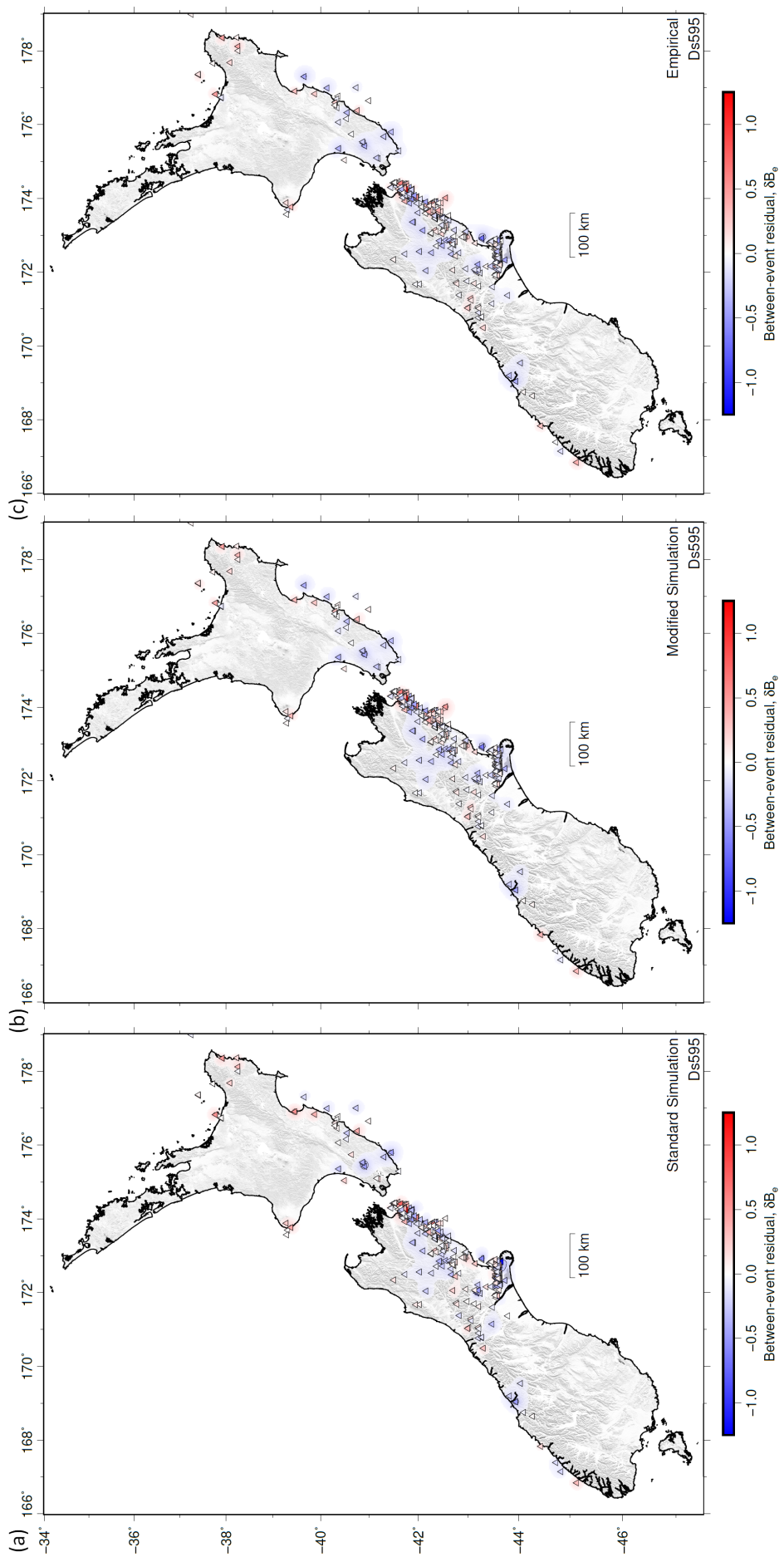


Figure F.3: Spatial distribution of D_{s595} between-event residuals, δB_e , for 479 events from: (a) Standard simulation; (b) Modified simulation; and (c) empirical prediction.

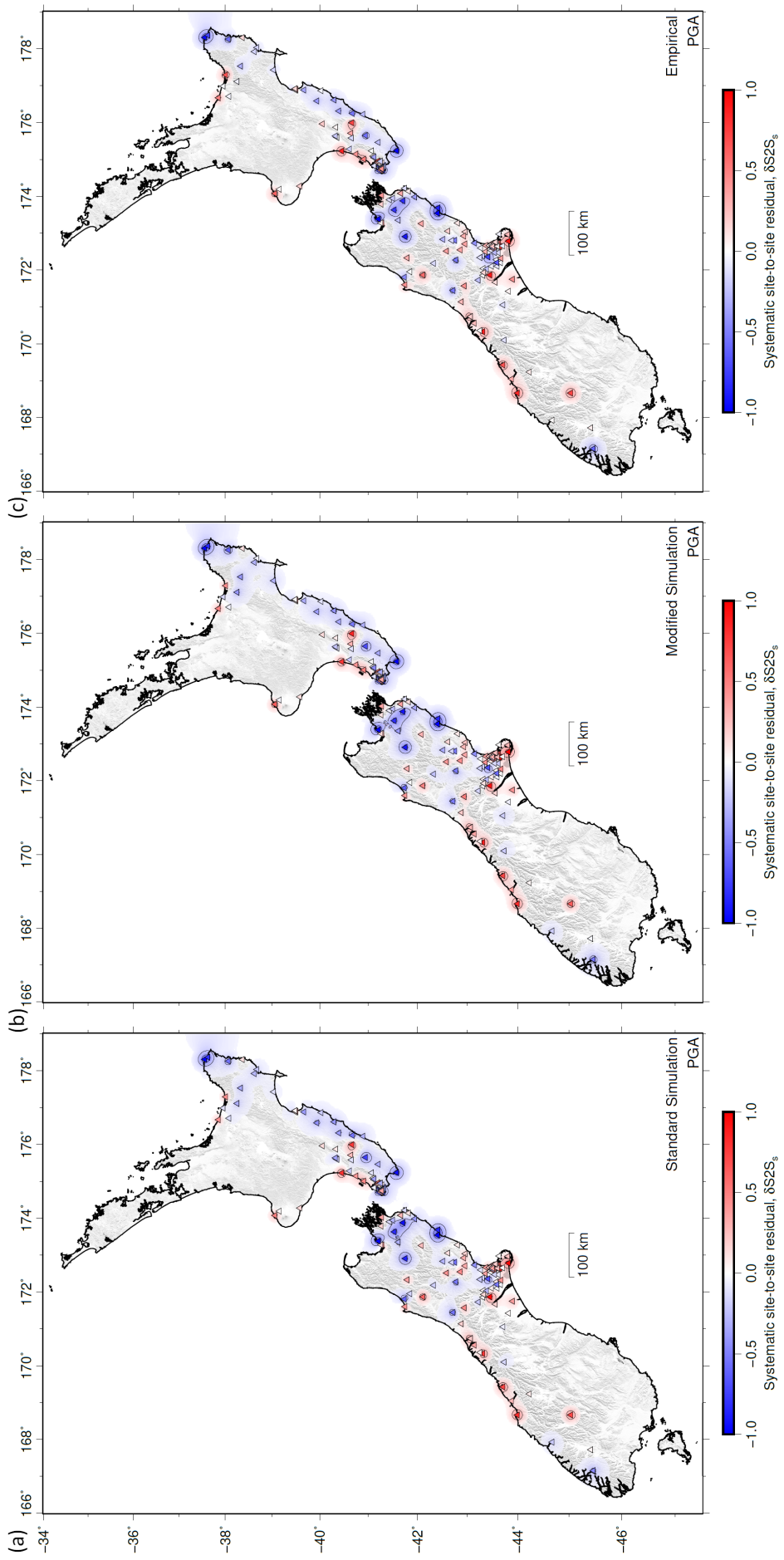


Figure F.4: Spatial distribution of PGA between-event residuals, $\delta S2S_s$, for 212 stations from: (a) Standard simulation; (b) Modified simulation; and (c) empirical prediction.

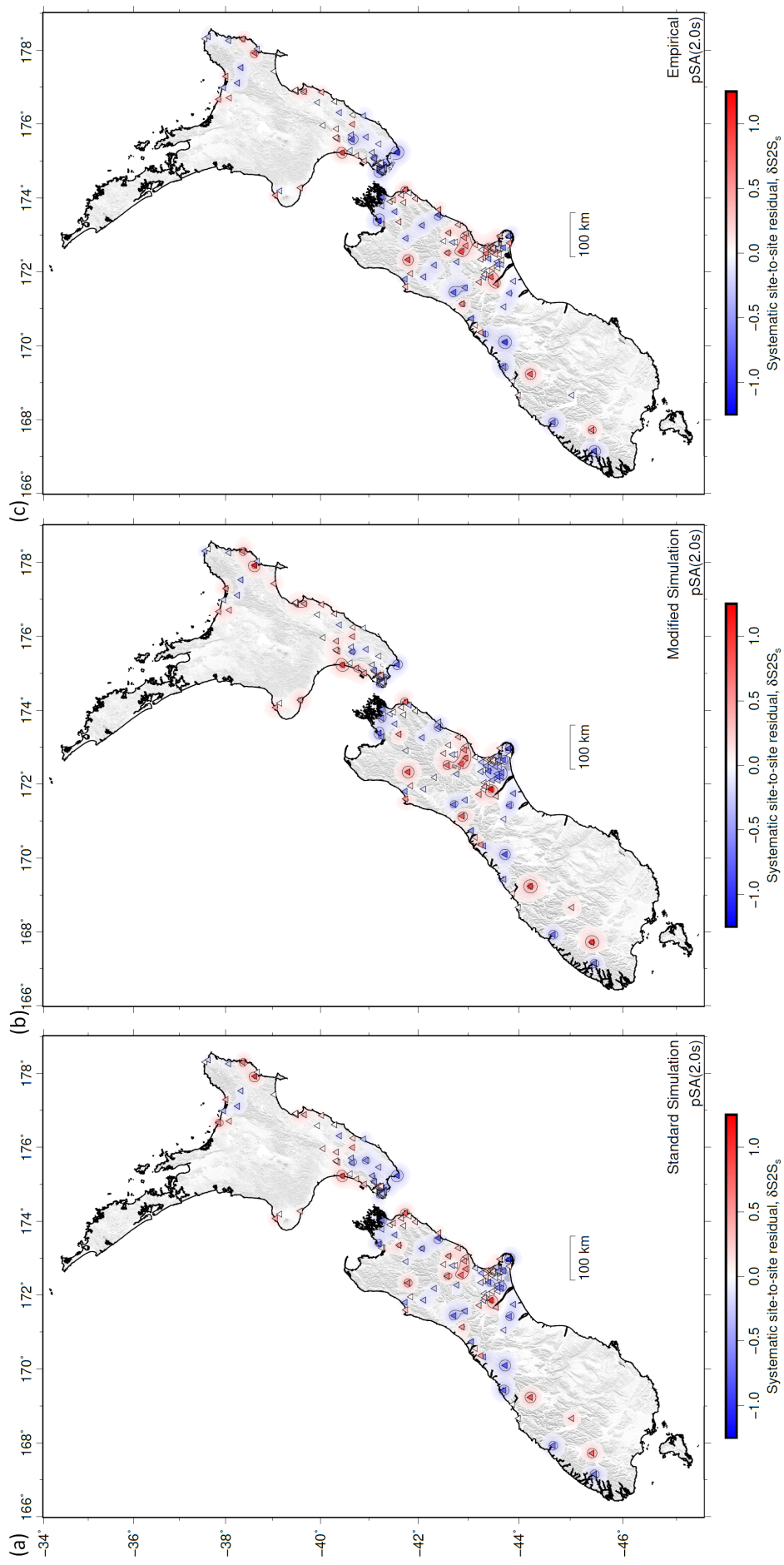


Figure F.5. Spatial distribution of pSA(2.0s) between-event residuals, $\delta S2S_s$, for 212 stations from: (a) Standard simulation; (b) Modified simulation; and (c) empirical prediction.

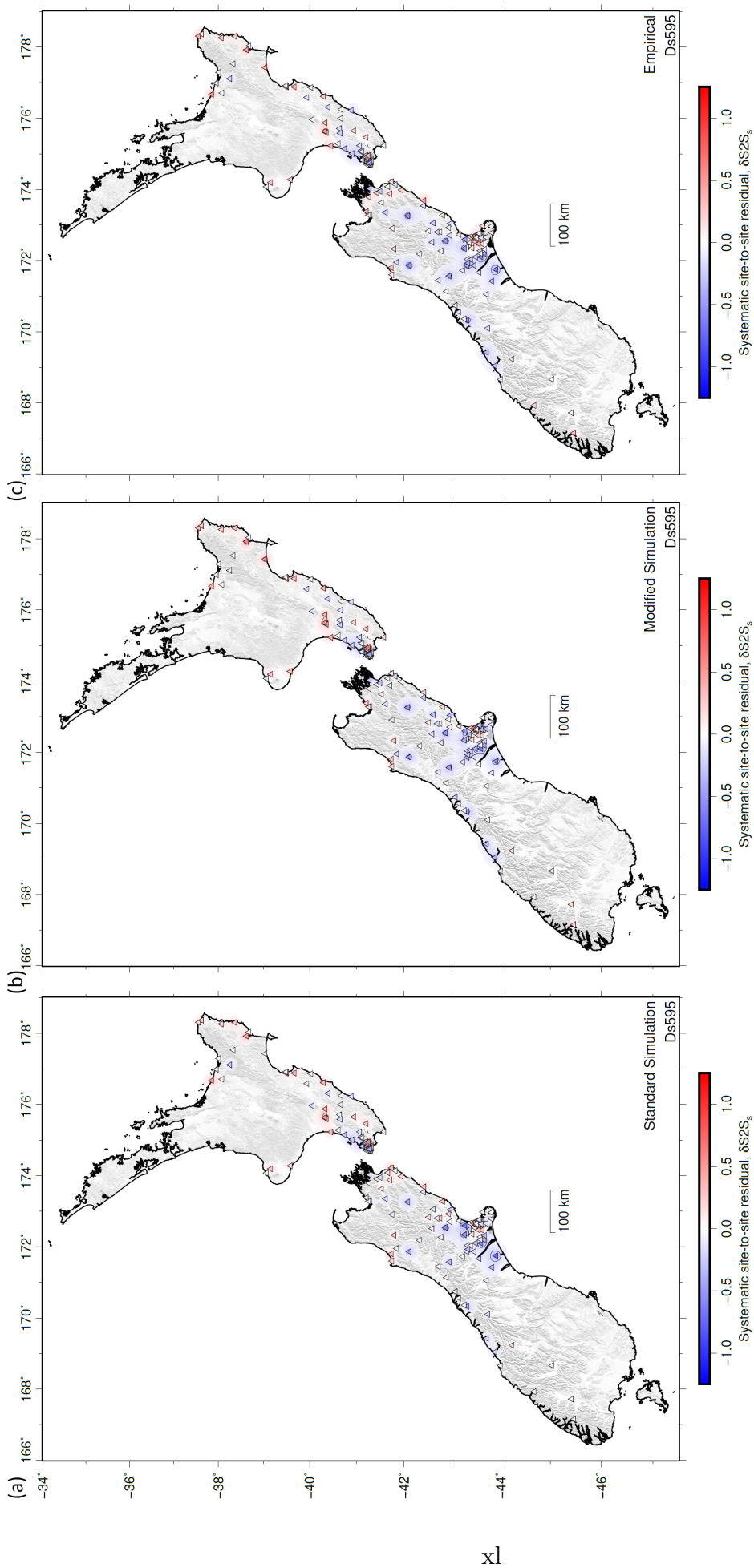


Figure F.6: Spatial distribution of D_{s595} between-event residuals, $\delta S2S_s$, for 212 stations from: (a) Standard simulation; (b) Modified simulation; and (c) empirical prediction.

1053 **G Electronic Supplement G: Additional Station Sub-**
 1054 **category Analysis**

1055 Figure G.1 and G.2 provide the station subcategory analysis for the Standard simulation
 1056 and empirical prediction which shows similar differences between subset and global biases
 1057 to the Modified simulation presented in the main text. Figure G.3 presents the average
 1058 $\delta S2S_s$ of each subcategory for each prediction method which shows that the bias-corrected
 1059 site-specific residuals are systematically similar between prediction methods with the ex-
 1060 ception of long-period pSA in the unmodelled sedimentary basin subcategory.

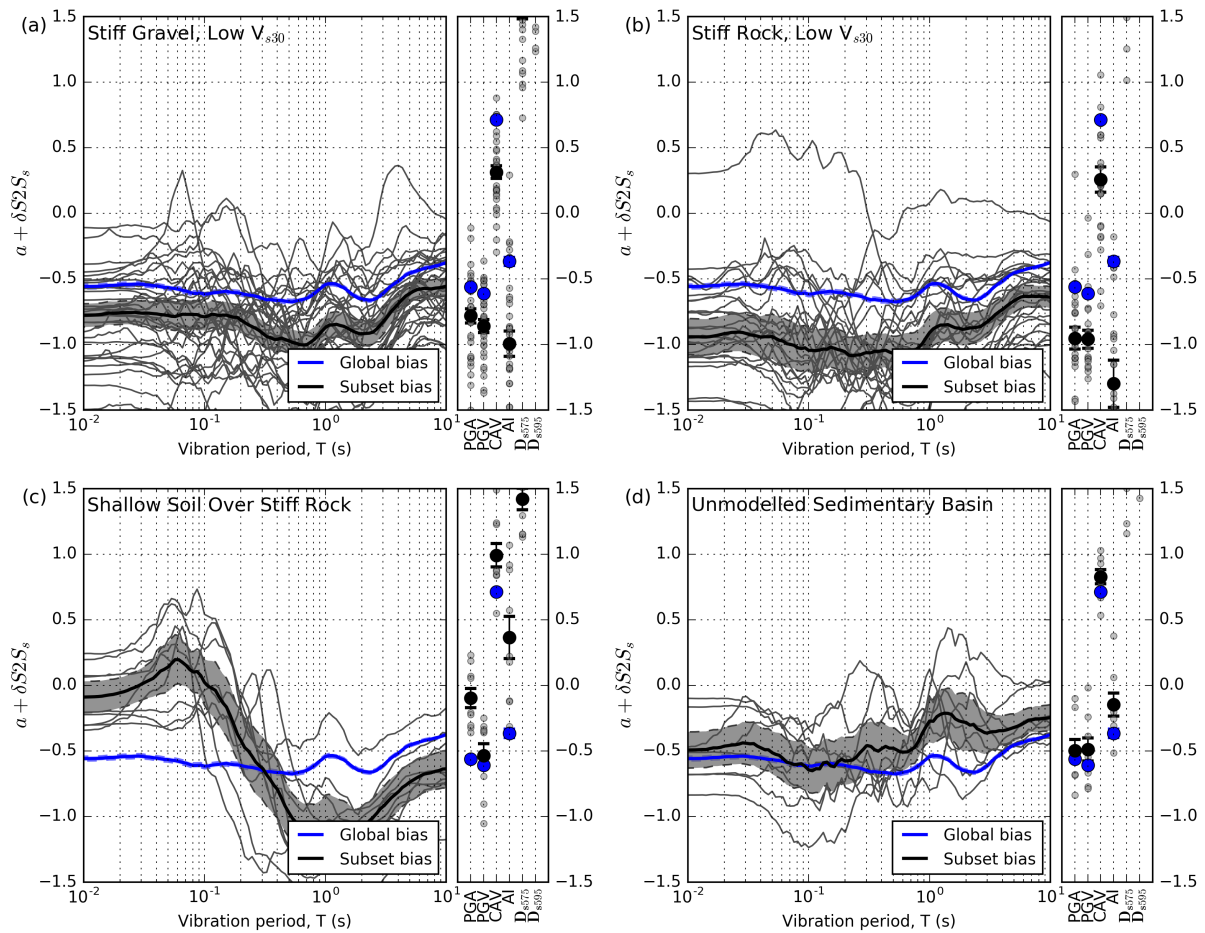


Figure G.1: Bias and systematic site-to-site residuals of station subcategories based on Standard simulation prediction: (a) stiff gravel sites with V_{s30} that is too low; (b) stiff rock sites with V_{s30} that is too low; (c) shallow soil overlying stiff rock sites; and (d) sites located in a sedimentary basin that is not modelled in the NZVM. Blue lines show the global model prediction bias, a , for the Standard simulation while the grey lines show $a + \delta S2S_s$ for each station in the subcategory, and the black line is the average of the grey lines.

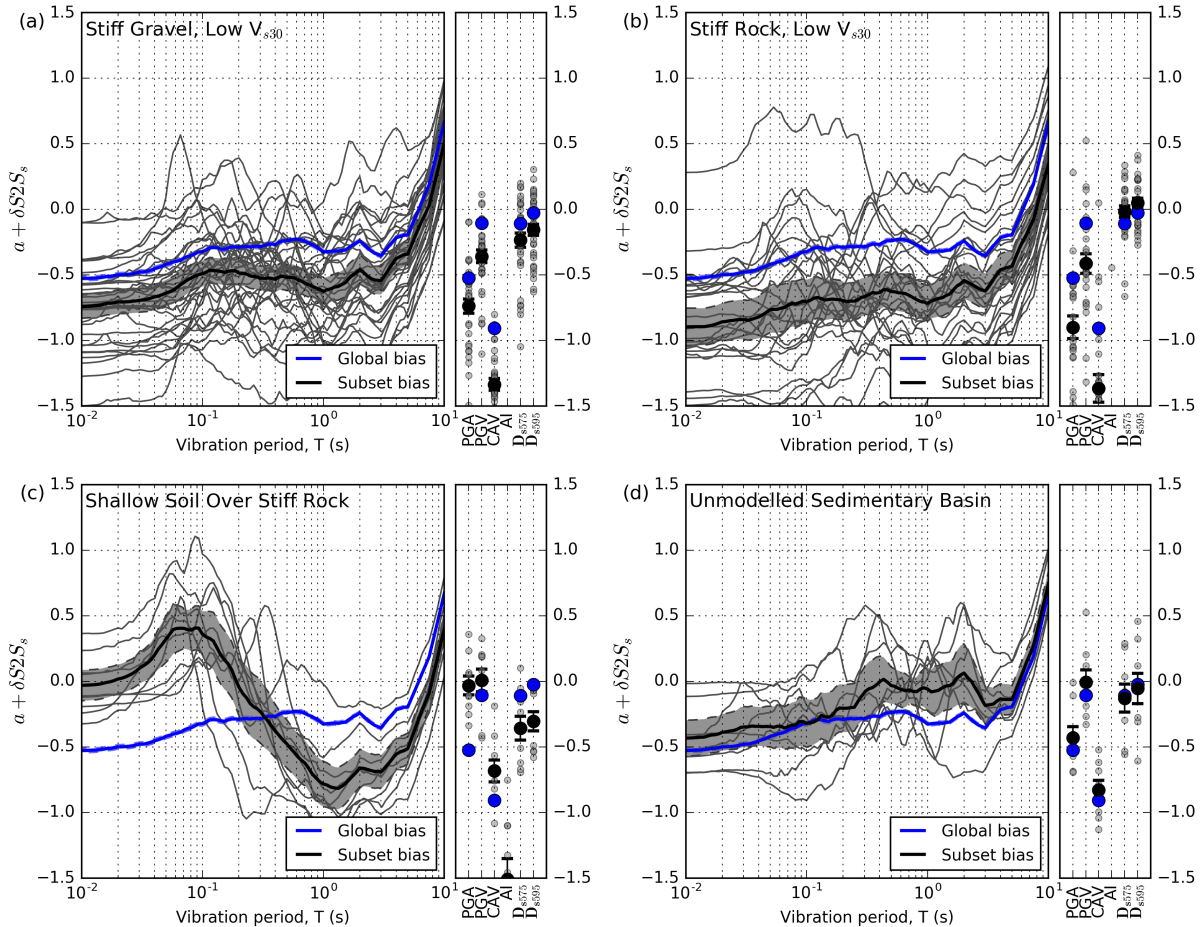


Figure G.2: Bias and systematic site-to-site residuals of station subcategories based on empirical GMM prediction: (a) stiff gravel sites with V_{s30} that is too low, (b) stiff rock sites with V_{s30} that is too low, (c) shallow soil overlying stiff rock sites, and (d) sites located in a sedimentary basin that is not modelled in the NZVM. Blue line shows the global model prediction bias for empirical GMMs while the grey lines show the model prediction bias $+ \delta S2S_s$ for each station in the subcategory, and the black line is the average of the grey lines.

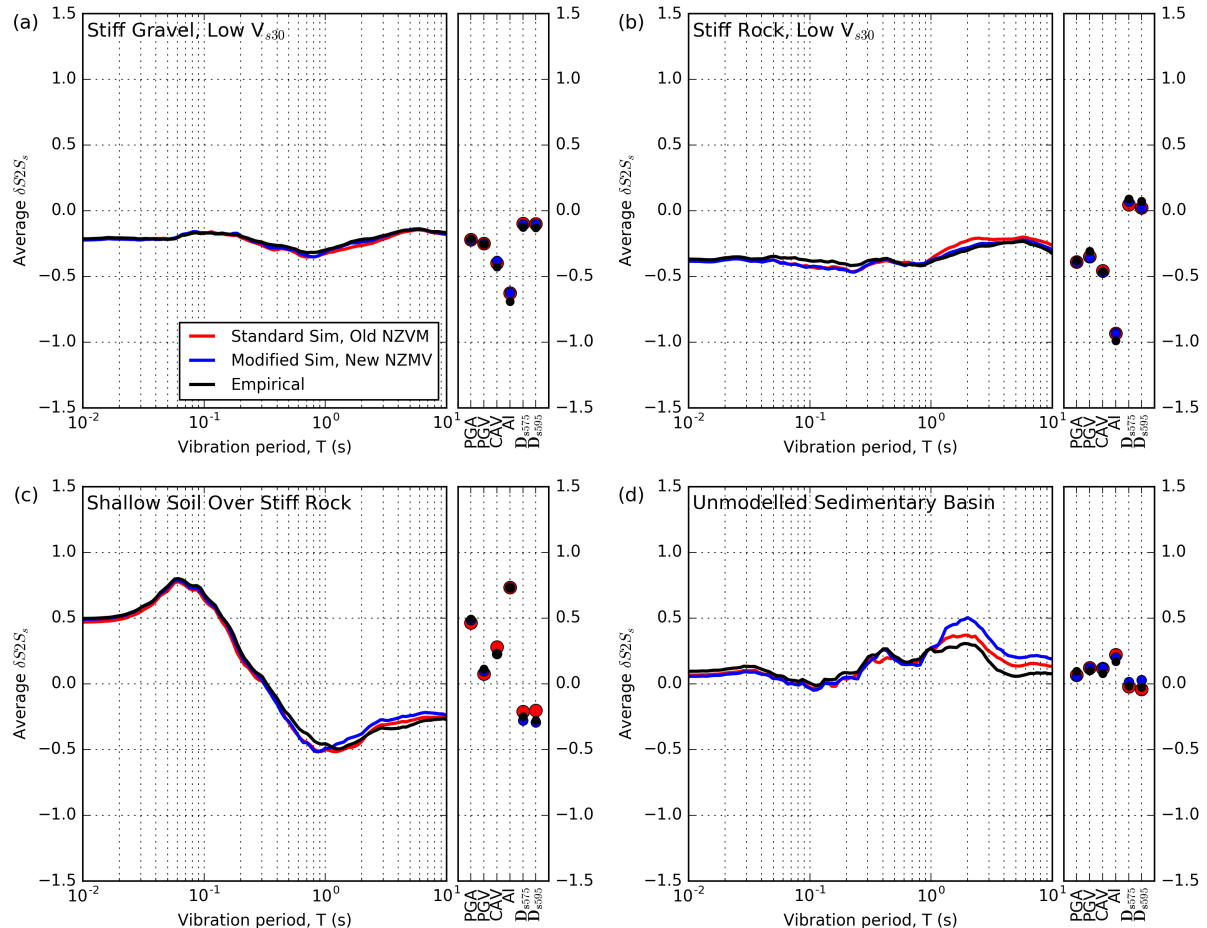


Figure G.3: Average systematic site-to-site residuals of station subcategories for all prediction methods: (a) stiff gravel sites with V_{s30} that is too low, (b) stiff rock sites with V_{s30} that is too low, (c) shallow soil over stiff rock sites, and (d) sites located in a sedimentary basin that is not modelled in the NZVM.